Wavefield Reconstruction, Inversion and Imaging Using Local solvers

by

© **Ligia Elena Jaimes Osorio**

A thesis submitted to the School of Graduate Studies in partial fulfillment of the requirements for the degree of Doctor of Philosophy.

Department of Earth Sciences

Memorial University

October 2021

St. John's, Newfoundland and Labrador, Canada

Abstract

In exploration geophysics, we usually implement non-invasive methods to image the interior of the Earth. Seismic methods, for example, are ideal for this purpose because they provide high-resolution images at large depths. During the construction of these images, understanding how seismic waves propagate through the subsurface is vital. Lacking analytical solutions for realistically complex models, numerical modeling becomes essential to comprehend the recorded data. Conventional modeling algorithms are designed to solve the wave equation throughout the entire model, even though we are often interested in only much smaller areas. To solve for the whole model is computationally expensive, particularly when the algorithm repeatedly simulates wavefields, as is often the case in common imaging techniques such as reverse time migration and full waveform inversion. The main goal of this thesis is to explore and understand the potential of local solvers under different scenarios, for instance, in the presence of large impedance contrast reflectors and complex geometries in different domains. We first demonstrate that a local acoustic-elastic solver can model the amplitude with sufficient accuracy between the surface and the reflector of interest and then can be used as a constraint in Amplitude Versus Offset (AVO) inversion. We show that the amplitude combined with the phase improves the convergence of this algorithm. However, the amplitude is not in perfect agreement with that obtained with full elastic modelling. This motivates our interest in building a local elastic solver that avoids the interchange between domains but keeps the computational, time, and resources cost feasible. We implement the Multiple Point Sources (MPS) method in a standard Finite Difference (FD) solver, computing the global wavefield in the local domain successfully using only the ability to record and inject data at the boundary, while being memory efficient. We test the robustness of the local elastic solver on different elastic models and uses in AVO and Phase Versus Offset (PVO) inversions, retrieving elastic parameters with high accuracy. To take the elastic solver to the next

level we assess the possibility of using converted wave modes during the inversion. To this end we explore different imaging conditions based on different wave modes that allow us to measure the focusing of the image to be ultimately used in conjunction with the local elastic solver. Notice that all implementations and results are shown in 2D.

Thesis Supervisor: Alison Malcolm
Title: Associate Professor

To my parents, Nubia y Mario

Acknowledgements

Like somebody said, "it has been the best and the worst time of my life." I think this person was doing a Ph.D. in Earth Science. My first and biggest thanks to my advisor and role model, Alison Malcolm. I am immensely grateful for the opportunity that she gave me. Achieving this goal was not easy since many times, I doubt that I could achieve it. But through all these years, Alison patiently supports, advised and guided me to reach where I am today. It has been a pleasure learning from and working with her.

Many more people have made parts of this work possible. Ali Gholami was great helping me when I was working with the acoustic-elastic solver. Bram Willemsen helped me to improve my first paper through his comments. Polina Zheglova, Erik F. M. Koene and Henrik R. Thomsen helped me to implement the elastic-local solver. A small detail was seen by Polina that enabled me to move forward in that project. Gregory Ely walked me through the world of real medical data. I want to thank my committee members, Dr. J. Kim Welford and Dr. Michael A. Slawinski, for their suggestions that helped to improve this thesis.

Thanks to each one of my friend and fellows researchers at MUN. Thanks for the incredible energy, respect, and support that helped me keep moving through difficult times. Finally, thanks to my family, who has always believed in me. Their constant love pushed me up throughout this challenging and arduous process.

Statement of contribution

This project was first started by Alison Malcolm and then was outlined and executed by Ligia Elena Jaimes-Osorio and Alison Malcolm. Ligia Elena Jaimes-Osorio developed, examined and refined the specific questions inquired along the course of study under the supervision and guidance of Alison Malcolm. Ligia Elena Jaimes-Osorio performed all the research, numerical calculations, and drafting for all the chapters in this thesis.

Ligia Elena Jaimes-Osorio presented the first results of Chapter 2 at the Geological Association of Canada (GAC) Newfoundland and Labrador Section Annual Meeting (2018), 5th International Domain Decomposition Methods Conference (2018) and SEG Technical Program Expanded Abstracts, (2018). Ligia Elena Jaimes-Osorio was awarded the best poster paper at SEG Anaheim 2018. All Expanded Abstracts have been co-authored by Alison Malcolm, who provided research and editorial guidance. The entire Chapter 2 is published in Geophysics and co-authored by Alison Malcolm and Ali Gholami. Alison Malcolm provided research supervision and provided editorial direction and help with the organization of the paper. Both Alison Malcolm and Ali Gholami helped to shape ideas. This paper was reviewed by Lucas Abraham Willemsen, John Etgen and two anonymous reviewers.

Chapter 3 is published in Geophysics under the section of Geophysical Software and Algorithms and co-authored by Alison Malcolm, Polina Zheglova, Erik F. M. Koene and Henrik R. Thomsen. Alison Malcom and Polina Zheglova provided help shaping ideas. All the co-authors provided editorial guidance and helped with the organization of the paper. This paper was reviewed by Chuen Hon Arthur Cheng, Filippo Broggini, Eric Verschuur, Gustavo Alves and other two anonymous reviewers. In addition,

this paper was presented by Ligia Elena Jaimes-Osorio at Geoconvention 2020 where Ligia Elena Jaimes-Osorio was selected as a 2020 Best Student Poster Presentation. Also, it was presented at AGU Fall meeting 2020, the 82nd European Association of Geoscientists & Engineers (EAGE) Annual meeting and the mini-symposium WCCM-ECCOMAS 2020 by Ligia Elena Jaimes-Osorio.

Chapter 4 has been accepted in SEG Technical Program Expanded Abstracts 2021. Expanded Abstracts have been co-authored by Alison Malcolm, who provided research and editorial guidance. This Chapter is expected to be presented at SEG Annual International Meeting (2021).

A summary Chapter 5 has been accepted in IEEE IUS 2021 International Ultrasound Symposium. Expanded Abstracts have been co-authored by Alison Malcolm, Gregory Ely and Guillaume Renaud, who provided research and editorial guidance. This Chapter is expected to be presented at IEEE IUS 2021 International Ultrasound Symposium (2021). Alison Malcolm and Gregory Ely helped shaping ideas and organize the abstract. Guillaume Renaud provided the true data used in this study. This Chapter is also expected to be submitted in Ultrasonics Journal Elsevier and co–authored by Alison Malcolm, Gregory Ely and Guillaume Renaud.

Table of contents

List of tables

List of figures

Chapter 1

Introduction

Geophysical observations are fundamental to our understanding of the Earth because they allow us to see things that cannot be explored by direct observation. Exploration geophysics, for example, uses indirect observation methods such as inverse methods to understand deep horizons and structures of the subsurface. Inverse methods that are based on seismic imaging have been established in exploration geophysics because they pinpoint areas of prospective interest such as oil, gas reservoirs and mineral resources, reducing costs and risks. When seismic imaging techniques are combined with other algorithms such as Full Waveform Inversion (FWI), a more precise measurement of the Earth's properties can be obtained [75].

Our interest lies in exploration geophysics, specifically in understanding the behaviour and locations of subsurface fluids using seismic data. Seismic data are essential physical data in geophysics, giving the best resolution of the subsurface to locate and monitor reservoirs. Conventional algorithms that use seismic imaging techniques have been developed mainly by focussing on resolving an entire Earth model, even though our interest usually lies in a small region of the model. To update the Earth model for these targeted regions, propagating waves through the entire model is usually necessary, despite knowing that most of the Earth model will remain the same. Because of these observations, local wavefield solvers have been designed to reduce the computational size and cost while generating the same wavefield as a whole domain solver would within the local areas of interest [61, 87]. In this thesis, we investigate applications of local solvers, as outlined in the following subsections. A brief description of the underlying methods and relevant concepts and principles used in this thesis are

shown in this introduction.

1.0.1 Wavefield modeling

Seismic waves are widely used to create images of the Earth's interior. Nevertheless, we need to understand how wavefields propagate through the subsurface to appreciate the recorded seismic data. However, for 2D and 3D heterogeneous complex models, there are no analytical solutions. Therefore, approximate numerical methods have been created in geophysics. Because combining numerical methods with realistic Earth models results in synthetic seismograms that help interpret real seismic data. Numerical methods are the basis for testing processing techniques, such as migration to finally inferring subsurface images.

Some of the most sophistical migration techniques are Reverse Time migration (RTM) and FWI. RTM is well known because it can handle complex geological models by forward-propagating a simulated source in time and back-propagating in time the recorded wavefield to finally applying a zero time-lag cross-correlation between the two wavefields. Otherwise, FWI is a powerful high-resolution technique that aims to reconstruct the subsurface distribution of elastic properties by seeking the best model that explains the recorded data.

In seismic imaging algorithms such as FWI and RTM, the most expensive part is modelling the wavefield. One of the common methods to simulate wavefields in exploration geophysics is the Finite-Different (FD) method. This method is conceptually simple and can be easily implemented in parallel computer architectures. Using the FD method, we are able to model particle displacement $u(\mathbf{x}, t)$, velocities $v(\mathbf{x}, t)$, and density $\rho(\mathbf{x})$, which are features that define seismic waves. The local solvers used and implemented in this research are based on the FD method.

1.0.2 Characteristics of Seismic Waves

Seismic waves can be characterized by their particle displacement $u_i(\mathbf{x}, t)$, which are the distances of particles from their equilibrium positions that depend on space ($\mathbf{x}$) and time (t). To derive an expression for these displacements, we start by noting that seismic waves cause stresses around the equilibrium state in a material. These

stresses are represented by a stress tensor, $\tau_{ij}(\mathbf{x}, t)$ which describes the force per unit area applied to the surface of the material, where i describes the plane on which the force is applied and j indicates the direction of the force. These stresses result in a strain, which represent the deformation of the material and can be written as

$$\xi_{ij}(\mathbf{x}, t) = \frac{1}{2}\left(\frac{\partial u_i(\mathbf{x}, t)}{\partial x_j} + \frac{\partial u_j(\mathbf{x}, t)}{\partial x_i}\right). \tag{1.1}$$

Both the stress, $\tau_{ij}(\mathbf{x}, t)$, and strain, $\xi_{ij}(\mathbf{x}, t)$, tensors are assumed symmetric, such that each tensor only contains 6 independent components.

1.0.3 Wave Equations

To produce the elastodynamic wave equation, the displacement and stress are related using Newton's law,

$$\rho(\mathbf{x})\frac{\partial^2 u_i(\mathbf{x}, t)}{\partial t^2} = \frac{\partial \tau_{ij}(\mathbf{x}, t)}{\partial x_j} + f_i(\mathbf{x}, t), \tag{1.2}$$

where $\partial^2/\partial t^2$ is the second time derivative, ρ represents the density of the material, $\partial/\partial x_j$ represents the space derivative and $f_i(\mathbf{x}, t)$ represents the external force vector. Because we assume no heat loss and only small displacements in the medium, the stiffness tensor, C_{ijkl}, can be used to denote the linear lossless elastic stress-strain relation as $\tau_{ij}(\mathbf{x}, t) = C_{ijkl}(\mathbf{x}, t)\xi_{ij}(\mathbf{x})$. Where $C_{ijkl}(\mathbf{x}, t)$ is symmetric, i.e, $C_{ijkl} = C_{jikl} = C_{ijlk} = C_{klij}$, due to the symmetries of the stress and strain tensors, and the conservation of strain energy [2].

Note that the symmetry in C_{ijkl} leads to a simple version of the linear lossless elastic stress-displacement relation,

$$\begin{aligned}\tau_{ij}(\mathbf{x}, t) &= C_{ijkl}(\mathbf{x})\frac{1}{2}\left(\frac{\partial u_k(\mathbf{x}, t)}{\partial x_l} + \frac{\partial u_l(\mathbf{x}, t)}{\partial x_k}\right), \\ &= C_{ijkl}(\mathbf{x})\frac{\partial u_k(\mathbf{x}, t)}{\partial x_l}.\end{aligned} \tag{1.3}$$

By combining equations 1.2 and 1.3, we can formulate the wave equation as a

displacement-stress system:

$$\begin{aligned} \rho(\mathbf{x})\frac{\partial^2 u_i(\mathbf{x},t)}{\partial t^2} &= \frac{\partial \tau_{ij}(\mathbf{x},t)}{\partial x_j} + f_i(\mathbf{x},t), \\ \tau_{ij}(\mathbf{x},t) &= C_{ijkl}(\mathbf{x})\frac{\partial u_k(\mathbf{x},t)}{\partial x_l}. \end{aligned} \tag{1.4}$$

A variation of the **displacement-stress** system can be found by substituting $\partial u_i/\partial t = v_i$, which represents the particle velocity. Thus, a **velocity-stress** system is described as,

$$\begin{aligned} \rho(\mathbf{x})\frac{\partial v_i(\mathbf{x},t)}{\partial t} &= \frac{\partial \tau_{ij}(\mathbf{x},t)}{\partial x_j} + f_i(\mathbf{x},t), \\ \frac{\partial \tau_{ij}(\mathbf{x},t)}{\partial t} &= C_{ijkl}(\mathbf{x})\frac{\partial v_k(\mathbf{x},t)}{\partial x_l}. \end{aligned} \tag{1.5}$$

We now have an equation of motion in terms of **velocity-stress** (equation 1.5), which is the equation that we are going to model with the FD method.

P- and S-Wave Velocities

In isotropic media the relation $\tau_{ij}(\mathbf{x},t) = C_{ijkl}(\mathbf{x},t)\xi_{ij}(\mathbf{x})$ becomes,

$$\tau_{ij}(\mathbf{x},t) = \lambda\xi_{kk}\delta_{ij} + 2\mu\xi_{ij} = \lambda\theta\delta_{ij} + 2\mu\xi_{ij}, \tag{1.6}$$

where θ is the dilatation, and μ and λ are called the Lamé constants and are defined as,

$$C_{ijkl} = \lambda\delta_{ij}\delta_{kl} + \mu(\delta_{ik}\delta_{jl} + \delta_{il}\delta_{jk}). \tag{1.7}$$

Using equation 1.4 and 1.6, we can derive the wave equation in an isotropic medium,

$$\begin{aligned} \rho\frac{\partial^2 \mathbf{u}}{\partial t^2} &= (\lambda + 2\mu)\nabla(\nabla.\mathbf{u}) - \mu\nabla\times\nabla\times\mathbf{u} \\ \rho\ddot{\mathbf{u}} &= (\lambda + 2\mu)\nabla(\nabla.\mathbf{u}) - \mu\nabla\times\nabla\times\mathbf{u}. \end{aligned} \tag{1.8}$$

We can separate equation 1.8 into solutions for P- and S-waves by calculating the divergence and curl, respectively.

When we compute the divergence of equation 1.8, we obtain

$$\begin{aligned} \rho\frac{\partial^2(\nabla.\mathbf{u})}{\partial t^2} &= (\lambda+2\mu)\nabla^2(\nabla.\mathbf{u}) \\ \nabla^2(\nabla.\mathbf{u}) - \frac{1}{\alpha^2}\frac{\partial^2(\nabla.\mathbf{u})}{\partial t^2} &= 0, \end{aligned} \tag{1.9}$$

where α is the P-wave velocity,

$$\alpha = \sqrt{\frac{\lambda+2\mu}{\rho}}, \tag{1.10}$$

note that equation 1.9 expresses **acoustic wave equation**. By computing the curl of equation 1.8, we obtain,

$$\begin{aligned} \rho\frac{\partial^2(\nabla\times\mathbf{u})}{\partial t^2} &= -\mu\nabla\times\nabla\times\nabla\times\mathbf{u} \\ \rho\frac{\partial^2(\nabla\times\mathbf{u})}{\partial t^2} &= \mu\nabla^2(\nabla\times\mathbf{u}) \\ \nabla^2(\nabla\times\mathbf{u}) - \frac{1}{\beta^2}\frac{\partial^2(\nabla\times\mathbf{u})}{\partial t^2} &= 0, \end{aligned} \tag{1.11}$$

where β is the S-wave velocity,

$$\beta = \sqrt{\frac{\mu}{\rho}}. \tag{1.12}$$

So, using α and β we can rewrite equation 1.8 in terms of P- and S-wave as

$$\ddot{\mathbf{u}} = \underbrace{\alpha^2\nabla(\nabla.\mathbf{u})}_{P-wave} - \underbrace{\beta^2\nabla\times(\nabla\times\mathbf{u})}_{S-wave} \tag{1.13}$$

Potentials

A vector can be represented as a sum of curl-free and divergence-free forms, known as the Helmholtz decomposition [2],

$$\begin{aligned} \mathbf{u} &= \nabla\phi + \nabla\times\mathbf{\Psi} \\ \nabla\cdot\Phi &= 0, \end{aligned} \tag{1.14}$$

where ϕ is the P-wave scalar potential and $\mathbf{\Psi}$ is the S-wave vector potential. Therefore, we have

$$\begin{aligned} \nabla.\mathbf{u} &= \nabla^2\phi \\ \nabla \times \mathbf{u} = \nabla \times \nabla \times \mathbf{\Psi} &= -\nabla^2\mathbf{\Psi}. \end{aligned} \tag{1.15}$$

Inserting equations 1.15 into equations 1.9 and 1.11 respectively, we obtain two equations for these potentials,

$$\begin{aligned} \nabla^2\phi - \frac{1}{\alpha^2}\frac{\partial^2\phi}{\partial t^2} &= 0 \\ \nabla^2\mathbf{\Psi} - \frac{1}{\beta^2}\frac{\partial^2\mathbf{\Psi}}{\partial t^2} &= 0, \end{aligned} \tag{1.16}$$

therefore, P- and S-wave displacements are given by the gradient of ϕ and curl of $\mathbf{\Psi}$ in equation 1.16.

To this point, we have shown a brief description of the seismic wave characteristics, different wave equations systems, the P- and S-wave velocities and their potentials—all of these concepts are used throughout this thesis. The following section shows the conventional numerical scheme of the FD method for the velocity-stress system, which is the equations system used in the elastic solver implemented in this research.

1.0.4 Modeling the equation of motion with finite differences

The Finite Difference (FD) method is used because it is easy to implement and allows us to numerically approximate the derivatives, which cannot be computed analytically. In this thesis we use the **velocity-stress** system of equations defined in equation 1.5,

which can be transformed explicitly into the following first-order hyperbolic system,

$$\begin{aligned}
\frac{\partial v_x}{\partial t} =& \frac{1}{\rho}\left(\frac{\partial \tau_{xx}}{\partial x} + \frac{\partial \tau_{xz}}{\partial z}\right) \\
\frac{\partial v_z}{\partial t} =& \frac{1}{\rho}\left(\frac{\partial \tau_{xz}}{\partial x} + \frac{\partial \tau_{zz}}{\partial z}\right) \\
\frac{\partial \tau_{xx}}{\partial t} =& (\lambda + 2\mu)\frac{\partial v_x}{\partial x} + \lambda \frac{\partial v_z}{\partial z} \\
\frac{\partial \tau_{zz}}{\partial t} =& (\lambda + 2\mu)\frac{\partial v_z}{\partial z} + \lambda \frac{\partial v_x}{\partial x} \\
\frac{\partial \tau_{xz}}{\partial t} =& \mu\left(\frac{\partial v_x}{\partial z} + \frac{\partial v_z}{\partial x}\right),
\end{aligned} \tag{1.17}$$

where $\lambda = \frac{\nu E}{(1+\nu)(1-2\nu)}$ and $\mu = \frac{E}{2(1+\nu)}$ are the Lamé coefficients, where E represents Young's Modulus and ν represents Poisson's ratio, (v_x, v_z) is the velocity vector $v_i(\mathbf{x}, t)$ and $(\tau_{xx}, \tau_{xz}, \tau_{zz})$ is the stress tensor $\tau_{ij}(\mathbf{x}, t)$ defined in a 2D medium with horizontal axis x and a vertical axis z pointing downward. Here the medium is assumed to be linearly elastic and isotropic. Note that the external source f_i is not included in equation 1.17.

Following [83], we use a centered FD to discretize the medium derivatives using a staggered grid. Figure1.1 shows the staggered grid scheme.

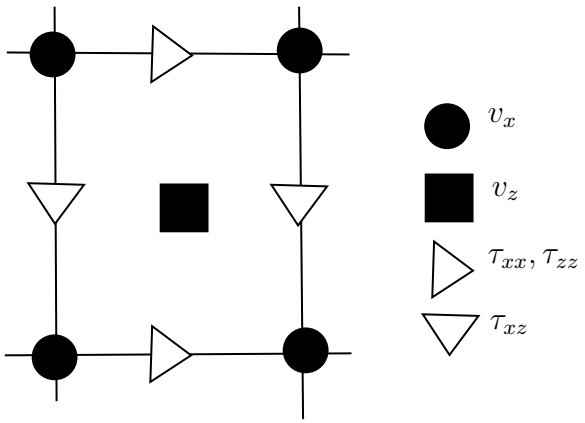

Figure 1.1: Staggered elastic grid scheme. The black circle and square represent the stresses and Lamé coefficients at time $(k\Delta t)$. White triangles represent velocities and buoyancy at time $(k + 1/2)\Delta t$.

The conventional numerical scheme that represents the system of equations in 1.17

is,

$$v_x|_{i,j}^{k+1/2} = v_x|_{i,j}^{k-1/2} + \frac{\Delta t}{\rho_{i,j}} \left(\frac{\tau_{xx}|_{i+1/2,j}^{k} - \tau_{xx}|_{i-1/2,j}^{k}}{\Delta x} + \frac{\tau_{xz}|_{i,j+1/2}^{k} - \tau_{xz}|_{i,j-1/2}^{k}}{\Delta z} \right)$$

$$v_z|_{i+1/2,j+1/2}^{k+1/2} = v_z|_{i+1/2,j+1/2}^{k-1/2} + \frac{\Delta t}{\rho_{i+1/2,j+1/2}} \left(\frac{\tau_{xz}|_{i+1,j+1/2}^{k} - \tau_{xz}|_{i,j+1/2}^{k}}{\Delta x} + \frac{\tau_{zz}|_{i+1/2,j+1}^{k} - \tau_{zz}|_{i+1/2,j}^{k}}{\Delta z} \right)$$

$$\tau_{xx}|_{i+1/2,j}^{k+1} = \tau_{xx}|_{i+1/2,j}^{k} + (\lambda + 2\mu)_{i+1/2,j} \frac{\Delta t}{\Delta x} \left(v_x|_{i+1,j}^{k+1/2} - v_x|_{i,j}^{k+1/2} \right) + \lambda_{i+1/2,j} \frac{\Delta t}{\Delta z} \left(v_z|_{i,j+1}^{k+1/2} - v_z|_{i,j}^{k+1/2} \right)$$

$$\tau_{zz}|_{i+1/2,j}^{k+1} = \tau_{zz}|_{i+1/2,j}^{k} + (\lambda + 2\mu)_{i+1/2,j} \frac{\Delta t}{\Delta z} \left(v_z|_{i+1,j}^{k+1/2} - v_z|_{i,j}^{k+1/2} \right) + \lambda_{i+1/2,j} \frac{\Delta t}{\Delta x} \left(v_x|_{i+1,j}^{k+1/2} - v_x|_{i,j}^{k+1/2} \right)$$

$$\tau_{xz}|_{i,j+1/2}^{k+1} = \tau_{xz}|_{i,j+1/2}^{k} + \mu_{i,j+1/2} \frac{\Delta t}{\Delta z} \left(v_x|_{i+1,j}^{k+1/2} - v_x|_{i,j}^{k+1/2} \right) + \lambda_{i,j+1/2} \frac{\Delta t}{\Delta x} \left(v_z|_{i+1,j}^{k+1/2} - v_k|_{i,j}^{k+1/2} \right) \tag{1.18}$$

where k represents the index for time discretization, (i, j) for (x, z) discretization, Δt is the grid step in time, and Δx and Δz are the grid steps for the x and z axis, respectively. Thus, we compute the velocities v_x and v_z at time $(k + 1/2)\Delta t$ and stresses $(\tau_{xx}, \tau_{xz}, \tau_{zz})$ at time $(k+1)\Delta t$ from velocity at $(k-1/2)\Delta t$ and stress at time $k\Delta t$. The repeated calculation of equation 1.18 for later and later times leads to an algorithm that simulates seismic waves for an arbitrary time duration.

Note that the FD approximation implies that we are not solving the original wave equation (equation 1.17) anymore, but a modified equation instead (equation 1.18). Thus, this approximation brings a natural trade-off between the choice of Δt, Δx and Δz values, the approximation accuracy, and the computational cost involved. Note that we use a first-order difference approximation; higher-order differences will result in a more accurate approximation (for more details on FD parameters trade-off see [36]).

1.1 Extracting the physics

After understanding the mathematical approximation of the modelling of seismic wave propagation, we now focus on the seismic methods that use seismic modelling in their algorithms to retrieve elastic parameters. In exploration geophysics, we are

usually interested in two types of seismic waves – compressional (P-waves), in which the direction of particle motion is parallel to the direction of wave propagation and transversal (S-waves), in which the direction of particle motion is orthogonal to the direction of wave propagation [13] – that's because the combination of the P- and S-wave velocities and the density define the seismic response or reflection coefficient that varies according to the contrast of subsurface rocks. These contrasts, in turn, depend on the lithology, porosity, pore-fluid content and pressure of the rocks [9]. However, the dependence of seismic attributes on angle or offset, called Amplitude Variation with Offset or Angle (AVO or AVA) gives more information than just the zero offset reflection coefficients. Part of this research involves analyzing AVO effects and FWI methods with local solvers to retrieve elastic parameters in areas of interest. In the following subsection we describe the general concepts of these two methods.

1.1.1 Amplitude Variation with Offset – AVO Inversion

AVO analysis is a method that attempts to exploit the offset dependent variation of the P-wave reflection coefficients to define anomalous contrasts in shear wave velocities and density across an interface. Figure 1.2 illustrates synthetic seismic data that exhibit AVO. The traces resulting for each offset do not have the same amplitude as the vertical incidence or zero offset. Conventionally, the AVO method and its approximations are based on plane waves, which only sample one incoming angle. Moreover, all approximations are derived under the same assumptions; small changes in P- and S-wave velocities and density across the interface and small angles of incidence, limiting conventional AVO inversion to small to moderate offsets. Figure 1.3 shows the partition of energy of an incident P-wave amplitude into four components, reflected P- and S-waves and refracted P- and S-waves and the associated reflected and refracted coefficient curves. Note the significant changes at the critical angle for the reflected P- and S-waves. The shape of these coefficient curves varies according to different medium parameters.

One way to get around this limitation is using FD elastic modeling with point sources to simulate the full spherical waveform. Figure 1.4 illustrates the plane and spherical waveforms. In spherical full-waveform simulations, the spherical reflection coefficients include more than one incoming angle, incorporating additional information from adjacent angles within the first Fresnel zone of the reflection point. Figure

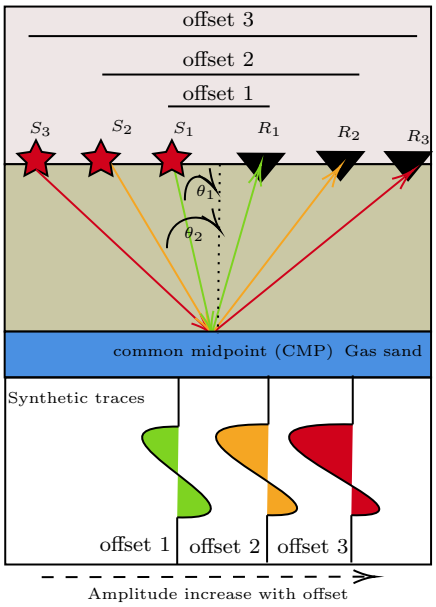

Figure 1.2: Illustration of seismic exhibits AVO.

1.5 illustrates the Fresnel zone involved in the spherical wave reflection at a plane homogeneous interface. The incorporation of information from adjacent angles allows a smooth transition around the critical angle in spherical reflection coefficient AVO curves [22]. Figure 1.6 shows a schematic comparison between spherical and plane reflection coefficient AVO curves.

1.1.2 Full Waveform Inversion – FWI

In contrast to AVO inversion, Full Waveform Inversion (FWI) methods seek to exploit the seismic wavefield's full information content over a broad range of incidence angles to build subsurface models with a wide range of wavenumbers, allowing us to invert for more complicated Earth models [58, 84]. FWI aims to recover an Earth model of the subsurface by iteratively finding better models m with synthetic wavefields $u(m)_{syn}$ by progressively matching the observed data d_{obs} better, reducing an objective function $\mathcal{F}$ (Figure 1.7). Commonly, a least-squares objective function is used, which includes all combinations of source and receiver wavefields,

$$\mathcal{F}(m) = \sum_s \sum_r \sum_t \frac{1}{2} \left|\left| d_{obs}(s,r,t) - u(m;s,r,t)_{syn} \right|\right|_2^2, \tag{1.19}$$

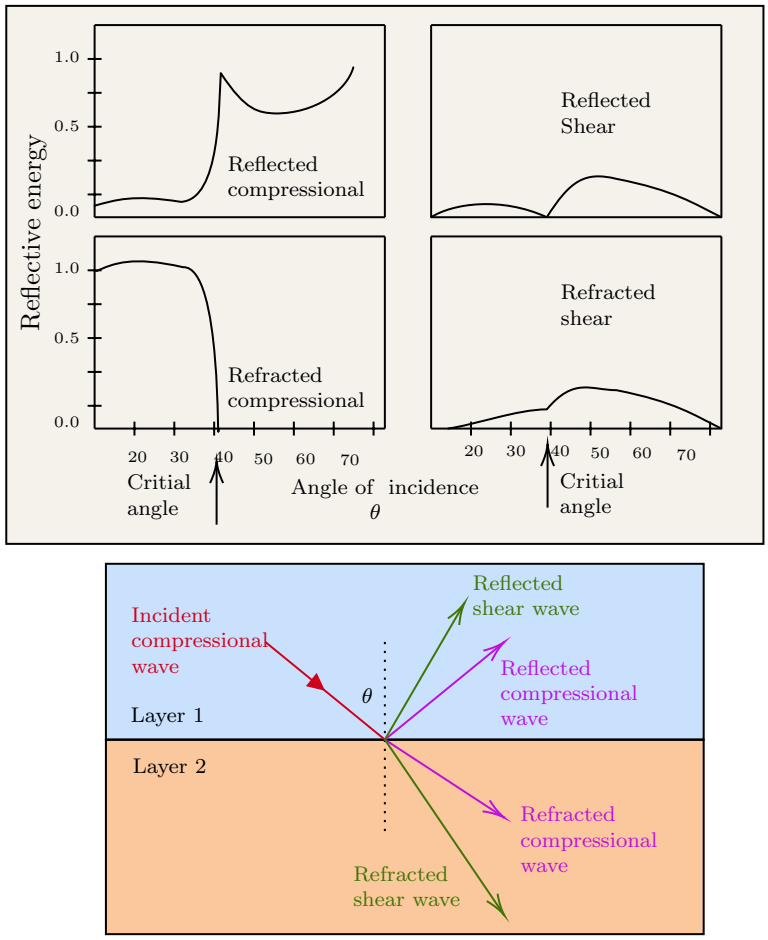

Figure 1.3: Reflection coefficients and partitioning of a unit-amplitude incidence P-wave energy into four components- reflected and refracted P- and S- waves. Based on [60]

$||\cdot||$ represents the norm and $\sum_s$ represents sum over sources. Because FWI uses pre-stack data the risk of losing useful information is minimal. Even though FWI was introduced in the 80s by [42, 75], it only became manageable in 2D at the end of the 90s and in 3D in the 2000s, due to the high computational cost associated with the wavefield simulations [58, 56, 82].

The cost of FWI comes primarily from the efficiency of the forward model's wavefield simulations since it is applied more than once in the inversion process and usually in large domains. Specifically, to evaluate an objective function for a model estimate m_i, a number n_s of wavefield simulations is required, where n_s represents the number of sources. Then, the gradient of the objective function is computed and evaluated at the current model m_i. Thus, n_s additional simulations are required to calculate the

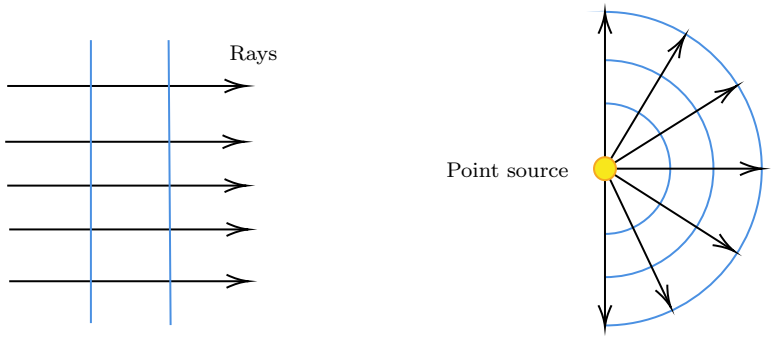

(a) Planel wave fronts (b) Spherical wave fronts

Figure 1.4: Illustration of (a) plane wave fronts and (b) spherical wave fronts.

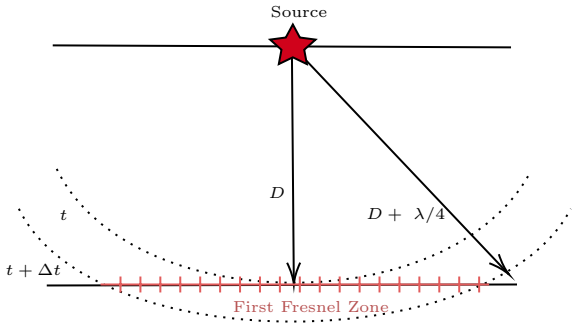

Figure 1.5: schematic illustration of the Fresnel zone for a spherical wave at a plane homogeneous interface.

adjoint wavefields needed for the gradient. In addition, n_s wavefield simulations are needed to compute the search direction to find a new model m_{i+1} that results in a lower objective function value. Thus, in this simple scenario, when only one evaluation along the search direction is required, the cost of one FWI iteration is $3n_s$. After, the model is updated, the procedure starts again for the next iteration. Note that in conventional FWI, the number of iterations required for the inversion to converge can range from two to thousands. Figure 1.7 illustrates the iterative procedure for the FWI method and shows where the n_s wavefield simulations take place (for more details refer to [58]).

Based on the previous analysis, it is clear that the computational cost of FWI is directly proportional to the number of sources, making it quickly increase its cost. In addition, we are usually interested in solving for targeted areas, however, to update the model for these target regions, propagating waves through the entire model is usually necessary, despite knowing that most of the Earth model will remain the same.

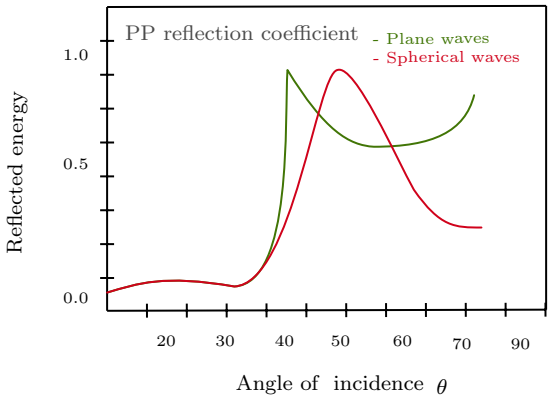

Figure 1.6: Schematic illustration of reflection coefficients AVO curves using planar and spherical waves.

Because of these observations, local wavefield solvers have been designed to reduce the computational size and cost while generating the same wavefield as a whole domain solver would within the local areas of interest [61, 87]. The following section presents a brief overview of seismic wavefield reconstruction locally.

1.2 Wavefield reconstruction

Usually, seismic waves are recorded using sources and receivers that are constrained to be on the Earth's surface. Then seismic wave propagation modeling methods are applied to evaluate the wavefield acquired on a suite of closely related subsurface models. The areas of interest or the changes between models evaluated are often limited to subdomains of the subsurfaces. For those cases, employing techniques that do not require repeated full wavefield simulation for the entire model is worthwhile—instead, modelling the wavefield only in the region of interest or where the change is expected (Figure 1.8).

Different authors have investigated the reconstruction of local wavefields in many different configurations. For instance, [28] investigated the case of a homogeneous medium with inhomogeneities restricted to a bounded subdomain. They computed the wavefield by partitioning the inhomogeneous subdomain into a collection of small volumes. Impedance-to-impedance maps connect the volumes to their neighbours. The volumes are merged recursively in a tree-like fashion to generate an impedance-to-impedance map for the entire subdomain. This impedance-to-impedance map then

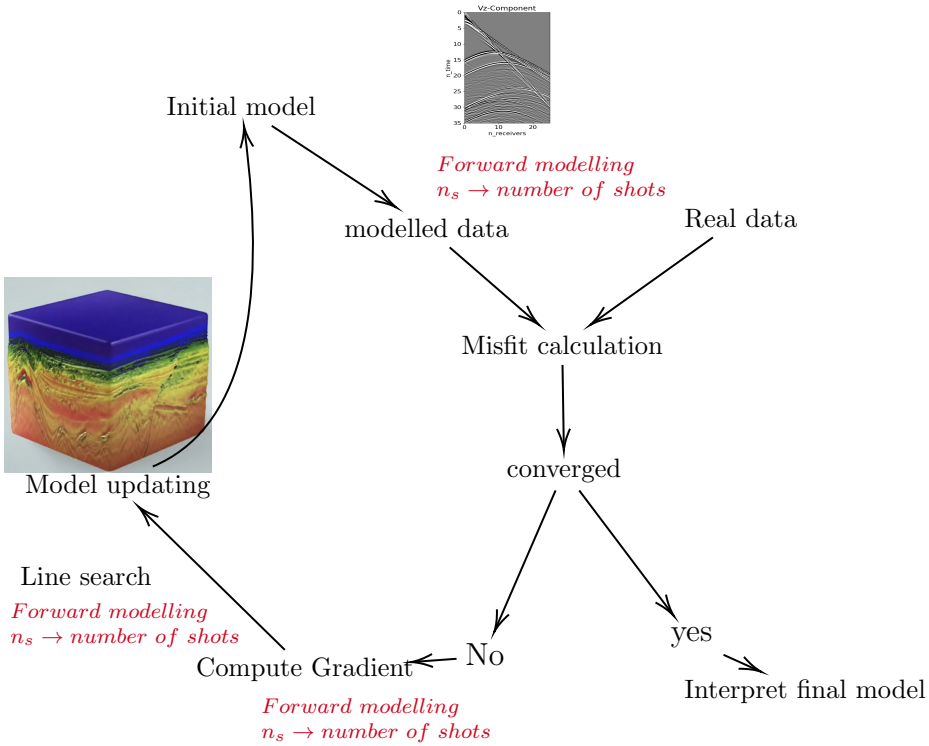

Figure 1.7: Sketch of the iterative procedure for the full waveform inversion (FWI) method. Usually, hundreds of iterations are required before a satisfactory model that explains the recorded data is found.

connects the subdomain to the homogeneous exterior. Another examples is [32], who introduce an efficient method for solving for the interaction between multiple inhomogeneous subdomains embedded in a homogeneous infinite space. The non-reflecting nature of the homogeneous medium gives exact knowledge of the arrival times for waves leaving one scattering domain and arriving at another. This locality in times makes an efficient time domain implementation possible when truncating the computational domain. Even though, these approximations are efficient, geological media are not homogeneous nor infinite.

On the other hand, [61] developed FD-injection method. The FD-injection method allows the reconstruction of wavefields after local model alterations and then propagates scattered wavefields to the receivers in the inhomogeneous background models. This technique saves significant computational memory and time compared with the conventional approach. Still, it needs to save the data around the target of interest to ensure the reconstruction, making it a memory-intensive algorithm. Another

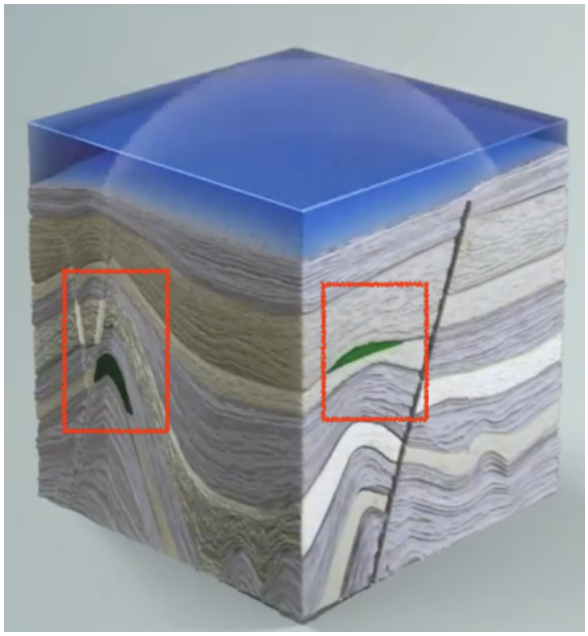

Figure 1.8: Illustration of target areas defined in a subsurface model (From [21]).

technique applicable to inhomogeneous models is the Multiple Points Sources (MPS) method proposed by [51] and studied and extended by [79, 4, 61, 87]. This is a more memory-efficient algorithm because it only requires the storage of FD quantities along a single surface in the FD grid. Figure 1.9 illustrates the surfaces that need to be saved in both (a) MPS and (b) FD-injection methods. The white represents the local computational domain, and the green is the computational boundary. Figure 1.9(a) shows the single layer (gray dots) around the local domain needed in the MPS injection method. Figure 1.9(b) illustrates the FD-injection approach in the acoustic domain, which requires half the FD stencil storage either in the computational (gray) or in the boundary (blue) domains. This figure illustrates a second-order scheme.

In the following section, the standard FD-injection method and the MPS methods are briefly introduced [61, 53]. This technique was used by [87] to implement the acoustic-elastic local solver—coupled local solver used in Chapter 2 in this thesis, and to implement the elastic-elastic local solver developed, implemented and used in this thesis – Chapters 3 and 4.

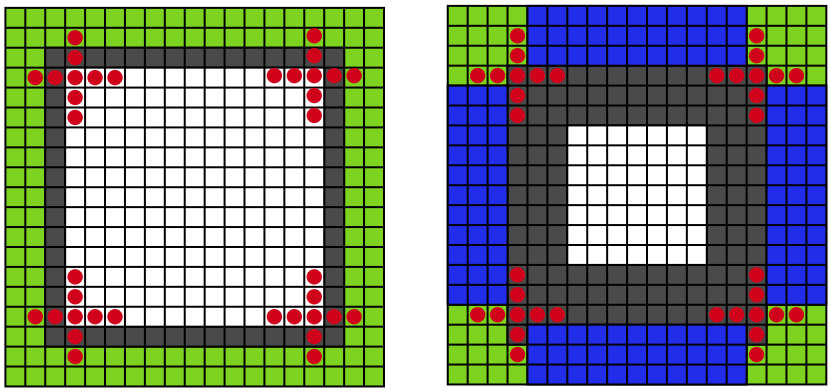

(a) (b)

Figure 1.9: Illustration of boundary layers needed in the (a) MPS and (b) FD-Injection method. The white represents the local domain and the green is the computational boundary. (a) shows the single layer (gray dots) around the local domain need in MPS injection method. (b) Illustrates the FD-injection approach in the acoustic domain which requires the storage of half the FD stencil either in the computational (gray) or in the boundary (blue) domains (second-order FD scheme is shown in this case) (Figure is based on [11]. Note that the MPS method is independent of the FD scheme order used.

1.2.1 FD-injection method

[61] introduce the local elastic solver by computing the full-domain Green's functions and the local wavefields, using the same elastic staggered grid implementation. In this study, we used the equation of motion in 2D introduced in equation 1.17. This standard local solver updates the velocities and the stress in a turn-wise manner. First, the velocities in the first two equations in 1.17 are updated. These are then used to updated the stresses, which are the last three equations in 1.17. All the equations are solved on a staggered grid with second-order accuracy in time and fourth-order accuracy in space.

Figure 1.10 shows the top-right section of the staggered elastic grid of the local solver. The symbols represent the location where the elastic wavefields in equations 1.17 are evaluated. Notice that black lines denote grid cells where the four staggered grid symbols are included. The local solver compute the perturbed wavefield within the magenta line in Figure 1.10. Note that the magenta line intersects grid cells on the boundary by design. The model can be perturbed only inside the inner blue line. This local solver requires storage of the background wavefields at all locations between

the two blue lines. By definition, when we talk about the local domain, we mean the entire local solver grid. Therefore, the local domain is the combination of the shaded and unshaded nodes, surrounded by its PML boundary condition outside the outer blue line.

The order of accuracy with which the spatial derivatives in equations 1.17 are discretized determines the width of the stencils. As an example of how the equations are discretized on the staggered grid, we show the update equation for the perturbed z-component of the velocity (equations 1.17). So, we update the velocity,

$$v_z(\mathbf{x}, t) = v_z(\mathbf{x}, t - \Delta t) + \Delta v_z(\mathbf{x}, t), \tag{1.20}$$

and using,

$$\begin{aligned}\Delta v_z(\mathbf{x}, t) = \frac{\Delta t}{\rho} \Big[& \frac{c_1}{\Delta x} \left(\tau_{zx}(x_{i+1}, z_k, t - \frac{1}{2}\Delta t) - \tau_{zx}(x_i, z_k, t - \frac{1}{2}\Delta t) \right) \\ & + \frac{c_2}{\Delta x} \left(\tau_{zx}(x_{i+2}, z_k, t - \frac{1}{2}\Delta t) - \tau_{zx}(x_{i-1}, z_k, t - \frac{1}{2}\Delta t) \right) \\ & + \frac{c_1}{\Delta z} \left(\tau_{zz}(x_i, z_{k+1}, t - \frac{1}{2}\Delta t) - \tau_{zz}(x_i, z_k, t - \frac{1}{2}\Delta t) \right) \\ & + \frac{c_2}{\Delta z} \left(\tau_{zz}(x_i, z_{k+2}, t - \frac{1}{2}\Delta t) - \tau_{zz}(x_i, z_{k-1}, t - \frac{1}{2}\Delta t) \right) \Big] .\end{aligned} \tag{1.21}$$

In equation 1.21, the staggered spatial derivatives are evaluated at the staggered time step, i.e., $t - 1/2\Delta t$ and the fourth-order accurate staggered grid coefficients c_1 and c_2 are $9/8$ and $-1/24$, respectively. On the right side, the vector $\mathbf{x}$ is decomposed in its x and z coordinates in this 2D example. An update equation similar to equation 1.21 can be derived for the propagation of the scattered v_z^{sc} in the shaded region. This updated equation replaces all perturbed wavefield quantities with their scattered counterparts. For elastic wavefield quantities other than v_z similar derivative stencils are used as those shown in Figure 1.10.

Far from the magenta boundary in Figure 1.10, the updated equations for the perturbed and scattered wavefield are simple to compute. However, within the two green lines, the derivative stencils cross the magenta line separating the locations where the perturbed and background wavefields are computed and stored. So that,

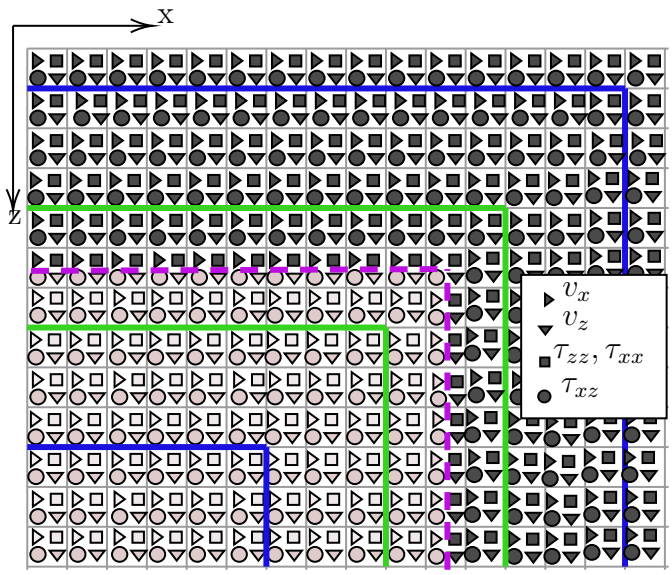

Figure 1.10: Staggered elastic grid around the top-right boundary of the elastic local solver. The model updated only inside the inner blue line. The background wavefields are saved between the two blue lines. The magenta line shows the boundary where the perturbed and scattered wavefield are compute and stored. The green lines show where the scattered and perturbed wavefields are added or subtracted to updated equation 1.21 correctly.

the updated equations for nodes between the green lines require modification. In regions where the updated stencil access the scattered τ_{zz}^{sc} at the shaded symbols in cells and the perturbed τ_{zz} in other cells, the background τ_{zz}^{0} needs to be added to the scattered τ_{zz}^{sc} to obtain the perturbed τ_{zz} and consequently update equation 1.21 correctly. This background τ_{zz}^{0} is obtained by convolving the precomputed τ_{zz}^{0} Green's functions with the source wavelet for the particular source that is simulated locally. Applying this correction to all nodes between the green lines introduces the background wavefield into the local domain where there are not model updates.

Similarly, the second stencil in Figure 1.10 has the opposite problem when updating v_z^{sc} at the shaded symbol. Part of its stencil crosses the magenta line and accesses the perturbed field τ_{xx} stored at the unfilled symbols. At these locations, we need to subtract the background wavefield from the perturbed wavefield so that we can correctly evaluate the stencil for updating the scattered wavefield at the shaded symbols. When the model is updated in the unshaded region this correctly computes the perturbed fields at the unfilled symbols and the scattered field at the filled symbols. Multiple scattering between the background model at the shaded nodes is computed

correctly.

1.2.2 Multiple Point Sources – MPS method

The modeling of seismic waves with FD method that we use in this research is carried out with the velocity-stress formulation system shown in equation 1.17. We can see that the implementation of the equivalent point source in such schemes may be written in the following form, where the representation theorem was solved [53, 1],

$$
\begin{aligned}
\frac{\partial v_x}{\partial t} &= \frac{1}{\rho}\left(\frac{\partial \tau_{xx}}{\partial x} + \frac{\partial \tau_{xz}}{\partial z}\right) + \overbrace{\left[\frac{1}{\rho}(\tau_{xx}n_x + \tau_{xz}n_z)\delta_S\right]}^{f_x(\mathbf{x}_s,t)}, \\
\frac{\partial v_z}{\partial t} &= \frac{1}{\rho}\left(\frac{\partial \tau_{xx}}{\partial x} + \frac{\partial \tau_{zz}}{\partial z}\right) + \overbrace{\left[\frac{1}{\rho}(\tau_{xz}n_x + \tau_{zz}n_z)\delta_S\right]}^{f_z(\mathbf{x}_s,t)}, \\
\frac{\partial \tau_{xx}}{\partial t} &= (\lambda + 2\mu)\frac{\partial v_x}{\partial x} + \lambda\frac{\partial v_z}{\partial z} + \overbrace{[(\lambda + 2\mu)v_x n_x + \lambda v_z n_z]\delta_S}^{h_{xx}(\mathbf{x}_s,t)}, \\
\frac{\partial \tau_{zz}}{\partial t} &= (\lambda + 2\mu)\frac{\partial v_z}{\partial z} + \lambda\frac{\partial v_x}{\partial x} + \overbrace{[\lambda v_x n_x + (\lambda + 2\mu)v_z n_z]\delta_S}^{h_{zz}(\mathbf{x}_s,t)}, \\
\frac{\partial \tau_{xz}}{\partial t} &= \mu\left(\frac{\partial v_x}{\partial z} + \frac{\partial v_z}{\partial x}\right) + \overbrace{\mu[v_x n_z + v_z n_x)\delta_S}^{h_{xz}(\mathbf{x}_s,t)},
\end{aligned}
\tag{1.22}
$$

where the first terms on the left- and right-hand are the standard velocity-stress formulation system and the last terms in all equations represent monopole sources injected on S in terms of velocity and stress. Therefore, $f_x(\mathbf{x}_s, t)$ and $f_z(\mathbf{x}_s, t)$ represent the point-source injected as velocities and $h_{xx}(\mathbf{x}_s, t)$, $h_{zz}(\mathbf{x}_s, t)$, and $h_{xz}(\mathbf{x}_s, t)$ represent the point-sources injected as stresses. δ_S denotes the delta function centered at $\mathbf{x}_s$ on the surface S. Note that the normal particle velocity is injected into the stress field and vice versa.

The effect of the equivalent point sources on the boundary to reconstruct wavefields is easy to understand visually. Figure 1.11 shows the boundary sources on S, bounding a volume V_s within a larger volume V. We can interpret the injection as the combined effect of monopole source that constructively interfere to produce the wavefields inside S while canceling the wavefields outside S. For this, we first record the stresses and particle velocities on the boundary S during a 'global simulation' within V. In a

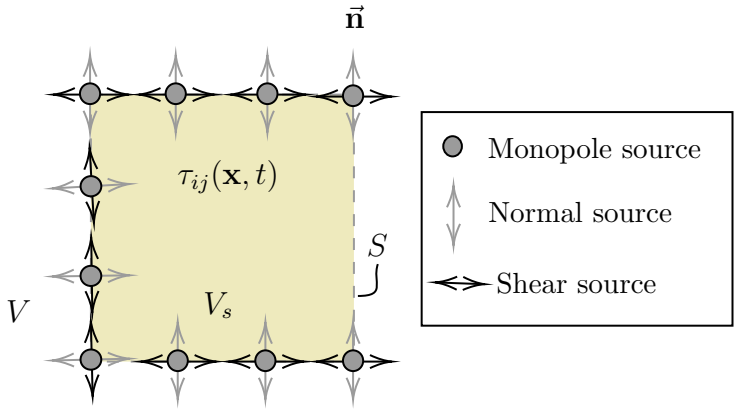

Figure 1.11: Illustration of the reconstruction of the field τ_{ij} inside S using point sources on the transparent boundary S.

second simulation, we use the given source terms (i.e., $f_x(\mathbf{x}_s,t)$, $f_z(\mathbf{x}_s,t)$, $h_{xx}(\mathbf{x}_s,t)$, $h_{zz}(\mathbf{x}_s,t)$, and $h_{xz}(\mathbf{x}_s,t)$ in equation 1.22) to keep the wavefield bounded within V_s. There are various implementations of this method, such as [51, 49, 79, 41]. The MPS method is used in this research to develop and implement an elastic local solver using Devito libraries – Chapters 3 and 4.

1.2.3 Pysit and Devito Libraries

Pysit and Devito are the libraries used in this research to develop and implement the AVO inversion algorithms for Chapter 2 and the local elastic solver and inversion algorithms for Chapters 3 and 4. Both libraries have been written in python by [35] and [47], respectively and are two collections of seismic wave modelling, solvers and inversion toolboxes. These packages are designed as testbed environments for developing advanced techniques for inverting seismic data. Chapter 3 was published in Software and Algorithms Geophysics journal and it contains an open-source software package for a Local elastic solver. Appendix A shows the steps to install Devito, all dependencies and the local solver package to reproduce the results and figures in Chapter 3.

In this thesis, first we study the impact of a coupled acoustic-elastic local solver developed by [87] on the amplitude modeled from a reflector of interest, and we use it for Amplitude VS Offset (AVO) inversion. While studying the acoustic-elastic approximation for the amplitude, we observed differences between the true curve

from a full elastic solver and the true curve modeled with the local solver. As a result, the elastic parameters were not perfectly recovered. To fix this problem, we designed an elastic-elastic local solver that generates exactly the same wavefield as a full domain solver within a local domain, using the Multiple Point Sources (MPS) methodology, which falls in the second category of wavefield reconstructions mentioned above [53]. Note that we implement the elastic-elastic local solver within an existing solver while also making it more memory efficient. This elastic-elastic local solver overcomes the mismatch in amplitude from the acoustic-elastic solver, giving an exact reconstruction of the amplitude and phase from the PP-reflection from a reflector of interest, leading to a better constraint for AVO and Phase Versus Offset (PVO) inversions. We successfully apply this elastic-elastic local solver to salt boundary inversion. Having established the utility of the elastic-elastic local solver, we then take this work to the next level by analyzing the focusing and defocusing of migrated images with Reverse Time Migration (RTM) with the ultimate goal of computing velocity updates with the local solver. We focus our analysis on the migrated image created with P- and S-wave modes. Note that the RTM method is closely related to the first update of FWI and will be introduced later on the thesis.

The main objective of this thesis is to understand the potential of local solvers under different scenarios and their applications in AVO and PVO inversions. This will enable us to assess the advantages and disadvantages of working with coupled acoustic-elastic or elastic-elastic local solvers. This study is carried out initially with a simple synthetic model, where two homogeneous half-spaces are divided by one planar interface. More complex models are also used, such as the North Sea elastic synthetic model and SEG Advanced Modeling Program (SEAM) model [23]. Finally, laboratory data obtained by [59] are used in the analysis of migrated images.

1.3 Thesis Outline and Summary of Contributions

The thesis consists of six chapters including this introduction. All chapters can be considered independent papers with their own abstract, introduction, methodology, results, discussion and conclusions. By presenting the thesis in this format the reader can read between sections with hopefully no problem. Therefore, some introductory and background material presented can be redundant.

We first introduce the background of the coupled acoustic-elastic local solver. Afterward, we evaluate the amplitude modeled from the reflector of interest and its utility in AVO inversion by recovering elastic parameters from a chalk layer and a hydrocarbon anomaly. We then focus on understanding how much the amplitude and phase contribute to the reconstruction accuracy of the elastic material parameters. Following this, we introduce a numerically exact elastic local solver theory, where we demonstrate its functionality by applying this local elastic solver to a subsection of the SEAM model. Then we compare the full-waveform inversion and the AVO and PVO inversion using the local elastic solver. We move to the next level by introducing S-wave velocity into the AVO and PVO inversion using the local elastic solver. Below, we briefly discuss the content of each chapter of this thesis and the main contributions.

Chapter 2: Amplitude variation with offset (AVO) inversion using acoustic-elastic local solver

In Chapter 2 we analyze if a coupled acoustic-elastic local solver can model the amplitude of local PP-wave reflections. This study assumes that the amplitude of the reflected PP-waves is approximately correct when using acoustic wavefield simulation. We first demonstrate that the coupled local solver propagates the P-wave with sufficient accuracy between the surface and the reflector of interest. For this purpose we use a model with two horizontal reflectors. Then, we show that the amplitude from within the local domain can be used as a constraint in recovering elastic material properties using a more complex model based on a North Sea velocity model. Then, we focus on understanding how much the amplitude and phase contribute to the reconstruction accuracy of the elastic material parameters. Our results suggest that the combination of amplitude and phase in the inversion helps with the convergence. We analyze elastic parameter trade-offs in AVO inversion. We conclude that we should invert for P-wave velocity and S-wave velocity simultaneously with fixed density to recover accurate P-wave velocities. Finally, we evaluate the sensitivity of the coupled local solver to the initial model, from which we find that we are able to recover parameters closer to the global minimum but with many local minima clustered around the global minimum resulting in a loss of accuracy in the recovered model. Having noted the acoustic-elastic solver's limitations when modelling the amplitude from PP-reflections from the local domain, this motivated us to introduce a local elastic solver

in the next chapter that models the amplitude and phase with much higher precision.

Chapter 3: Reduced memory implementation of a local elastic finite-difference solver

In Chapter 3 we introduce an elastic-elastic local solver that allows us to propagate the elastic wavefields within a subvolume after local alterations of the model. Using an elastic-elastic local solver, amplitude compensations are not needed in the transition zone around the boundary, providing an exact amplitude reconstruction. By choosing a finite-difference implementation of the local elastic solver, we have to decide the best injection method. We extend existing works by using the method of MPS to recompute the wavefield within the local domain. This method is memory efficient because it only requires the global wavefield to be recorded along the local domain boundary. By injecting these recordings as point sources, the global wavefield is emulated within the local domain. Thus, the method requires no modifications of standard FD solvers, merely the ability to record and inject data on the boundary. To conclude this chapter, we determine how the scattered wavefield due to the alterations can be extrapolated from the local domain to surface receivers. We evaluate the capability of the local elastic solver to reconstruct the wavefield in a subvolume of the elastic SEAM model.

Chapter 4: Inversion comparison using an elastic local solver to recover elastic parameters

In this Chapter we apply the local solver of Chapter 3 to a local AVO and PVO inversion problem that then is compared with FWI. First, we invert for elastic parameters using the amplitude and phase of the PP-wave reflected for a salt layer. Recovering elastic parameters from salt bodies is notoriously hard due to the high velocity contrast with surrounding sediments. Despite this difficulty, accurate recovery of the elastic parameters is an essential step for imaging and interpretation. With the amplitude and phase of the PP-wave modeled with the local elastic solver, we can recover elastic parameters with an error of less than 0.2 %. Applying FWI to the same problem, we obtain errors, on average, smaller by a factor of 10 compared to the results in the AVO and PVO inversion, i.e. 0.02 %. However, we found that the memory required for FWI is substantially larger than that for AVO and PVO investment. We also compare time costs, indicating that amplitude and phase inversion

saves around 18 % per iteration compared with FWI. Given the small error in both cases, using the phase and amplitude rather than the full wavefield may be beneficial if many re-calculations are needed.

Chapter 5: Elastic parameter recovery in a complex velocity model

Imaging and recovering parameters from structures with complex geometries and large contrast interfaces, such as salt bodies, is challenging. These conditions lead to poor illumination and weak reflectivity, which results in unfocused images. The main difficulty is the estimation and updating of the velocity model since the high-velocity contrast with the surroundings and the irregularities of the interfaces scatter and refract the incident waves to such an extent that the underlying structures are often poorly illuminated. This is a problem that is shared in geophysics and the medical field. Limitations in time and computation resources are always present. In geophysics due to the dimensionality, in medicine, because real-time results are desirable. AVO and PVO inversion using local solvers have shown promising results, suggesting that they could alleviate these challenges for both industries. However, those techniques only use amplitude and phase from the PP-reflection, therefore fail in the presence of complex scattering. In this Chapter, we take the local elastic solver of Chapter 3 to the next level, incorporating the S-wave into the objective function by measuring the focusing and defocusing of migrated images with elastic reverse time migration (RTM). Involving the S-wave in the objective function provides critical information that helps to estimate S-wave velocity in complex models. The evaluation is developed, first, in synthetic data that contain a large impedance contrast layer. Then, we analyze the migrated images using an ultrasound transverse real dataset of a polymethyl methacrylate (PMMA) tube, which mimics a bone shaft.

Chapter 6: Conclusions and Future Directions

In this chapter we summarize our major contributions and discuss some avenues for future directions.

Chapter 2

Amplitude variation with offset (AVO) inversion using acoustic-elastic local solver

2.1 Summary

Conventional amplitude variation with offset (AVO) inversion analysis uses the Zoeppritz equations, which are based on a plane-wave approximation. However, because real seismic data are created by point sources, wave reflections are better modeled by spherical waves than by plane waves. Indeed, spherical reflection coefficients deviate from planar reflection coefficients near the critical and postcritical angles, which implies that the Zoeppritz equations are not applicable for angles close to critical reflection in AVO analysis. Elastic finite-difference simulations provide a solution to the limitations of the Zoeppritz approximation because they can handle near- and postcritical reflections. We have used a coupled acoustic-elastic local solver that approximates the wavefield with high accuracy within a locally perturbed elastic subdomain of the acoustic full domain. Using this acoustic-elastic local solver, the local wavefield generation and inversion are much faster than performing a full-domain elastic inversion. We use this technique to model wavefields and to demonstrate that the amplitude from within the local domain can be used as a constraint in the inversion to recover elastic material properties. Then, we focus on understanding how much the amplitude and phase contribute to the reconstruction accuracy of the elastic material

parameters (v_p, v_s, ρ). Our results suggest that the combination of amplitude and phase in the inversion helps with the convergence. Finally, we analyze elastic parameter trade-offs in AVO inversion, from which we find that to recover accurate P-wave velocities we should invert for v_p and v_s simultaneously with fixed density.

2.2 Introduction

The study of how the amplitude of a reflected wave varies with offset or angle (AVO or AVA) has long been of interest in geophysics because P- and S-wave velocities (and their anisotropy), along with density, determine the value of the reflection coefficient. To relate the reflection coefficient to these material properties, [102] defines equations that describe the reflection coefficients as a function of the incidence angle. However, the [102] equations and all of the ensuing approximations [2] are based on plane waves, which only sample one incoming angle. Moreover, all of these approximations are derived under the same assumptions: small changes in P- and S-wave velocities and density across the interface and near vertical angles of incidence. These assumptions limit the applicability of conventional AVO inversion from small to moderate offsets. One way to bypass this limitation is to use finite-difference elastic modeling with a point source, which simulates the spherical full waveform. In spherical full-waveform simulations, the associated reflection coefficients incorporate more than one incoming angle and thereby include additional information from adjacent slownesses within the first Fresnel zone of the reflection point. This additional interference allows a smooth transition around the critical angle in spherical reflection coefficient AVO curves [22].

Spherical full-waveform inversion (FWI) methods seek to exploit the full information content of the seismic wavefield recorded over a broad range of incidence angles, to build subsurface models with a broad range of wavenumbers [58, 84]. However, for FWI methods, one must choose the best strategy to forward model the data, and even the simplest full-waveform method is likely to be more computationally expensive than plane-wave methods.

There are several alternative forward simulations that model large angle reflection, for instance, [101] present a methodology in which spherical waves are decomposed into the plane-wave domain using a (τ, p) transform. Even though this method determines the P-wave reflection coefficients with acceptable accuracy compared to P-wave

reflection coefficients modeled by conventional plane-wave approximations, it does not model the finite-frequency effects of wavefield propagation. [99] compare phase information from pre and postcritical reflections using plane and spherical waves and then use a least-squares scheme to invert the modeled phase variation with angle (PVA) and AVO for four elastic parameters (density and three velocities — two for one layer and one for the other layer), showing that when the observed and predicted phases are consistent, the method finds the correct solution.

In general, spherical wavefield modeling is expensive because we need to solve the wave equation for a large domain. Specifically, we need to use a model large enough to include all regions of the subsurface through which we expect waves to pass for a particular survey, even though we are interested in only a small area of the subsurface. To speed up the inversion process, [61] approximate the full elastic wavefield with high accuracy within a locally perturbed subdomain of the full domain and then propagate this wavefield to the receivers in an inhomogeneous background model. Their formulation discards part of the perturbed wavefield that scatter outside the region of interest and subsequently reenter the subdomain. A time-reversal mirror introduced by [49] makes the same approximation; therefore, both methods do not generate the exact local wavefield. [78] and [88] introduce an exact acoustic domain truncation that works for inhomogeneous background models in the time and frequency domain, respectively. [87] propose coupling a local elastic solver with a background acoustic model to estimate PVA, based on the interest in recovering detailed elastic parameters in only a limited part of the subsurface. In this method, they use an acoustic solver to propagate the wavefield to a subdomain in which the local elastic solver from [61] is implemented, avoiding the calculation of full-domain elastic Green's functions, but incorporating elastic physics in the region of interest. Their study focuses on the phase of reflected waves. They approximate propagation between the surface and this elastic reflector of interest with acoustic physics because the acoustic and elastic propagation provide similar estimates of the wavefield phase. Then, they use the modeled PVA to invert for elastic material properties.

Here, we extend that work to see if a constant-density acoustic elastic (CDA-EL) local solver can accurately model the amplitude of local PP-wave reflections. We justify this study based on the idea that the amplitudes of the reflected PP-waves are approximately correct when using acoustic wavefield simulations. In addition, although we expect better accuracy when using the correct velocity model and elastic

propagation, it is not clear that elastic propagation will be more accurate when only an approximate velocity model is available. We show that the CDA-EL local solver propagates the P-wave with a sufficient accuracy between the surface and the reflector of interest. In addition, the CDA-EL local solver is faster than either a full elastic solver or an elastic-elastic local solver [61, 10]. After this, we investigate whether the amplitude modeled by the CDA-EL local solver can be used as an additional constraint to invert for the P- and S-wave velocities and density (v_p, v_s, ρ, respectively) at a reflector of interest.

Despite the fact that interparameter trade-off is an area of interest in FWI, there is still a paucity of literature discussing how the different elastic parameters trade off with one another in AVO inversion. This is our focus in the second part of this study. Multiparameter FWI concerns recovering more than one parameter (i.e., the P- and S-wave velocities and density) for rock property identification, reservoir prediction, and lithologic characterization. When simultaneously inverting for multiple elastic parameters, perturbations of one parameter may be mapped into the estimation of another, making interparameter trade-off challenging [57]. [54] discuss some FWI factors that help to determine the trade-off between the velocities of the P- and S-waves, density, attenuation, and anisotropic parameters, based on the radiation patterns in viscoelastic anisotropic media. [27] propose an algorithm for total variation regularized nonlinear multi-interface AVO inversion based on the Zoeppritz equations to estimate P-wave velocity, S-wave velocity, and density simultaneously. In this paper, we study the trade-off between the amount and type of data used as an input to the inversion and the accuracy of the inverted elastic parameters (v_p, v_s, ρ), as well as the potential trade-offs between them, using the CDA-EL local solver.

2.3 Methods

In this section, we review the general aspects of the elastic local solver that we use to model the forward wavefield. The elastic local solver that we use is based on the one described by [61] and modified by [87] to evaluate the PVA. This modification involves propagating the wavefields using an acoustic solver to a subdomain on which we use the elastic solver. This CDA-EL local solver produces a scattered wavefield within a local domain in which waves that scatter inside and outside the local domain

(e.g., multiples) are discarded.

Figure 2.1 shows a schematic of the CDA-EL solver. The CDA-EL solver requires the Green's functions for the acoustic background, which are represented by the dashed black lines inside the large white box. This is where we have significant computational and memory savings by using an acoustic, rather than an elastic, solver because the CDA Green's functions are less expensive to compute than the EL Green's functions. The Green's functions in the background are connected through an injection/recording boundary (red box) to the local elastic subdomain represented by the blue box. Between the red and blue boundaries, the model transitions from an elastic media (inside the blue box) to an acoustic media (outside the red box). We update the model only in the elastic subdomain (blue box), which contains the PP-reflection response that we want to model. The dark-red boxes surrounding the full and local domain represent the perfectly matched layer boundary condition. Here, we summarize the basic ideas of the local solver; additional details are described in [87].

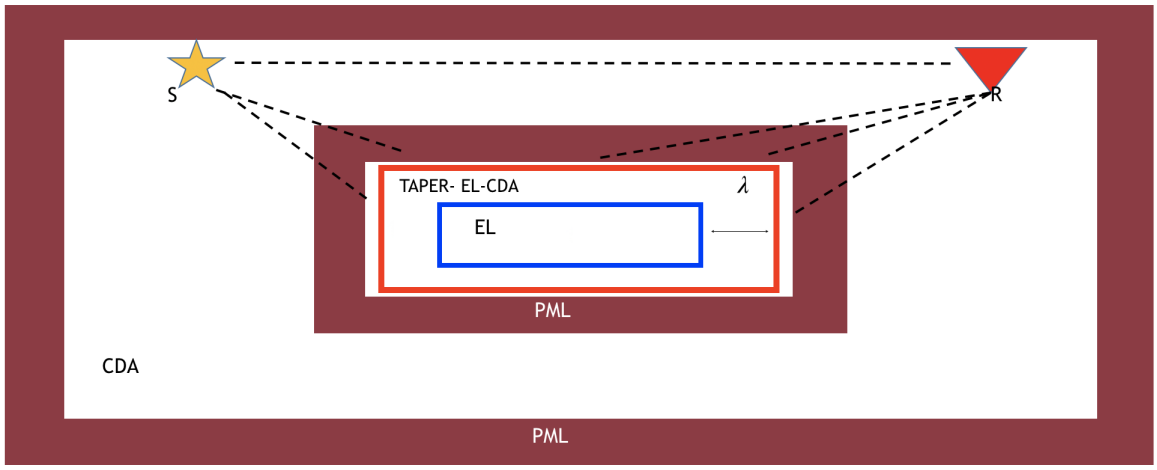

Figure 2.1: Schematic of the CDA-EL local solver. The star represents the source, and the triangle represents the receiver. The wavefield is updated by the local solver within the blue box. We taper the velocity model from acoustic to elastic through the region between the red and blue boxes. Further explanation is shown in the "Method" section. Based on [87].

To calculate the Green's functions, we use a standard CDA code implemented in PySIT [35]. We use an extension of this code, developed by [90] to calculate the boundary integral along the blue box shown in Figure 2.1. The boundary integral computes the scattered pressure, p, on the boundary S using equation 2.1:

$$p^{sc}(y,t) = \int_S l_\rho^{rec}(x) l_{v_s}^{rec}(x) \left[G_0(x,y,t) * \frac{\partial p^{sc}(x,t)}{\partial x_n} - p^{sc}(x,t) * \frac{\partial G_0(x,y,t)}{\partial x_n} \right] dS_x, \quad (2.1)$$

where $l_\rho^{rec}(x)$ and $l_{v_s}^{rec}(x)$ are approximate inverses of the injection compensation factors (Figure 2.2), $G_0(x,y,t)$ is the CDA background Green's function between the boundary x and the evaluation position y, $*$ denotes the convolution and $\partial/\partial x_n$ represents the normal derivative. The boundary integral propagates, to the receiver position y, any scattered wavefield generated by a perturbation added to the background, i.e. variations in P- and S-wave velocities and density inside the red box. However, we need to apply extra compensation in the amplitude because $\rho(x)$ and $v_s(x)$ are variable along the injection boundary or between the source and receiver locations. [90] proposes a workflow with amplitude compensation factors. Figure 2.2 illustrates the steps in the procedure. Once we compute the amplitude of the reflected wavefields at the receiver positions, we proceed to obtain the reflection coefficient values as a function of angle.

2.3.1 Measuring the Amplitude

To measure the amplitude of a wavefield, we isolate an event and pick the amplitude independent of the phase. To do this, we first pick a window that includes the reflection of interest, and then we use equation 2.2 for the computation of the envelope from which we take the maximum value of each analytic trace; i.e., we compute

$$\Upsilon_{amp} = \text{Max}(|\text{Hilbert}(\text{trace})|). \quad (2.2)$$

Υ_{amp} represents the amplitude obtained, $|.|$ represents the absolute value and trace represents the windowed trace.

2.3.2 Measuring the Phase

To measure the phase of the wavelet, we adopt the method used by [90] who follows [99]. The idea is based on the observation that a zero-phase wavelet has maximum correlation with its envelope [24]. We use a grid-search procedure, with a grid over phase, then phase rotate the wavelet in 1° increments and compute the correlation

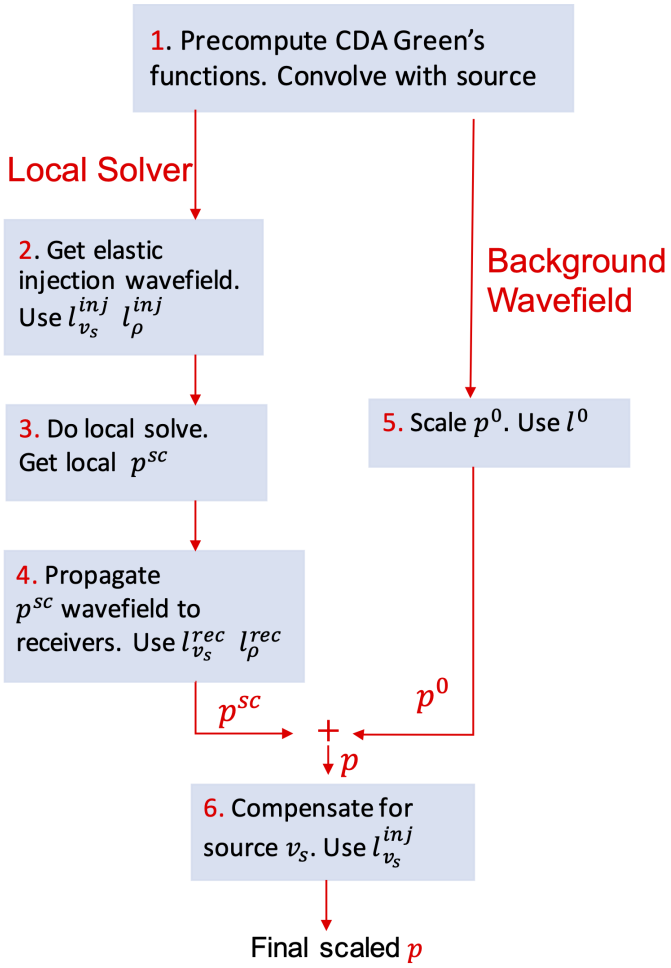

Figure 2.2: Workflow applied to compensate for amplitude differences. The amplitude compensation factors ($l_{v_s}^{inj}$, l_{ρ}^{inj} $l_{v_s}^{rec}$, l_{ρ}^{rec} and l^0) are defined in [90].

with the envelope of this shifted wavelet. Then, the measured phase is the location of the maximum of this correlation function.

2.3.3 Amplitude evaluation

Two layer model

To evaluate if the CDA-EL local solver can accurately model the amplitude of a local PP-reflection, we use the local solver on a simple two-layer model. In the CDA-EL local solver, we taper the elastic true model to constant density and S-wave velocity at its boundary. Then, we verify if the amplitude of the PP-reflection in this tapered

simulation is similar to that of the true elastic model and to the Zoeppritz equation.

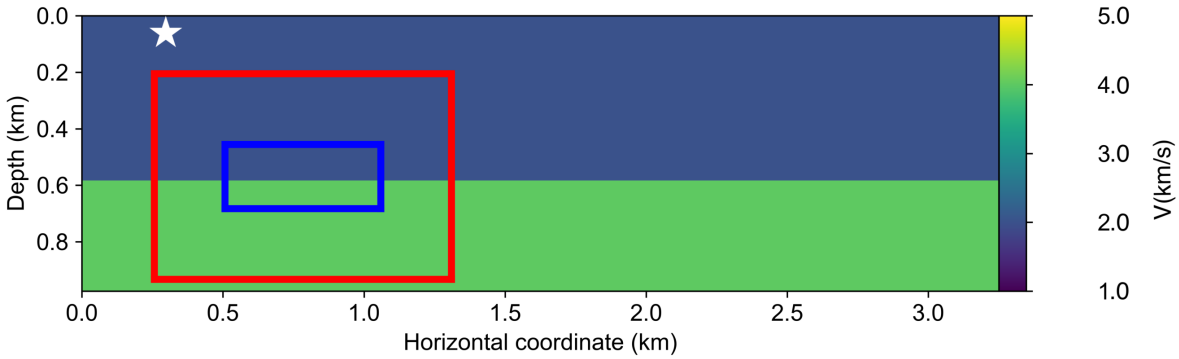

Figure 2.3: P-wave velocity model of the two layer true elastic model with a source at $x = 0.351$ km and $z = 0.1$ km (white star). Model properties: top layer ($v_p = 2000$ m/s, $v_s = 880$ m/s, $\rho = 2000$ kg/m^3), bottom layer: ($v_p = 4000$ m/s, $v_s = 1540$ m/s, $\rho = 2300$ kg/m^3).

The P-wave velocity of the true elastic model is shown in Figure 2.3. The S-wave velocity and density models are tapered using an exponential taper from an EL model inside the blue box to a CDA model at the red box. The size of the taper is the same on all sides with a length of 240 m, which is three times the maximum wavelength (λ_{max}) in the top layer when $f = 25$ `Hz` (i.e., $3\lambda_{max}$). The values for the P- and S-wave velocities and density (V_p, V_s and ρ, respectively) for each layer are given in the figure caption of Figure 2.3. We place the source at $x = 0.35$ km and $z = 0.10$ km and receivers along the top of the model at $z = 0.10$ km. The source is a Ricker wavelet with a peak frequency of 25 `Hz` (Figure 2.3).

Figure 2.4a shows the AVA modeled with the full EL solver on the true model (blue line: Full EL-True), the full EL solver on the tapered model (red +: Full EL-Model Tapered), the CDA-EL local solver on the tapered model (magenta line: CDA-EL Local), and the Aki-Richards approximation for P-wave reflection coefficient (green line: Zoepp Rpp). The red and magenta lines show the same pattern, demonstrating that the CDA-EL local solver is implemented correctly for this geometry. The amplitude of the reflection for the red and magenta lines shows an irregular behaviour in the first 25° and after 50°, which are associated with the size of the taper and the size of the local elastic domain. First, we test the taper size. We change the taper length from ($3\lambda_{max}$) to ($5\lambda_{max}$) to investigate how the curves modeled with full EL domain on the tapered model (red +: Full El -Model Tapered) and with the CDA-EL local solver (magenta line: CDA-EL Local) get closer to the Full EL domain solver (blue

line: Full EL-True)(Figure 2.4b).

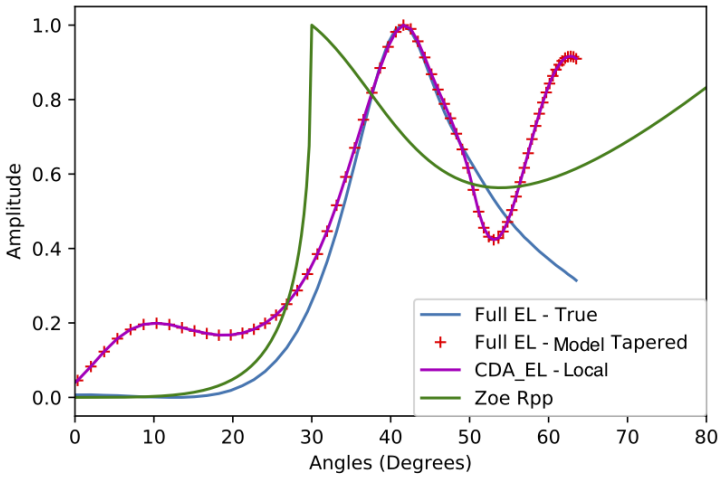

(a) AVA- three wavelength taper

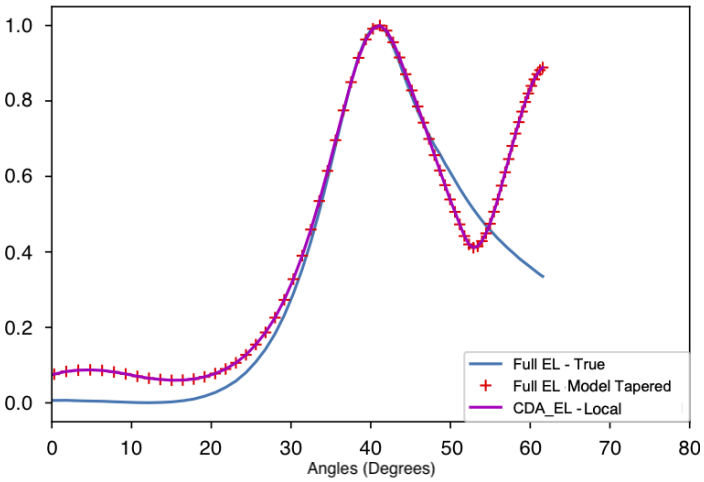

(b) AVA- five wavelength taper

Figure 2.4: The AVA modeled using the three-wavelength taper and (b) AVO modeled using the five-wavelength taper transition. Results are shown for the full EL domain solver (blue line: Full EL-True), the full EL domain with an elastic local solver (red +: Full EL-Local Tapered), the full CDA domain with an EL local solver (magenta line: CDA-EL Local Tapered), and the Zoeppritz equations for the P-reflection coefficient (green line: Zoe Rpp). All of the reflection coefficients are normalized to increase from zero to one using equation 2.3.

Second, we test the size of the local elastic solver.We increase the length of the local elastic domain from 1.4 to 2.7 km (Figure 2.5a) and we use a three-wavelength taper. In this case, the CDA-EL amplitude curve shows a behavior closer to the full

EL domain solver after 45° as we expect. However, they do not match perfectly, which suggests that the artifacts in the curves are the result of a combination of the size of the taper, the size of the local domain, and the position of the source. However, the behavior of the curves between 25°and 48° remains relatively accurate even when using the shorter taper and small elastic local domain; therefore, we choose to work with the short taper and small local domain (Figure 2.4b). The taper and elastic local domain can be made larger if higher amplitude precision is required, though when a larger taper and local domain are used the computational cost increases, which may change the balance between the computational cost of the CDA-EL local versus an elastic to elastic solver (e.g. [61]). However, some of the accuracy gains in using the elastic to elastic solver may be lost when we do not know the overburden accurately. It is worth noting that the position of the reflector is quite shallow; a deeper reflector would move the peak of the curve closer to the Zoeppritz approximation because the Fresnel zone would reduce to a point where only one incoming angle would contribute and effectively simulate a plane wave. We do not expect to obtain agreement with the Zoeppritz result as this assumes plane waves. Instead, we expect the result to agree with the Full EL-True result. Note that the values of the amplitude in the first 25° for the full EL domain and Zoeppritz equation are close to zero, but they are not actually zero(Figure 2.4b).

Thus far, we have found that the CDA-EL local solver is able to accurately estimate the amplitude for angles between 25° and 48°, using a homogeneous model. In the following example, we illustrate the technique with a more realistic model based on the geology of the North Sea.

North Sea Model

To evaluate how the overburden heterogeneity affects the amplitude modeling with the CDA-EL local solver, we introduce a more complex and realistic model designed to resemble the geology of the North Sea. Using the same configuration as used for the two-layer model, we evaluate the amplitude of the PP-reflected wave. Because we investigate whether or not the CDA-EL local solver can accurately model the local PP-reflection in this more complicated North Sea model, we only compare the result with the reflection obtained using the full EL domain solver.

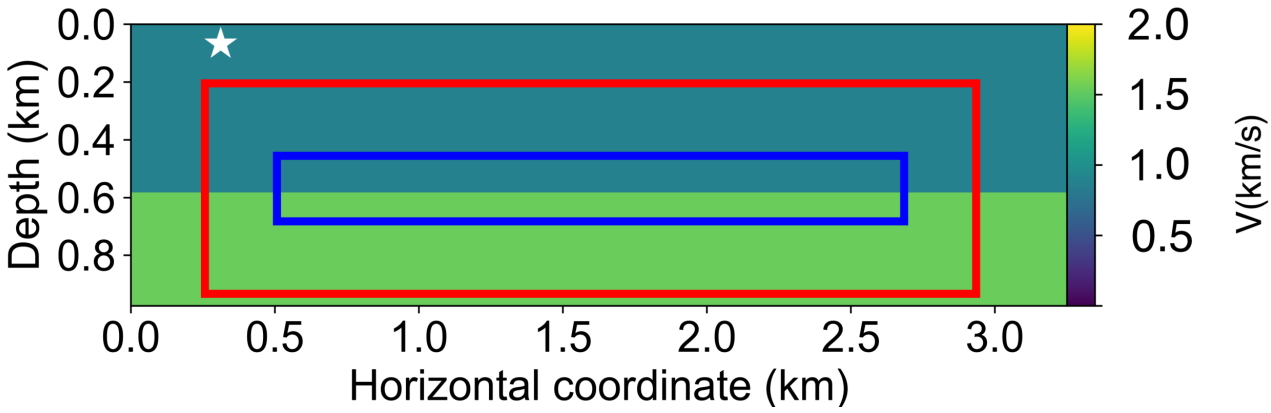

(a) S-wave velocity model

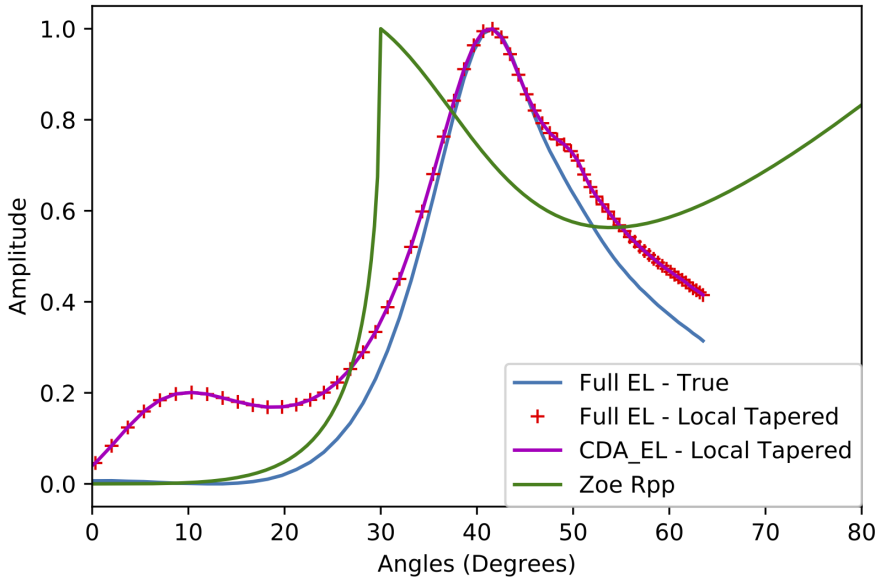

(b) AVA

Figure 2.5: (a) The S-wave velocity model of the two-layer true elastic model with a source at $x = 0.351$ km and $z = 0.1$ km (white star). The model properties are described in Figure 2.3. The blue box represents the elastic local domain that is increased from 1.4 km to 2.7 km and the red box is a three-wavelength taper transition region. (b) AVO modeled using the model depicted in (a). Results are shown for the full EL domain solver (blue line: Full EL-True), the full EL domain with an elastic local solver (red +: Full EL-Local Tapered), the full CDA domain with an EL local solver (magenta line: CDA-EL Local Tapered), and the Zoeppritz equations for P-reflection coefficient (green line: Zoe Rpp). All of the reflection coefficients are normalized to increase from zero to one using equation 2.3.

Figure 2.6 shows the P-wave velocity model based on North Sea geology, characterized by high-velocity layers that represent a chalk layer and a small velocity

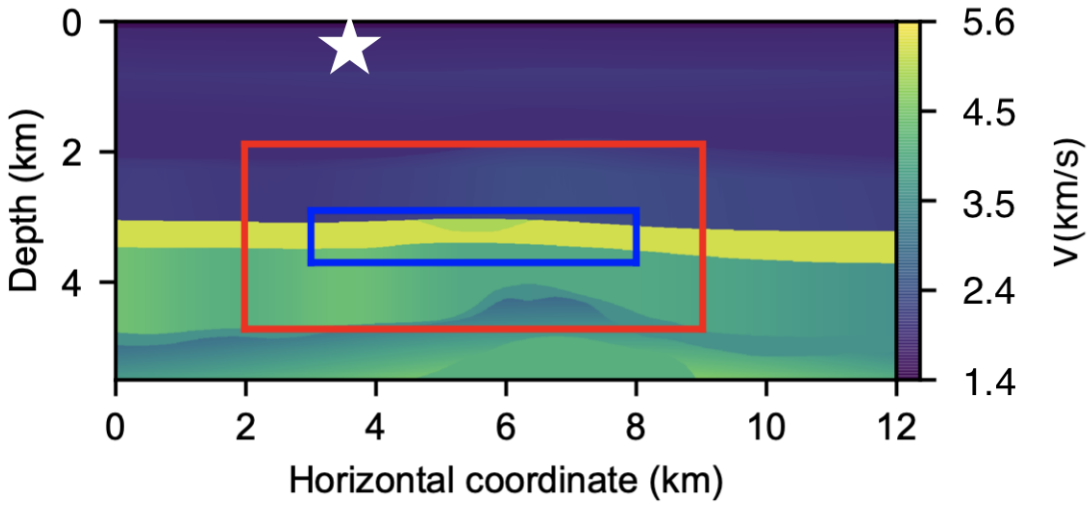

Figure 2.6: The P-wave velocity based on the geology of the North Sea with a source at $x = 3.5$ km and $z = 0.1$ km (white star). The blue box is the region in which we use the fully elastic local solver, and the area between the blue and red boxes is the region in which we apply a taper from the EL to the CDA models.

decrease, which represents the presence of hydrocarbons (at roughly $x = 5.5$ km and $z = 3.0$ km). In this example, the density model with a range of $(1000, 2600)$ kg/m^3 and the S-velocity model with a range of $(0, 3200)$ m/s are derived using Gardner's equation and assuming a Poisson solid, respectively. Thus, the combination of P-velocity, S-velocity, and density make up the true elastic Earth model. From this Earth model, we expect to obtain strong postcritical reflections due to the contrast in P-wave velocity at the boundary of the chalk layer, which is our zone of interest (blue box shown in Figure 2.6). The overburden density model is finely layered; however, the average value of the density above the hydrocarbon anomaly and chalk layer is 2000 kg/m^3. The difference between the chalk and the overburden layer densities is 350 kg/m^3 (Table 2.1), implying a negative contrast between these two layers. The modeled source wavelet has a peak frequency of 6.0 Hz and is located at $x = 3.5$ km and $z = 0.1$ km. The receivers are placed continuously between 5.0 km and 10 km horizontally at 0.1 km in depth, with 10m spacing.

This is a situation in which "normal" AVO is likely to fail because of the presence of postcritical reflections. In addition, a straight acoustic approach is unlikely to work

Table 2.1: The P- and S-wave velocities for the hydrocarbon anomaly and the bulk chalk. The parameters are inverted using the amplitude only with three shots.

Hydrocarbon anomaly				
	True	Initial	Amplitude Inverted	Error
v_p(km/s)	5.00	4.30	4.76	4.82%
v_s(km/s)	2.86	2.20	282	1.26%
ρ(kg/km^3)	2.35	2.10	2.29	2.14%
Chalk layer				
	True	Initial	Amplitude Inverted	Error
v_p(km/s)	5.30	4.60	5.11	3.5%
v_s(km/s)	3.06	2.60	3.05	0.32%
ρ(kg/km^3)	2.65	2.30	2.71	2.54%

because this phase transition depends on the model being elastic. It is also important to keep in mind that we are looking at elastic effects on PP-reflections, which is why the acoustic approximation may still be sufficiently accurate outside the domain of interest. We also note that the corrected acoustic simulation contains some elastic effects without the full cost of an elastic simulation. It does not contain any S-waves, but amplitudes of reflected PP-waves are approximately corrected [10].

Figure 2.7 shows the amplitude modeled using the full EL solver (blue line: Full EL-True), and the CDA-EL local solver (magenta line: CDA-EL Local). From this graph we see how other events intersect with the chalk reflection and as a result the amplitude values oscillate rapidly. For instance, the region between 43° and 50° corresponds to receivers located between $x = 9$ km and $x = 11$ km where the combination of the direct wave and ocean bottom reflection intersect the chalk reflection [87]. Due to the superposition of this event with the chalk reflection, the total reflection will have a different picked amplitude than that of the chalk reflection alone.

We propose to mute the positions where other events cross the chalk reflection to calculate the amplitude. The mute windows for the source at $x = 3.5$ km are shown with gray shading in Figure 2.7. After muting, we obtain the amplitude for only the PP-reflection from the area of interest. Comparing them, we see that the PP-reflection is affected primarily by scattering at the reflection and is less influenced by propagation through the elastic overburden, which agrees with observations from

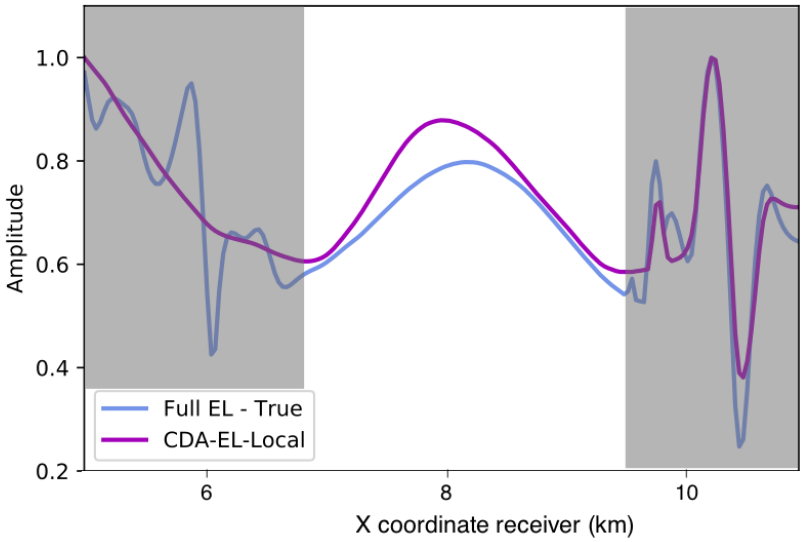

Figure 2.7: Modeled amplitude for a source located at x=3.5km using full EL solver (blue line: Full EL-True) and CDA-EL local solver (magenta line: CDA-EL Local Tapered). The gray windows correspond to areas that are muted because they interfere with the PP-wave reflection from the chalk.

[99]. Even though we do not obtain an exact match between the two curves, we will see that the approximation is still good enough to use the CDA-EL local solver to model amplitudes from PP-reflected waves, using models that contain an overburden from homogeneous to moderately heterogeneous.

For display purposes, we normalize the amplitude curves (Figures 2.4a, 2.4b, and 2.7) using,

$$A_{norm} = \frac{A(x) - A_{min}}{A_{max} - A_{min}}, \tag{2.3}$$

where $A(x)$ represents the amplitude at position x and A_{min} and A_{max} are the minimum and maximum values, repectively.

2.3.4 Amplitude Inversion

[87] perform a phase inversion. They measure the phase of the wavelets, using the observation that a zero-phase wavelet has maximum correlation with its envelope (operator Υ_{amp} defined in equation 2.2). Here, we investigate whether the amplitude

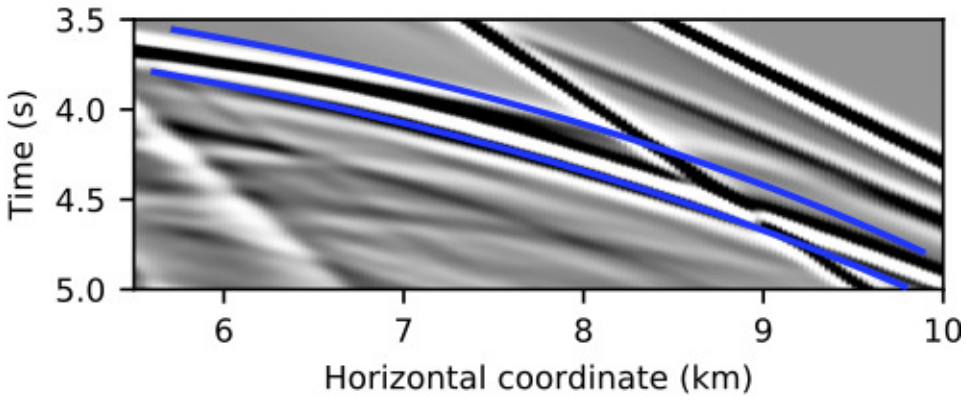

Figure 2.8: Shot gather for a source at $x = 3.5$ km generated on the true North Sea elastic model. The blue lines delineate the window used to measure the amplitude and phase of the PP- wave reflection.

of the reflection event generated by the local solver can also be used to invert for material parameters at a reflector of interest. Specifically, we minimize the objective function:

$$\Gamma(\mathbf{m}) = \frac{1}{2}\,||\Lambda(\mathbf{d}) - \Lambda(F(\mathbf{m}))||_2^2\,, \tag{2.4}$$

where F represents the CDA -EL local solver, $\mathbf{d}$ the recorded data, and $\mathbf{m}$ the model vector. To minimize equation 2.4, we extract the values of phase and amplitude from $\mathbf{d}$ and $F(\mathbf{m})$ applying the operator Λ as,

$$\begin{aligned} \Lambda(\mathbf{d}) &= (\nu_{\mathbf{P}}; \nu_{\mathbf{A}}) \\ \Lambda(F(\mathbf{m})) &= (\zeta_{\mathbf{P}}; \zeta_{\mathbf{A}}). \end{aligned} \tag{2.5}$$

where $(\nu_{\mathbf{P}}; \nu_{\mathbf{A}})$ and $(\zeta_{\mathbf{P}}; \zeta_{\mathbf{A}})$ represent vectors that contain phases $(\nu_{\mathbf{P}}, \zeta_{\mathbf{P}})$ and amplitudes $(\nu_{\mathbf{A}}, \zeta_{\mathbf{A}})$ of the recorded and modeled data. The term $\Lambda = (\Upsilon_{phase}, \Upsilon_{amp})$ with Υ_{amp} (equation 2.2) and Υ_{phase} as described above.

Writing out equation 2.4 produces

$$\Gamma(\mathbf{m}) = \left|\left| a\frac{\nu_{\mathbf{P}} - \zeta_{\mathbf{P}}}{max(\nu_{\mathbf{P}})} \right|\right|_2^2 + \left|\left| b\frac{\nu_{\mathbf{A}} - \zeta_{\mathbf{A}}}{max(\nu_{\mathbf{A}})} \right|\right|_2^2, \tag{2.6}$$

where $max(\nu_{\mathbf{P}})$ and $max(\nu_{\mathbf{A}})$ are the maximum values of the phase and phase of the recorded and modeled data, respectively, defined in equation 2.5, and a and b are

constant values that oscillate within (0 to $max(\nu_{\mathbf{P}})$) for the phase and (0 to $max(\nu_{\mathbf{A}})$) for the amplitude, respectively. Terms a and b give different weights to the phase and amplitude during the inversion; however, for this study we used $a = max(\nu_{\mathbf{P}})$ and $b = max(\nu_{\mathbf{A}})$; we do not explore these parameters further. The amplitude and phase are functions of the elastic parameters (v_p, v_s, ρ) in the layer of interest.

To estimate the best-fitting model, we use the Gauss-Newton inversion method. Suppose that our starting model $\mathbf{m_0}$ is relatively close to the true model and the misfit function $\Gamma(\mathbf{m})$ is expanded in a Taylor series retaining up to the second order terms [75],

$$\Gamma(\mathbf{m}) = \Gamma(\mathbf{m_0}) + \Delta\mathbf{m} \bigtriangledown \Gamma(\mathbf{m})|_{\mathbf{m}=\mathbf{m_0}} + \frac{1}{2}\Delta\mathbf{m}^t \bigtriangledown^2 \Gamma(\mathbf{m})|_{\mathbf{m}=\mathbf{m_0}}\Delta\mathbf{m} \tag{2.7}$$

where superscript t denotes matrix transposition. Minimizing equation 2.7, to acquire the optimal parameters (e.i., the closet minimum around $\mathbf{m}_0$), we differentiate equation 2.7 with respect to the model parameters and set it equal to zero,

$$\frac{\partial\Gamma(\mathbf{m})}{\partial\mathbf{m}} = \bigtriangledown\Gamma(\mathbf{m})|_{\mathbf{m}=\mathbf{m_0}} + \Delta\mathbf{m}^t \bigtriangledown^2 \Gamma(\mathbf{m})|_{\mathbf{m}=\mathbf{m_0}} = 0, \tag{2.8}$$

where $\Delta\mathbf{m} = \mathbf{m} - \mathbf{m}_0$. Hence, the minimum is achieved by arranging equation 2.8,

$$\Delta\mathbf{m} = -\mathbf{H}(\mathbf{m}_0)^{-1} g(\mathbf{m}_0), \tag{2.9}$$

where $g(\mathbf{m}_0) = \bigtriangledown_m \Gamma(\mathbf{m})|_{\mathbf{m}=\mathbf{m_0}} = \mathbf{J}_i^t \mathbf{r}_i$ is the gradient and $\mathbf{H}(\mathbf{m}_0) = \{\mathbf{J}_i^t \mathbf{J}_i\}$ is the approximate Hessian. Therefore the search direction $\Delta\mathbf{m}$ at iteration i is,

$$\Delta\mathbf{m}_i = -\{\mathbf{J}_i^t \mathbf{J}_i\}^{-1} \mathbf{J}_i^t \mathbf{r}_i. \tag{2.10}$$

We then update the model $\mathbf{m}_i$ to $\mathbf{m}_{i+1}$ via $\mathbf{m}_{i+1} = \mathbf{m}_i + \alpha_i \Delta\mathbf{m}_i$, where α_i is the step length. In this paper, a value of α is determined at each iteration by using the backtracking line search algorithm. This is the same methodology as that of [87].

2.4 Results

In this section, we discuss the inversion results, using the North Sea model. Following this, we evaluate the relationship between the amount of data and the improvement of the inversion results, when adding more information from more shots into the inversion, and evaluate the trade-off between the elastic parameters. Finally, we evaluate the sensitivity of the objective function to the starting model using the CDA-EL local solver.

2.4.1 Inversion with North Sea model

Amplitude inversion

We investigate if the amplitude of the reflection event, generated by the CDA-EL local solver, can be used to invert for material properties at a reflector of interest. We do this by minimizing the least squares objective function (equation 2.4). Following [87], we assume that the overburden is known. We use the exact properties at the source and receiver locations using the compensation factors explained above (Figure 2.2). We invert only for the material properties of the chalk and hydrocarbon anomaly located at $x = 5.75$ km. We invert for six parameters, three for the chalk and three for the hydrocarbon anomaly (v_p, v_s and ρ, respectively for each). We identify the hydrocarbon anomaly parameters with the number 1 and the chalk parameters with the number 2. The amplitude is not normalized during the inversion, and we are not using the phase, effectively setting $a = 0$ in equation 2.6.

We first evaluate the amplitude curve. Figure 2.9 shows the evolution of the amplitude at iterations 0, 1, 2, 3, and 6, using dashed lines. The amplitude curves show how the amplitude residual becomes smaller as the inversion progresses. Figure 2.10a shows the evolution of the model $\mathbf{m}_i$ as a function of iteration number i for three shots located at $x = 2.5$ km, 3.0 km and 3.5 km. All curves are normalized using the true value; hence, all of the curves should approach 1.0 for the perfect case. Due to the difference between the true curve (blue line: Full EL-True) and the true local curve (magenta line: CDA-EL Local), we do not expect to obtain a perfect recovery of the elastic parameters. We see that the modeled amplitude is able to recover velocities with an error of less than 5% (Table 2.1), but not densities which is not a surprise. This

density overestimation could be the inversion trying to compensate for the difference between the true and local true amplitude curves. Another possible reason that can result in the overestimation of the densities is the differences in the sensitivities of seismic data with respect to the velocity and density, making the inversion poorly constrained. Moreover, the patterns of diffraction of velocity and density are similar at small scattering angles [75, 52, 25].

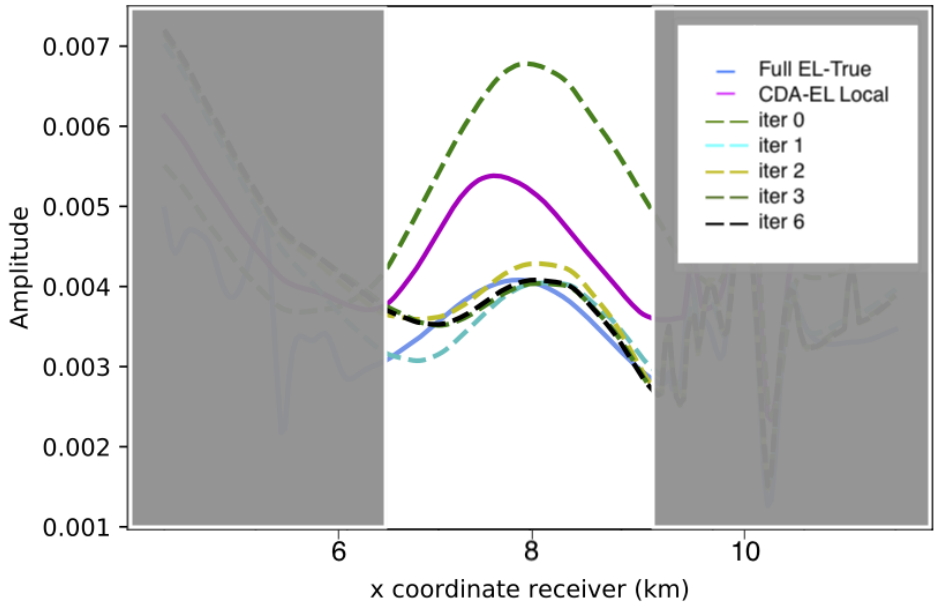

Figure 2.9: Amplitude for source at $x = 3.5$ km over several inversion iterations. The grayed regions are muted and are not included in the inversion.

There are techniques to approach these issues; however, this is outside of the scope of this paper (see e.g., [12], and [94]). Figure 2.10b shows the objective function values during the inversion, and the dashed line shows the value of the objection function for the true model. It is apparent that continuing with more than six iterations does not lead to the true value because the inverted model already has a lower objective function value than the true model. We calculate the error between the true (V_t) and inverted (V_e) value using,

$$\%Error = \frac{V_t - V_e}{V_t} * 100\%. \tag{2.11}$$

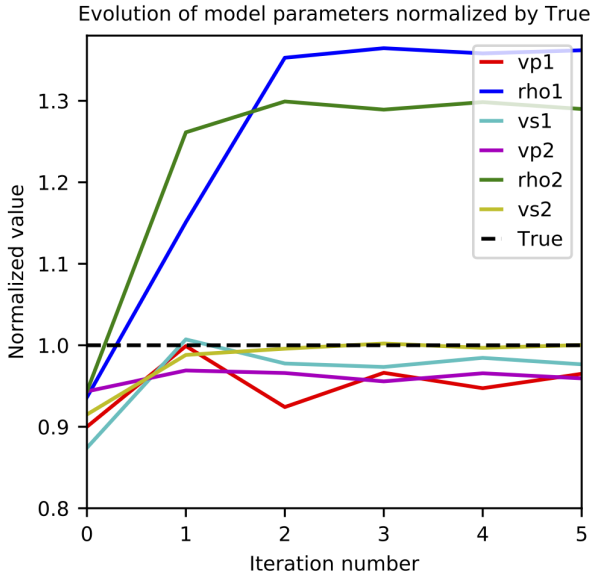

(a) Normalized model evolution

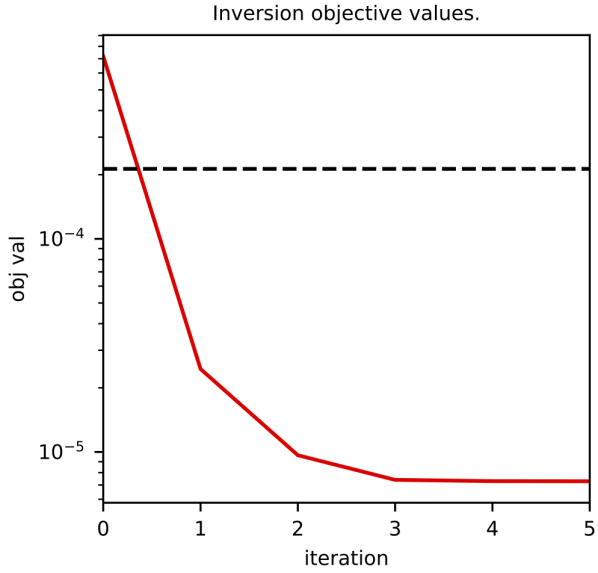

(b) Objective function

Figure 2.10: (a) Normalized model evolution during an inversion using only the amplitude of the chalk reflection. (b) Objective function from values derived with equation 2.6, using the amplitude as a constraint.

Amplitude and phase inversion

We now investigate whether the amplitude of the reflection event helps in the inversion when it is combined with the phase. We first evaluate the amplitude and phase.

Figures 2.11a and 2.11b show the evolution of phase and amplitude for some of the iterations for a shot located at $x = 2.5$ km. We see that the amplitude and phase curves move closer to the true value as the inversion progresses. We also see that the true (blue line: Full EL-True) and true local (magenta line: CDA-EL Local) curves for the amplitude and phase do not match perfectly; thus, again we do not expect to obtain a perfect recovery of the elastic parameters. The gray areas shown in Figures 2.11a and 2.11b are muted and are not used in the inversion.

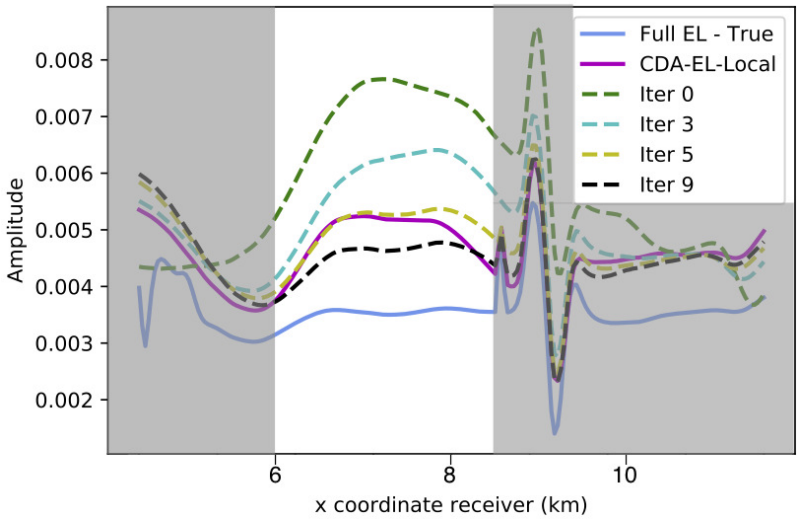

(a) Amplitude modeled

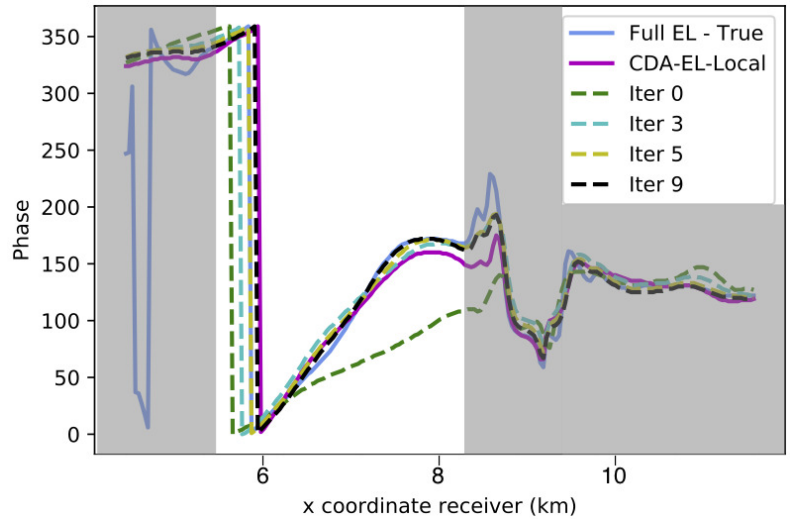

(b) Phase modeled

Figure 2.11: Amplitude (a) and phase (b) modeled for different iterations for a source at $x = 2.5$ km for an inversion using the amplitude and phase. The gray areas are muted and are not used in the inversion.

Figures 2.12a and 2.12b show the evolution of the model $\mathbf{m}_i$ as a function of iteration numbers for phase and phase and amplitude for three shots located at $x = 2.5$ km, 3.5 km, and 4.5 km. The curves are normalized using the true value, as done previously for the amplitude inversion. The curves show oscillatory updates; however, the range of variation decreases when the number of iterations increases in both cases. The chalk density exhibits the largest range in both graphs, but it is clear that the algorithm has converged by the last few iterations. Comparing both graphs at iteration number 10, we see that all of the elastic parameters converge to the true values.

Table 2.2 shows the true, initial, and inverted parameter values for the hydrocarbon anomaly and the chalk using phase as well as phase and amplitude. Both inversions are done with three shots and 10 iterations. The associated errors are less than 5% for the phase, and even lower for phase and amplitude, suggesting that the amplitude helps to improve the accuracy of the recovery.

Table 2.2: The P- and S-wave velocities and densities for the hydrocarbon anomaly and the bulk chalk. The parameters are inverted for phase only and then for the phase and amplitude together using three shots.

Hydrocarbon anomaly						
	True	Initial	Phase Inverted	Error	Phase & Ampl Inverted	Error
v_p(km/s)	5.00	4.30	4.77	4.54%	4.82	3.5%
v_s(km/s)	2.86	2.20	2.85	0.25%	2.86	0.24%
ρ(kg/km^3)	2.35	2.10	2.23	2.14%	2.31	1.78 %
Chalk layer						
	True	Initial	Phase Inverted	Error	Phase & Ampl Inverted	Error
v_p(km/s)	5.30	4.60	5.51	4.0%	5.49	3.7%
v_s(km/s)	3.06	2.60	3.04	0.45%	3.04	0.42%
ρ(kg/km^3)	2.65	2.30	2.71	2.54%	2.70	1.89%

2.4.2 Tradeoffs between data and reconstruction accuracy

In this section, we study the trade-off between the data as an input to the inversion and the accuracy of the inverted elastic parameters. We compare the phase and amplitude

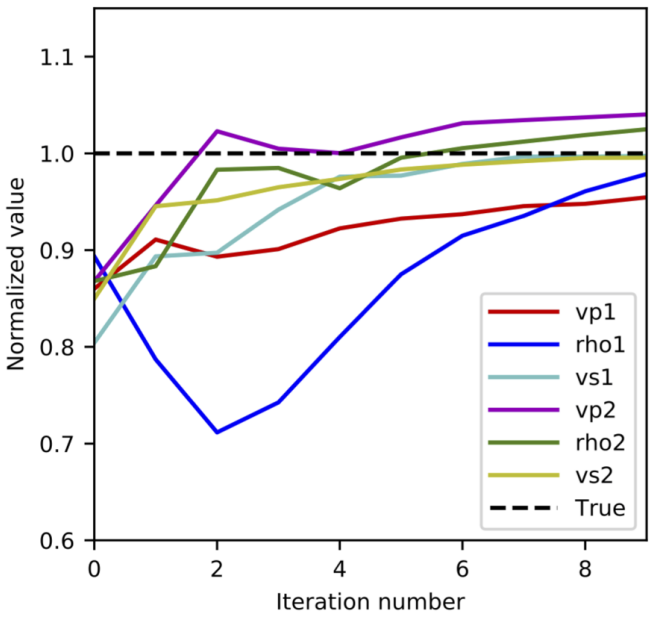

(a) Phase inversion

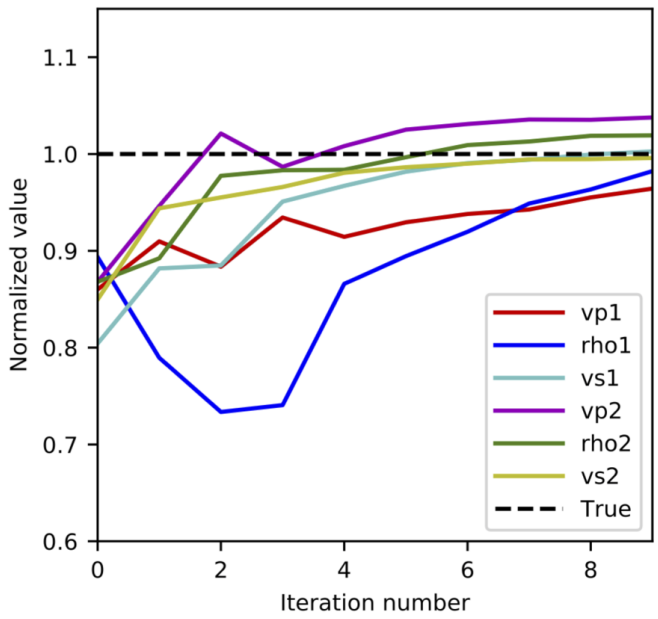

(b) Phase and amplitude inversion

Figure 2.12: Elastic parameters recovered using: (a) the phase and (b) phase and amplitude as constraints. We use three shots to invert for the elastic parameters.

inversion responses using three, four, five, and finally six shots in the inversion (Figure 2.13).

Comparing the four graphs shown in Figure 2.13, we see that the densities (ρ_1 and

ρ_2) improve when more data are used in the inversion, whereas the velocities decrease slightly in accuracy. For instance, S-wave velocities for the hydrocarbon anomaly and chalk layer decrease their accuracy by 0.6% and 0.11%, respectively, when six shots are used, whereas the densities increase their accuracy by 1.66% for the hydrocarbon anomaly and 0.64% for the chalk layer. In general, S-wave velocities (v_{s1} and v_{s2}) are already well-constrained with three shots, densities do well by the time we reach six shots, and v_{p1} and v_{p2} are still relatively poorly constrained even when using six shots.

Table 2.3: P-wave and S-wave velocities, and density for the hydrocarbon anomaly and the bulk chalk. We run the inversion with three and six shots, using the phase and amplitude simultaneously in the inversion.

Hydrocarbon anomaly						
	True	Initial	3shots.	Error	6shots	Error
v_p(km/s)	5.00	4.30	4.82	3.5 %	4.73	5.2%
v_s(km/s)	2.86	2.20	2.86	0.24%.	2.87	0.67%
ρ(kg/km^3)	2.35	2.10	2.30	1.78%	2.34	0.12%
Chalk layer						
	True	Initial	3shots.	Error	6shots	Error
v_p(km/s)	5.30	4.60	5.49	3.70%	5.54	4.62%
v_s(km/s)	3.06	2.60	3.04	0.42%	3.07.	0.53%
ρ(kg/km^3)	2.65	2.30	2.70	1.89%	2.68	1.25%

In Table 2.3 we see the inverted values and errors calculated for three and six shots. The most notable improvements are in the densities ρ_1 and ρ_2 when six shots are used. Even though v_{s1} and v_{s2} increase the percentage of error, both of these errors are still less than 1%. The worst results are for v_{p1} and v_{p2}, both of which increase their error by approximately 2% showing that additional data change the objective function, resulting in convergence to different local minima, highlighting the nonlinearity in the inverse problem [75, 54].

2.4.3 Tradeoff between elastic parameters and reconstruction accuracy

The nonlinearity present in elastic FWI is an important area of interest because the reconstruction of high-quality subsurface parameters from multicomponent seismic data is a great help in rock property identification and reservoir prediction [76, 15]. In this section we focus on the trade-off between the elastic parameters and reconstruction accuracy using the CDA-EL solver. To evaluate the accuracy in the reconstruction, we test four different configurations using three shots in the inversion: (v_{p1}, v_{p2}); (v_{s1}, v_{s2}); (ρ_1, ρ_2); and $(v_{p1}, v_{p2}, v_{s1}, v_{s2})$. During the inversions the parameters that are not calculated are fixed to their true values and all inversions are run to convergence, defined as when a new model cannot be found with a line search that reduces the objective function.

Table 2.4: P-wave and S-wave velocities, and density for the hydrocarbon anomaly subindex 1 and the chalk subindex 2 inverted with (v_{p1}, v_{p2}); (v_{s1}, v_{s2}); (ρ_1, ρ_2) and (v_{p1} v_{p2}, v_{s1}, v_{s2}); using three shots with phase and amplitude simultaneously.

	True	Initial	Inverted	Error
Configuration 1				
v_{p1}(km/s)	5.00	4.30	5.14	2.8%
v_{p2}(km/s)	5.30	4.60	4.52	14.6%
Configuration 2				
v_{s1}(km/s)	2.86	2.20	2.91	1.7%
v_{s2}(km/s)	3.06	2.60	3.08	0.7%
Configuration 3				
ρ_1(kg/km^3)	2.35	2.10	2.32	1.2%
ρ_2(kg/km^3)	2.65	2.30	2.65	0.2%
Configuration 4				
v_{p1}(km/s)	5.00	4.30	4.92	1.6 %
v_{p2}(km/s)	5.30	4.60	5.45	2.8%
v_{s1}(km/s)	2.86	2.20	2.90	1.5%
v_{s2}(km/s)	3.06	2.60	3.06	0.09%

These tests yield results similar to the test in the previous subsection in which we increased the number of shots. The P-wave velocities are the poorest resolved (Figure 2.14a), while S-wave velocities and densities are well-recovered (Figure 2.14b and

2.14c). From the P-wave curves we see that the algorithm favours large contrasts; that is v_{p1} and v_{p2} are over- and underestimated, respectively, producing a large contrast. We know that large contrasts can give complex reflection coefficients and thus phase rotation, producing errors in the phase (Figure 2.15a). These errors in the phase lead to large errors in the inverted P-wave velocities. Furthermore, most of the information in the inversion is provided by the phase because the phase ranges between 0° to 360°, while the amplitude ranges only from 0 to 0.010 maximum (Figure 2.15a and 2.15b). This suggests that we may need to weight the amplitude and phase data differently in the misfit term (equation 2.6) or to use a different functional for the misfit (instead of that given in equation 2.4); we will return to this in the discussion. When P- and S-wave velocities are inverted together, P-wave velocities recovered values become close to the true values (Figure 2.14d). In this case the modeled phase is much more accurate (Figure 2.15c). Thus, it is clear that including S-wave velocities in the inversion moves the objective function toward a local minimum that is closer to the global minimum. Table 2.4 shows the inverted values and errors for the four configurations studied.

2.4.4 Starting model - sensitivity study

In this section, we evaluate the sensitivity of the objective function considering 220 different initial models and analyze the objective function in the (v_p, v_s, ρ) parametrization. We calculate the models using the relationship:

$$m = m_{true} + \alpha m_1 + \beta m_2, \tag{2.12}$$

where $m_1 = (v_{p1}, v_{s1}, \rho_1, 0, 0, 0)$ and $m_2 = (0, 0, 0, v_{p2}, v_{s2}, \rho_2)$ and m_{true} is the true model.

Figure 2.16 shows contour maps for the objective function used in the inversion. The first evaluation of the objective function shows convergence toward the global minimum (i.e., $(\alpha, \beta) = (0, 0)$, Figure 2.16a). However, zooming on the vicinity of the global minimum, we find several local minima that are quite close together (Figure 2.16b). Looking at the details in Figure 2.16b we see that the global minimum is not at $(\alpha, \beta) = (0, 0)$, instead we see smaller values of the objective function around $(\alpha, \beta) = (0.14, 0.04)$, which means that, even if we successfully converge to the global

minimum of our objective function, we will not have converged to the true model. It is worth mentioning that because the observed data are created by full elastic modeling, whereas the predicted data are simulated by the simpler local elastic modeling, systematic errors due to the simplified physics only allow us to estimate approximate solutions. However, this method allows us to access an estimate of the parameters in a more computationally efficient way compared with full elastic solvers.

2.4.5 Discussion

Our goal in using the CDA-EL local solver is to evaluate the amplitudes modeled and investigate if those amplitudes can be used as constraints in the inversion to recover elastic material parameters. To evaluate the accuracy of the local reflections' amplitude, we use a simple two-layer model, in which we compare and verify that the amplitude of the local reflections is similar to the true elastic model and relatively accurate from approximately 25° to 48°, which is our region of interest. Using a more realistic and complex velocity model (the North Sea model), we invert for six elastic parameters. The evolution of the model as a function of iterations, using the phase and phase and amplitude in the inversion (Figure 2.12) shows that the amplitude helps in the convergence (Table 2.3). These results agree with previous results by [101]. They observe that the combination of amplitude and phase in the inversion produces slightly better results. However, our inversion converges much faster than their inversion, requiring only 10 iterations compared to 50 iterations required by [101] to obtain similar percentages of errors. In addition, in the inversion procedure, we estimate that using the CDA-EL local solver takes approximately 20% of the time that it would take to use a Full-EL solver or 47% of the time for an elastic to elastic solver, for 10 iterations, four parameters and three shots.

In comparing three to six shots in the inversion, we find that the P-wave velocities are relatively poorly constrained even with six shots, which suggests that additional data change the objective function, resulting in convergence to a different local minimum. The opposite occurs with densities, which improve their precision when more data are used in the inversion (Table 2.4). On the other hand, the analysis of the trade-off between elastic parameters shows that our algorithm favors large contrasts, producing errors in the phase that cause large errors in the recovered P-wave velocities. Most of the information in our inversion is given by the phase because it has

a larger range than the amplitude and thus intrinsically carries greater weight in our inversion setup. We attempt to normalize the amplitude and phase using several different approaches. For instance, we scale amplitude and phase data to have values between zero and one. In this case, it does not converge to the true value, rather the inversion does not progress or even diverges quite far from the true values. We normalize the phase only, and we obtain exactly the same inversion as the original, showing that the implementation is correct and the inversion is not affected by the scaling. Another strategy that we use is normalizing the objective function. We use the normalization proposed by [46]; nonetheless, this method does not result in a stable algorithm. There are many other ways one could imagine scaling the amplitude and phase, but it seems that allowing the phase to be a stronger contributor to the inversion is advantageous for a stable, accurate inversion algorithm.

When we invert v_p and v_s at the same time, the behaviour of v_p improves, showing clearly that v_s constrains the inversion to local minima that are closer to the global minimum. Indeed, we see that the S-wave velocity is the most stable parameter with the lowest percentage of error in all of the inversions. This may be because the inversion is helped by the chalk layer having a PS critical angle. Although we window around the reflected P-wave, we would expect some converted S energy to arrive at nearly the same time, meaning that this wave also contributes to the inversion. [6] observe similar results when inverting for v_p and v_s simultaneously.

In the last part of this study, we evaluate the sensitivity of the objective function. Inverting for multilayered and multidimensional models is difficult due to the relationship between the reflectivity of the interface at a given angle and the elastic properties of the media on both sides of the interface — in this case, the hydrocarbon anomaly and the chalk layer. We find that, despite the nonlinearity of our problem, the objective function converges to the global minimum. However, there are several local minima around the global minimum that easily trap the inversion away from the true model. In this study, we use the Gauss-Newton method that iteratively searches for a solution from a starting point in which a direction with a constant step length is computed at each iteration to determine the next point. Future work might focus on investigating the method that is used for computing the step length or use of the global linear approximation to compute the search direction [27].

In this paper we use the amplitude and phase of the PP-reflections in the inversion.

However, the CDA-EL local solver could be used for other elastic wave modes such as the P-S, S-S and S-P reflections.

2.5 Conclusions

In this paper, we model the amplitude of the reflection using a CDA-EL local solver on a simple two-layer model and on a more complex heterogeneous velocities model. Both amplitudes are modeled sufficiently accurately in our region of interest. The combination of the size of the local solver and taper as well as the position of the source play an important role in the behavior of the amplitude curves modeled and the resulting accuracy of the inversion. We observe that using a three-wavelength taper and a source located near the middle of the local domain allow us to model amplitudes with high accuracy. Having accurately recovered the amplitudes, we incorporate them as a constraint in the inversion and we show that, for an amplitude and phase inversion, we are able to recover more accurate model parameters of a reflector of interest compared to what we can obtain with the phase alone. Our results suggest that, if your objective is recovering accurate P-wave velocities, it is important to invert for v_p and v_s simultaneously. In addition, accurately modeling the data and including many shots in the inversion is more important in the recovery of density than the recovery of S- and P-wave velocities. Finally, we evaluate the sensitivity of the CDA-EL solver to the initial model, in which we find that we are able to recover parameters closer to the global minimum but with many local minima clustered around the global minimum resulting in a loss of accuracy in the recovered model. The next step will be to focus on using strategies that optimize and regularize the inversion algorithm.

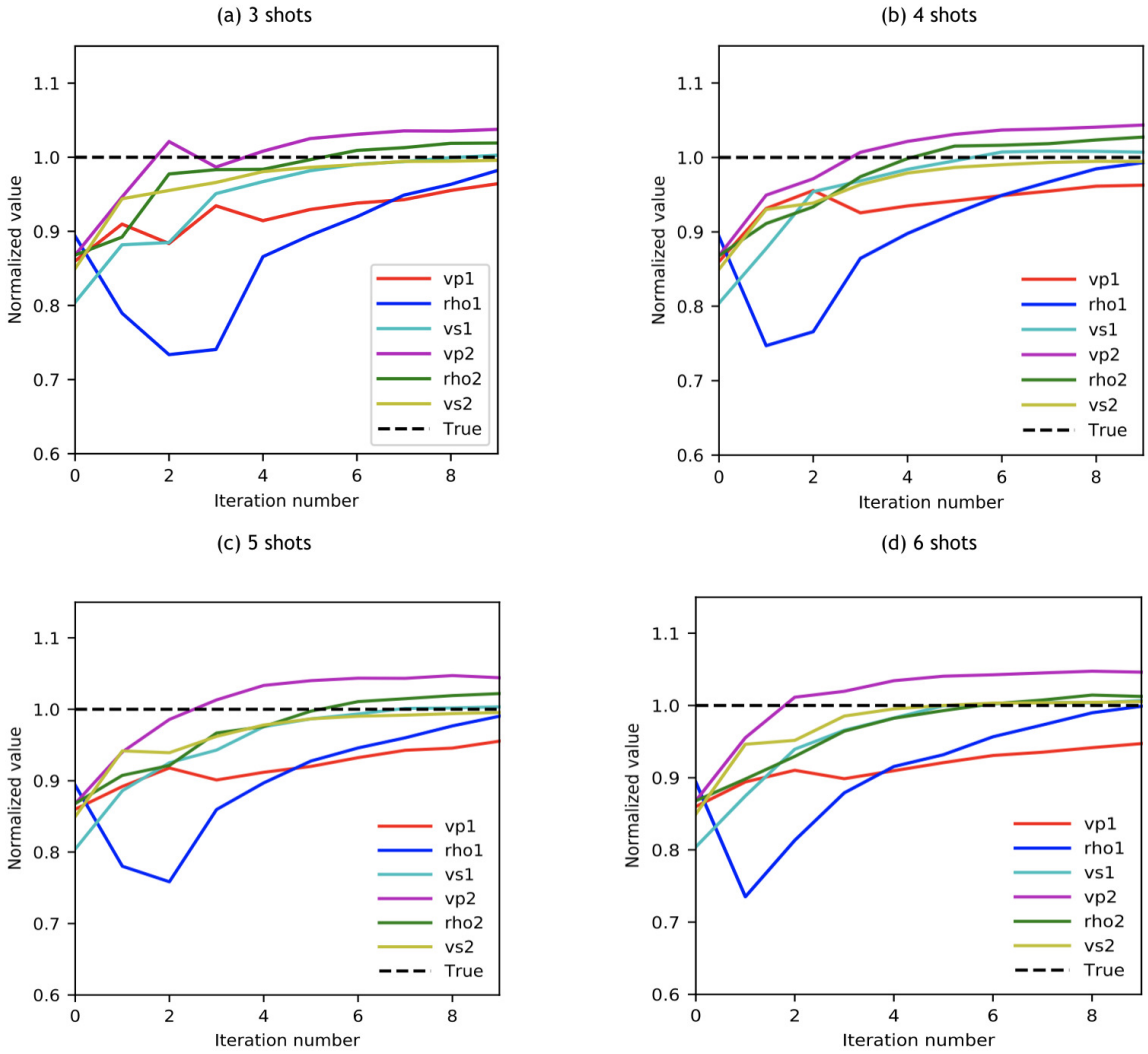

Figure 2.13: Phase and amplitude inversion. Elastic parameters recovered using phase and amplitude for: (a) three shots, (b) four shots, (c) five shots, and (d) six shots.

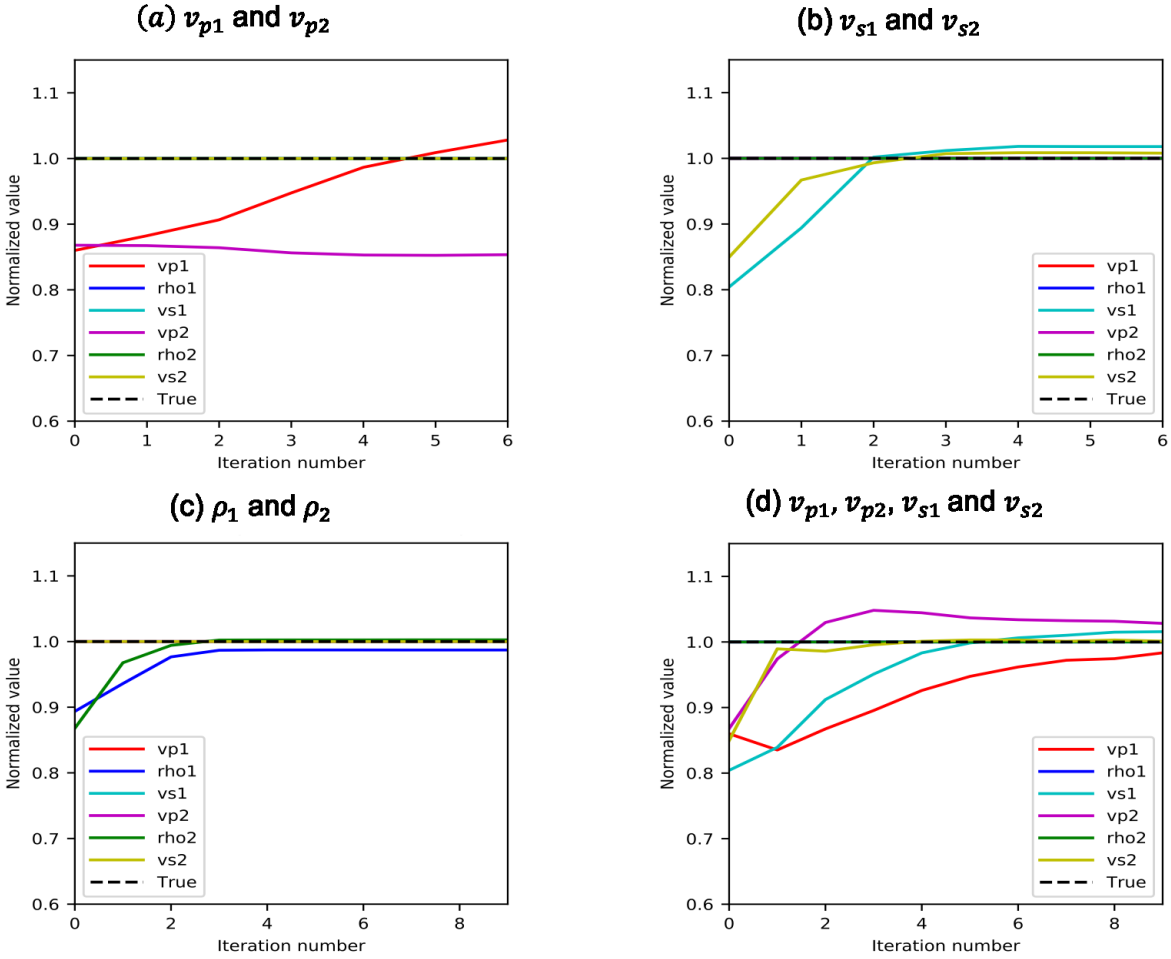

Figure 2.14: Phase and amplitude inversion. Evolution of the models as a function of iteration numbers for (a) v_{p1}, v_{p2}, (b) v_{s1}, v_{s2}, (c) ρ_1, ρ_2 and (d) $v_{p1}, v_{p2}, v_{s1}, v_{s2}$.

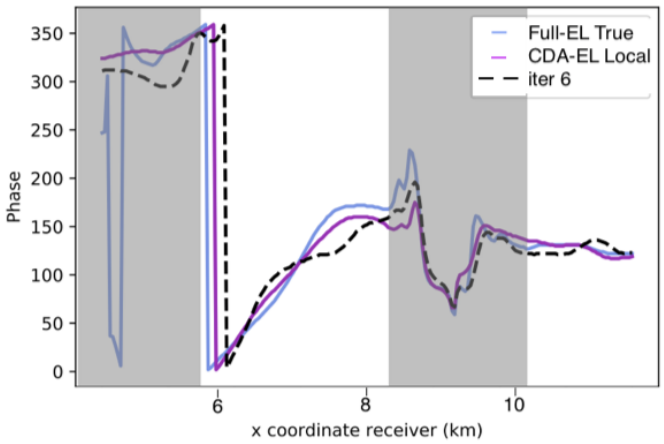

(a)

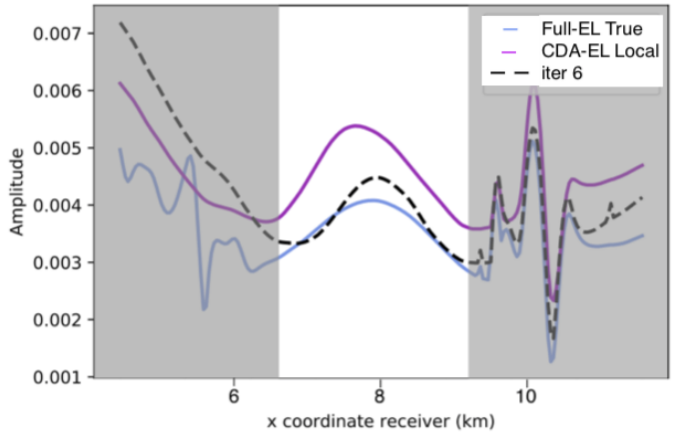

(b)

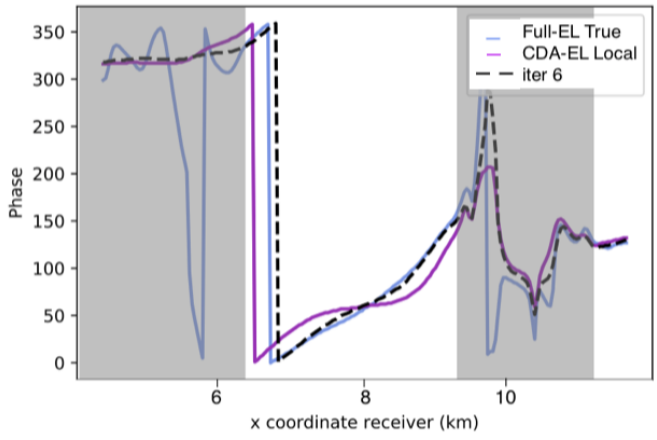

(c)

Figure 2.15: Phase (a) and amplitude (b) modeled for a shot at 2.5 km in iteration number 6 of the inversion of P-waves velocities only (v_{p1} and v_{p2}) (black dash line: iter 6). (c) Phase modeled for a shot at 3.5 km at iteration number 9 of the inversion of P-waves velocities only (v_{p1} and v_{p2}) (black dash lines) and using the full EL domain (blue line: Full EL -True), true local curve (magenta line: CDA-EL Local). The gray areas are muted and are not used in the inversion.

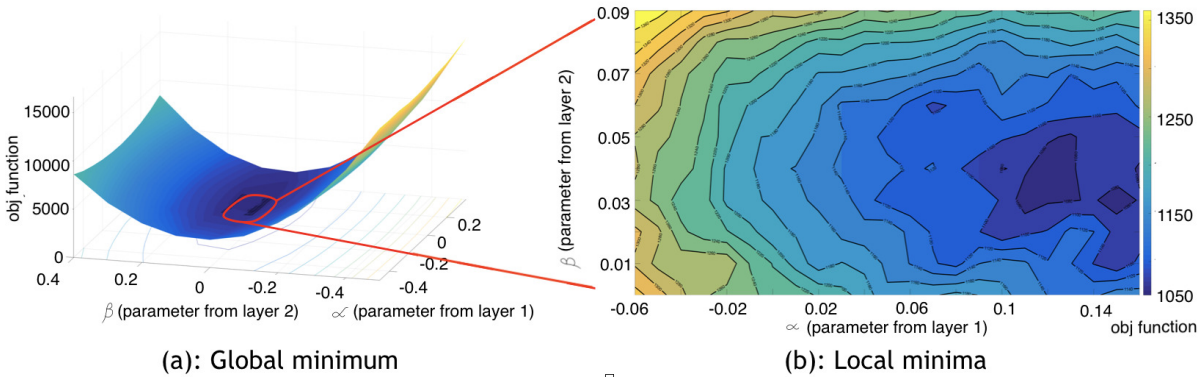

Figure 2.16: Contour map for the objective function showing (a) global minimum and (b) local minima.

Chapter 3

Reduced memory implementation of a local elastic finite-difference solver

3.1 Summary

The recovery of elastic properties from seismic data often requires the iterative use of seismic modeling. Finite-difference (FD) simulation is a common component in seismic modeling, and it is usually the most computationally expensive step in methodologies such as inversion or reverse time migration. Local solvers attempt to reduce the cost of FD simulations by reducing the computational domain to small areas, updating the model within these areas without recomputing throughout the full domain. We have implemented a local elastic solver that allows us to propagate the elastic wavefield within a subvolume after local alterations of the model. We determine how the scattered wavefield due to the alterations can be extrapolated from the local domain to surface receivers. We extend existing works by using the method of multiple point sources to recompute the wavefield within the local domain. This method is memory efficient because it only requires the global wavefield to be recorded along the local domain boundary. By injecting these recordings as point sources, the global wavefield is emulated within the local domain. Thus, the method requires no modifications of standard FD solvers, merely the ability to record and inject data. We evaluate the capability of the local elastic solver to reconstruct the wavefield in a subvolume of the

elastic SEAM model.

3.2 Introduction

The finite-difference (FD) method is commonly used to model and reconstruct wavefields. Applications of wavefield modeling include tomographic imaging [50], full waveform inversion (FWI) [75] and reverse time migration (RTM) [5]. Modeling is the most computationally intensive component in seismic imaging and inversion schemes. Local solvers have been developed and implemented to reduce the cost of FD simulations [61, 78, 87]. These algorithms reduce the size of the computational domain to small areas, allowing this part of the model to be updated without recalculating the wavefield throughout the full domain.

Local solvers are divided into two categories. In the first type of solver, boundary conditions are used to immerse the local domain in an extended domain. [29] present the general idea of this boundary condition. They use an analytic boundary condition to connect an inner and outer domain, and they solve the wave equation with a different method in each domain. In the other type of local solver, wave propagation is first performed in the background model and then used as an input to obtain the wavefield inside the local area. In this case, the wavefield is injected as a set of monopole and dipole sources [4, 61, 8]. [61], for example, present the FD-injection method to efficiently inject wavefields in a local domain after model alterations. They apply the method in a 2D time-lapse seismic problem showing a reduction in computation cost of 85%. In this study, we will also implement the local solver using a source-injection technique. This wavefield injection method is known as the method of multiple point sources (MPS) [53].

[50] develop a generalized approach to construct the excitation sources for time-reversal mirrors (TRMs) by introducing a spatial window function into the wave equation. They argue that the concept of TRMs can be used for forward and back propagation of the field in the local domain. They show that, when implementing a TRM with the FD method, their method is equivalent to the FD injection, as described by [61]. However, FD injection is a memory-intensive algorithm, requiring storage of FD quantities of up to twice the size of the FD stencil. A more memory-efficient method is the MPS methodology such as, for example, the methods explained in [51]

and [79]. These methods only require the storage of FD quantities along a single surface in the FD grid. For example [79] discuss the implementation of the MPS method in a standard staggered FD algorithm for the acoustic wave equation and its application to RTM. Hence, the MPS method provides a memory-efficient way to reconstruct FD wavefields within a local domain.

As a transition from acoustic to elastic, [87] propose coupling a local elastic solver with a background acoustic solver to estimate phase variation with angle. They use an acoustic solver to propagate the wavefield to a local domain in which the local elastic solver from [61] is implemented. [38] present an extension to the work of [87] using the coupled acoustic-elastic local solver to estimate amplitudes, which are then used to constrain an elastic inverse problem.

This study shows how to implement the MPS method in a staggered-grid FD scheme for the isotropic elastic wave equation and how to extrapolate the scattered wavefields from the local domain to the receiver locations. An attractive feature of our method is that no modifications of computer code are strictly required as long as data can be recorded and injected into an FD simulation. Thus, this local solver implementation approach requires minimal memory and minimal changes to the code of FD solvers, which is appealing for solving 3D problems. We implement the method in an existing FD solver, turning it into a local solver. Then, we use the modeled wavefield to estimate the phase and amplitude of a reflection event of interest. Here, we build upon Devito [48], implementing the MPS method within the framework of this code. Our goal is to provide the means for easy development and design of local elastic solvers algorithms to a broad range of researchers.

This paper is structured as follows. In the "Theory" section, we explain how to implement the elastic MPS methodology to reconstruct the wavefield inside an injection boundary. We use a simple model to verify the implementation. In the second part of this section, we introduce the extrapolation of the scattered wavefield to the receiver positions. We then show a two-layer model to explain the extrapolation of the scattered wavefield. Then, we validate the injection and extrapolation methods by comparing them with a full-domain elastic solver, recovering the amplitude and phase within a window that contains a reflection of interest. Finally, we demonstrate the method on a more complicated model.

3.3 Methods

In this section, we first describe the underlying theory of the local solver. We use methods developed by [17, 2] and [86], which we summarize and expand with additional implementation details. In the last part of this section, we give an explicit workflow describing what quantities need to be recorded and how to use them in each calculation step.

3.3.1 Wavefield injection using MPS

We consider elastic wave propagation in an isotropic heterogeneous medium. To solve the elastic wave equation, we use the velocity-stress formulation proposed by [83]:

$$\begin{aligned}
\frac{\partial v_x}{\partial t} =& \frac{1}{\rho}\left(\frac{\partial \tau_{xx}}{\partial x} + \frac{\partial \tau_{xz}}{\partial z}\right) + f_x(\mathbf{x_s}, t) \\
\frac{\partial v_z}{\partial t} =& \frac{1}{\rho}\left(\frac{\partial \tau_{xz}}{\partial x} + \frac{\partial \tau_{zz}}{\partial z}\right) + f_z(\mathbf{x_s}, t) \\
\frac{\partial \tau_{xx}}{\partial t} =& (\lambda + 2\mu)\frac{\partial v_x}{\partial x} + \lambda\frac{\partial v_z}{\partial z} + h_{xx}(\mathbf{x_s}, t) \\
\frac{\partial \tau_{zz}}{\partial t} =& (\lambda + 2\mu)\frac{\partial v_z}{\partial z} + \lambda\frac{\partial v_x}{\partial x} + h_{zz}(\mathbf{x_s}, t) \\
\frac{\partial \tau_{xz}}{\partial t} =& \mu\left(\frac{\partial v_x}{\partial z} + \frac{\partial v_z}{\partial x}\right) + h_{xz}(\mathbf{x_s}, t),
\end{aligned} \tag{3.1}$$

where ρ is the density; λ and μ are the Lamé parameters; v_x and v_z are the horizontal and vertical particle velocities, respectively; and τ_{xx}, τ_{xz} and τ_{zz} are the normal and shear stresses. Using the elastic representation theorem, we can determine the displacement wavefield $u_i(\mathbf{x}, t)$ within a volume V from measurements of displacement $u_i(\mathbf{x}', t)$ and normal tractions $\tau_{ij}(\mathbf{x}', t)n_j$ on an enclosing surface S (Figure 3.1) [17, 2] by

$$\begin{aligned}
u_n(\mathbf{x}, t) = \oint_S G_{in}(\mathbf{x}, \mathbf{x}', t) * \tau_{ij}(\mathbf{x}', t)n_j dS' - \\
\oint_S u_i(\mathbf{x},' t) * C_{ijkl}\partial_l G_{kn}(\mathbf{x}, \mathbf{x}', t)n_j dS',
\end{aligned} \tag{3.2}$$

where $G_{in}(\mathbf{x}, \mathbf{x}', t)$ is the component of the displacement Green's tensor at location $\mathbf{x}$ in direction n due to a unit point force at $\mathbf{x}'$ in direction i. Note that the Green's

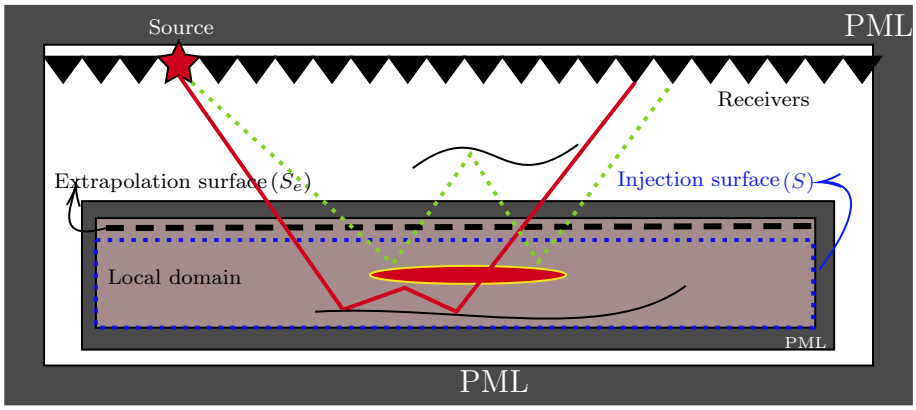

Figure 3.1: Schematic of the local solver. The dark-gray layers represent the perfectly matched layers (PMLs) on the boundary. The model is perturbed and the scattered field is updated within the local domain (the light red-gray region). The injection occurs on the injection surface S (the blue dotted line), and the extrapolation to the receiver locations takes place from the extrapolation surface S_e (the black dashed line). The local solver discards scattered wavefields that exit and then reenter to the local domain such as the green dashed line. Internal multiples with all three reflection points within the local domain are included.

functions can be computed in any model including all of the heterogeneities; here, we will compute them with finite differences. The variable $u_n(\mathbf{x}, t)$ is the nth component of the displacement vector, $*$ denotes temporal convolution, $\tau_{ij}(\mathbf{x}', t)n_j$ is the normal traction on the surface S, C_{ijkl} is the fourth-rank stiffness tensor and ∂_l represents the derivative with respect to the x_l coordinate.

The representation integral, equation 3.2, as stated is an integral that is not straightforward to solve. However, it may conveniently be computed on the fly with an FD scheme, using point-source excitations as shown by [51]. In the context of the velocity-stress system (equation 3.1), these sources take the following form:

$$
\begin{aligned}
f_x(\mathbf{x}_s,t) &= \sum_{s=1}^{N_s} \frac{1}{\rho}[\tau_{xx}n_x + \tau_{xz}n_z]\delta_s \\
f_z(\mathbf{x}_s,t) &= \sum_{s=1}^{N_s} \frac{1}{\rho}[\tau_{xz}n_x + \tau_{zz}n_z]\delta_s \\
h_{xx}(\mathbf{x}_s,t) &= \sum_{s=1}^{N_s} [(\lambda+2\mu)v_x n_x + \lambda v_z n_z]\delta_s \\
h_{zz}(\mathbf{x}_s,t) &= \sum_{s=1}^{N_s} [\lambda v_x n_x + (\lambda+2\mu)v_z n_z]\delta_s \\
h_{xz}(\mathbf{x}_s,t) &= \sum_{s=1}^{N_s} \mu[v_x n_z + v_z n_x]\delta_s,
\end{aligned}
\tag{3.3}
$$

where $f_x(\mathbf{x}_s,t)$ and $f_z(\mathbf{x}_s,t)$ represent the point sources injected into the first two equations of equation 3.1, and $h_{xx}(\mathbf{x}_s,t)$, $h_{zz}(\mathbf{x}_s,t)$ and $h_{xz}(\mathbf{x}_s,t)$ are the point sources injected at the correspondent τ_{xx}, τ_{zz} and τ_{xz} partial stresses derivatives in equation 3.1. Note that all quantities on the right side of the equation 3.3 are recorded at x_s, as we suppress this explicit dependence. The variable δ_s denotes the delta-function centered at $\mathbf{x}_s \in S$ scaled by the discretization interval to ensure correct amplitude, and N_s represents the number of sources, which we choose equal to the number of grid points on S.

Figure 3.2 shows the boundary S intersecting the staggered grid. In this figure, τ_{xx} and τ_{zz} are recorded exactly on S (circles). However, due to the staggered grid configuration, v_x ,v_z and τ_{xz} are recorded on nodes offset from the boundary S. To calculate their values on S, we use bilinear interpolation from the nodes surrounding the desired location. The number of nodes used in the interpolation depends on the length of the FD stencil and is chosen to match the accuracy of the FD scheme. To clarify, the recording of the stresses τ_{xx} and τ_{zz} takes place at one node only (circular), whereas the recording of the velocities v_x, v_z and stress τ_{xz} takes place at multiple nodes (triangles and squares) where the number of nodes corresponds to the length of the FD stencil on S. Using these recorded wavefields on S we are able to compute the point sources described in equation 3.3.

Now we place the point-sources shown in equation 3.3 in the location where the

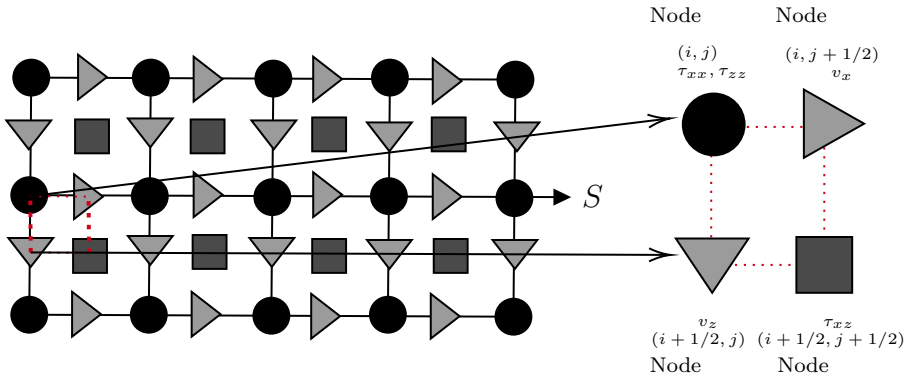

Figure 3.2: Grid for the staggered FD scheme. The zoom shows the locations of the wavefield components in the staggered elastic FD grid.

wavefields were recorded (i.e. at the circular nodes along S) to inject them inside the local domain. In this way, the injection of $h_{xx}(\mathbf{x}_s, t)$ and $h_{zz}(\mathbf{x}_s, t)$ takes place at circular nodes, whereas $f_x(\mathbf{x}_s, t)$, $f_z(\mathbf{x}_s, t)$ and $h_{xz}(\mathbf{x}_s, t)$ are extrapolated from the recording locations (circular nodes) onto the staggered FD grid, at the triangular and square nodes, respectively. Notice that equation 3.3 is general so that it can be used for arbitrary spatial-order stencils. We give more detail on how to record and inject the wavefields using the Devito package in the next section.

3.3.2 Injection using the Devito package

In this study we implement the local solver in the Devito package. This package is a domain-specific language for implementing the FD method [47].

To reconstruct the wavefield inside an injection boundary S for a source anywhere in the model, we need to save five different wavefields: v_x ,v_z, τ_{xz}, τ_{xx} and τ_{zz} on the boundary S (Figure 3.1). Then, we use these wavefields to compute the necessary point-sources given in equation 3.3. For instance, at the top portion of S where

$n = [0, -1]$, we inject

$$
\begin{aligned}
f_x(\mathbf{x}_s, t) &= \sum_{s=1}^{N_s} \frac{1}{\rho}[-\tau_{xz}]\delta_s, \\
f_z(\mathbf{x}_s, t) &= \sum_{s=1}^{N_s} \frac{1}{\rho}[-\tau_{zz}]\delta_s, \\
h_{xx}(\mathbf{x}_s, t) &= \sum_{s=1}^{N_s} \lambda[-v_z]\delta_s, \\
h_{zz}(\mathbf{x}_s, t) &= \sum_{s=1}^{N_s} (\lambda + 2\mu)[-v_z]\delta_s, \\
h_{xz}(\mathbf{x}_s, t) &= \sum_{s=1}^{N_s} \mu[-v_x]\delta_s,
\end{aligned}
\tag{3.4}
$$

where the fields v_x ,v_z, τ_{xz}, τ_{xx} and τ_{zz} are recorded on the boundary S. The sources on the other three portions of S are computed similarly. For demonstration purposes, we use a fourth-order FD scheme to model the response for a source located at $x = 2.5$ km and $z = 0.1$ km in a homogeneous elastic velocity model $v_p = 2.0$ km/s, $\rho = 2.0$ kg/m^3 and $v_s = 0.88$ km/s.

Figures 3.3(a) and 3.3(b) show the particle velocity v_z at time t=0.91 s modeled in the full domain and with the wavefield injection method, respectively. Figure 3.4 compares traces at $x = 2.0$ km and $z = 1.6$ km of the full and local v_x fields. There is a slight difference between the two curves. We measure the error by taking the L1-norm of the difference between the two traces to estimate the error in the reconstruction as 0.00046 m/s. This small difference depends on the FD stencil and the interpolation used during the injection, so that the method has a trade-off in the spatial sampling and the spatial order of the FD scheme. We tested our implementation with 2nd- to 8th-order schemes and with different sampling and the error decreases as we move toward smaller sampling and a lower space-order scheme. However, using reduced spatial sampling and a lower spatial-order scheme also requires a denser grid, increasing the computational cost.

To this point, we have implemented the MPS method to reconstruct wavefields inside the local domain using wavefields recorded along S. If the model inside of the local domain undergoes alterations, then scattered fields are generated from the model

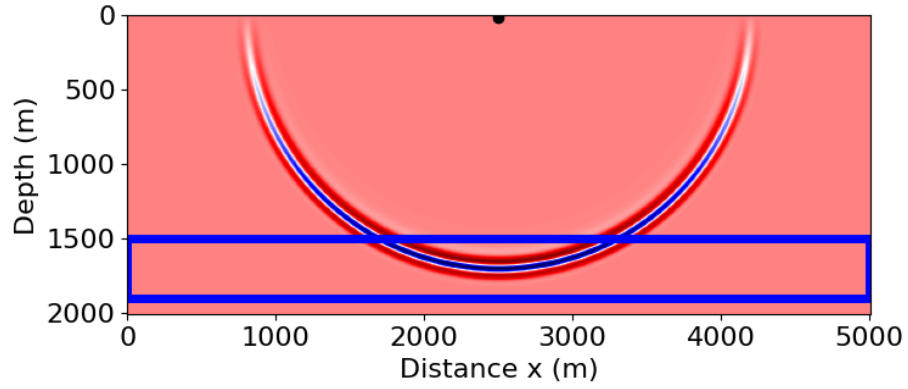

(a): Full

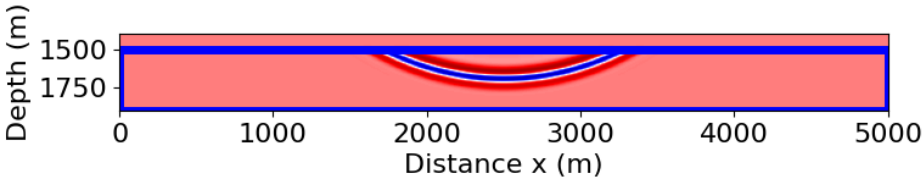

(b): Local

Figure 3.3: Snapshots of v_z at time t=0.91 s for an impulsive source at $x = 2500$ m in a constant velocity elastic model. (a): computed in the full domain, (b): computed by the injection of the monopole point sources. The blue box represents the injection surface (S) in Figure 3.1.

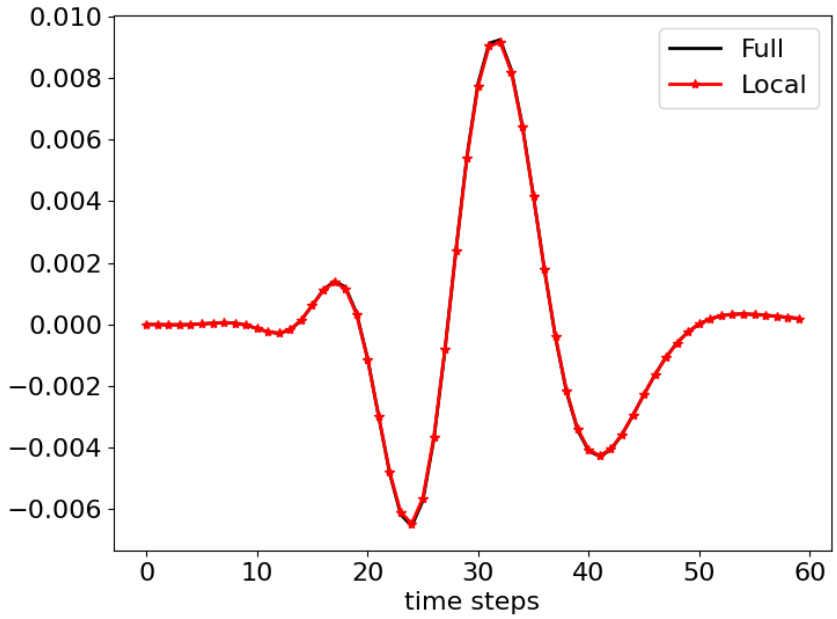

Figure 3.4: Trace comparison between full (solid) and local (triangle line) finite difference responses. Notice the excellent agreement between traces. The traces are located at $x = 2.0$ km and $z = 1.6$ km from the full and local modeled v_x fields.

perturbation in the local domain. This scattered field needs to be extrapolated from within the local domain to the receiver locations, which is the subject of the next subsection.

3.3.3 Extrapolation to the receiver positions

After the reconstruction of the wavefield inside the local domain in an altered model, the scattered wavefield should be extrapolated to receiver locations to be compared with the observed data. We use Green's functions between the receivers at the top of the model in Figure 3.1 and the extrapolation surface S_e (black dashed line in Figure 3.1), to extrapolate the scattered wavefield through the overburden via:

$$v_i^{rec} = v_i^b + \int_{S_e} (G_{ik}^v * \tau_{kj}^{sc} - G_{ijk}^\tau * v_k^{sc}) n_j dS, \tag{3.5}$$

where v_i^b is the ith component of the particle velocity in the background model, G_{ik}^v and G_{ijk}^τ are the Green's functions from the observation point (receiver locations) to

the point of integration on the surface (S_e), calculated in the unaltered model. The subscripts in G_{ijk} denote the stress in direction (j,k) due to a point force in direction i. The star denotes convolution in time, and n_j is the jth component of the normal to the surface S_e.

3.3.4 Computation of the Green's functions

Computing the Green's functions using the FD method and the reciprocity theorem involves the injection of impulsive sources at the receiver positions and recording the field at S_e. For example, to obtain v_x^{rec}, we compute

$$\begin{aligned} v_x^{rec} = v_x^b &+ \int_{S_e} (G_{xx}^v * \tau_{xz}^{sc} - G_{xxz}^\tau * v_x^{sc}) n_z dS \\ &+ \int_{Se} (G_{xz}^v * \tau_{zz}^{sc} - G_{xzz}^\tau * v_z^{sc}) n_z dS, \end{aligned} \tag{3.6}$$

where v_x^b is the x-component of the particle velocity for the background wavefield, i.e. the x-component of the velocity between the source and receiver in the unaltered model. The terms v_x^{sc}, v_z^{sc}, τ_{xz}^{sc}, and τ_{zz}^{sc} are the components of the scattered wavefield on S_e, and G_{xx}^v, G_{xxz}^τ, G_{xz}^v and G_{xzz}^τ are velocity and stress Green's functions due to an impulsive source injected in the x-direction (see also the description of the indices after equation 3.5). In other words, we need to inject an impulsive source in the x-direction as $f_x(x_r,t)$. To solve for v_z^{rec} a similar system of equations is obtained; but in this case the impulsive source $f_z(x_r,t)$ is injected. Each source needs to be run independently to obtain the corresponding Green functions making the calculation of these Green functions computationally and memory intensive.

Workflow

In this section, we take the theory derived above and describe each step in the computation explicitly. The objective of the local solver is to recompute the response of the forward wave propagation after perturbing the model inside the local domain within the injection area (the blue box in Figure 3.1) and then extrapolate the scattered wavefields from the extrapolation surface (Se) to the receiver positions. With this formulation, updating the shot gather after alterations to the model within the

local domain only requires us to recompute the part of the wavefield within the local domain. A workflow for the injection and extrapolation is presented in Figure 3.5.

We begin by defining the full elastic model parameters v_p, v_s and ρ. Then, we perform a forward model simulation for a source located at the top of the model (Figure 3.1). We use the library provided by the Devito package to perform the forward simulation. During the forward simulation, particle velocities and stresses v_i, τ_{jk} are recorded along S and S_e. The wavefield is also recorded at the receiver positions (triangles in Figure 3.1). We record the five wavefield components at only one type of node within the staggered grid (τ_{xx}, τ_{zz}, circle node Figure 3.2). We interpolate from the surrounding nodes to obtain v_x, v_z and stress τ_{xz}, which are computed at staggered locations. Devito provides the bilinear interpolation, and the number of grid points used depends on the length of the FD stencil.

After the full domain simulation, we perturb the model within the local domain inside S (blue box Figure 3.1). We then perform a simulation in the local domain to compute the scattered wavefield response from the alterations in the model. The model only differs from the original model inside S. The point sources calculated from the wavefields recorded in the first simulation are injected into the local domain along the surface S (see equation 3.3). If the model inside S does not have alterations, we expect the scattered wavefield to be zero. Notice that the multiple point sources generate the incoming wavefields and cancel the outgoing waves in this scenario, giving a scattered wavefield equal to zero. When we perturb the model inside S, a part of the wavefield will propagate outside the injection surface S. This scattered wavefield corresponds to the difference between the wavefields from the unaltered and the perturbed model. Only the parts of the wavefield that correspond to the perturbation will propagate outside of the injection surface S. Then, we record the scattered wavefields on S_e.

Once we have the scattered wavefield on the extrapolation surface, the propagation of the scattered wavefields recorded on S_e to the receiver locations can be performed at a significantly reduced computational cost. We use the FD method and the reciprocity theorem to compute the Green's functions on S_e, as explained above, and then we extrapolate the scattered wavefields using equation 3.5. Notice that the Green's function calculation is only performed once because there are no alterations in the model outside the surface S.

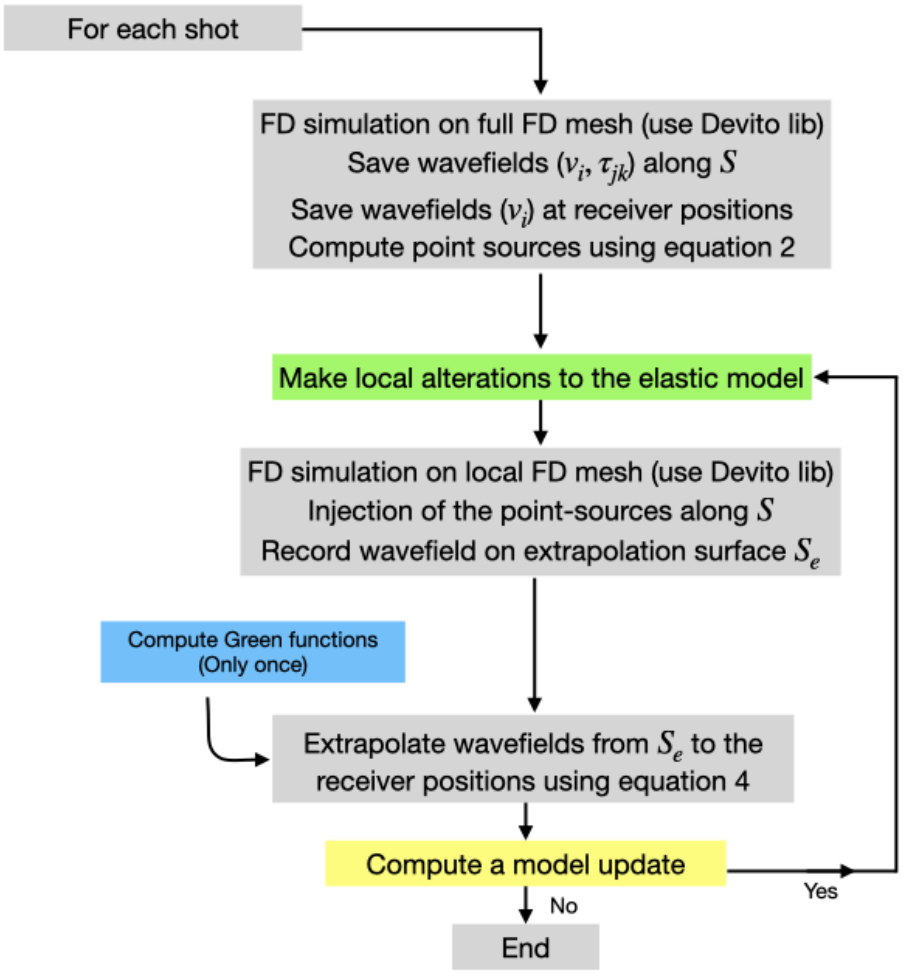

Figure 3.5: Workflow showing the MPS methodology and extrapolation in the Devito package.

Note that implementation of this method significantly reduces the computational cost in cases in which many iterative simulations are required, such as inverse problems. Performing this implementation for a single model alteration may not provide a computational benefit. We are not pursuing an iterative strategy in this paper because we are focused on the mechanics of the local solver, so we highlight only the appearance of a single iteration.

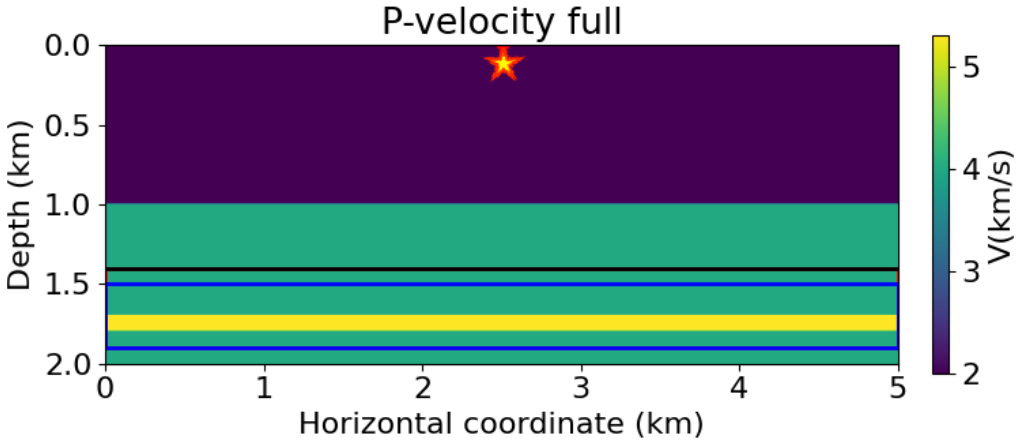

Figure 3.6: P-wave velocity of the two layer true elastic model. Material properties in the top layer are $v_p = 2000$ km/s, $\rho = 2.0$ kg/m^3, and $v_s = 0.88$ km/s. In the bottom layer, the material properties are 4.0 km/s, 2300 kg/m^3 and 1.54 km/s, respectively. The model contains a thin layer (yellow) with parameters 5.3 km/s, 2350 kg/m^3 and 2.86 km/s within the second layer. The blue box indicates the injection surface S and the black line represents the extrapolation surface S_e.

3.4 Numerical Examples

To verify the elastic local solver, we create a two-layer velocity model. We then verify the accuracy of the phase and amplitude of the reflection of interest by comparing them to the phase and amplitude computed in the full elastic model.

The P-wave velocity of the true elastic model is shown in Figure 3.6. The dimensions are 5.0 km $\times$ 2.0 km and the grid spacing is 10 m $\times$ 10 m. The source is located at $x = 2.5$ km and $z = 0.1$ km. The receivers are located along with the entire horizontal extent of the model at a depth of $z = 0.1$ km, the blue box in the P-wave velocity model corresponds to the injection surface S and the black line above the blue box marks the extrapolation surface S_e in Figure 3.6. For the source, we use a Ricker wavelet that generates only a P-wave with a peak of frequency 15 Hz. The entire model is surrounded by a PML boundary of 200 grid points as is the local domain (see Figure 3.1). We now investigate if we can correctly model the elastic PP-reflection using the local solver.

Figure 3.7 shows the shot gather for both the v_x- and v_z-components using the full-domain elastic solver (Figures 3.7a and 3.7b) and local solver (Figures 3.7c and 3.7d) for the model shown in Figure 3.6. In these figures, we see the direct wave, the

PP- and PS-reflection from the first reflector located at 1.0 km (Figure 3.6) (marked PP Ref1 and PS Ref1, respectively) and PP-reflection from the second reflector located at 1.7 km (Figure 3.6) (marked PP Ref2). Note that all waves are present in both components. Both plots are shown with the same colour scheme. Note that all wavefields have a time shift of approximately 70 ms because the Ricker wavelet peak is shifted away from $t = 0$ by about 70 ms.

Figure 3.8 shows a trace at $x = 2.0$ km of the PP Ref2 and PS Ref1 v_x-component shot gather. The black line in this plot is the trace computed in the full-domain (Figure 3.7a), and the red triangle dashed line is the trace computed using the local domain simulation (Figure 3.7c). Notice that in approximating the scattered wavefields generated by the local solver, the wavefield components that scatter on the perturbation and then leave and subsequently re-enter the local domain before going to the receiver locations are discarded (see Figure 3.1 green-dash line) and the internal multiples within the local domain are included (see Figure 3.1 red line). Thus, the local solver correctly computes the scattered wavefield from the injection, allowing us to update the wavefield after altering the elastic model within the local domain. The black and red curves in Figure 3.8 overlay one another exactly as expected. With this example we demonstrate that the local solver is correctly implemented for this geometry.

To verify the precision of the injection and the extrapolation methods implemented, we measure the phase and amplitude of the PP Ref2 v_x-component in the full simulation (Figure 3.7a), and the local simulation (Figure 3.7c) within a 0.2 s time window shown in Figure 3.7c with the red dashed lines.

Amplitude measurement

To recover the amplitude of the windowed reflection, we isolate the event and pick the amplitude independent of the phase. We use $\Upsilon_{amp} = \text{Max}(|\text{Hilbert}(\text{trace})|)$, where Υ_{amp} represents the amplitude obtained, $|.|$ is the absolute value and *trace* is the windowed trace (see [38]).

Figure 3.9 shows the amplitudes of the PP Ref2 v_x-component at the windowed reflection (Figure 3.7 the red dash lines). The black line and red triangle dashed line plot the amplitude of the full and local domain simulations, respectively (Figure 3.7a

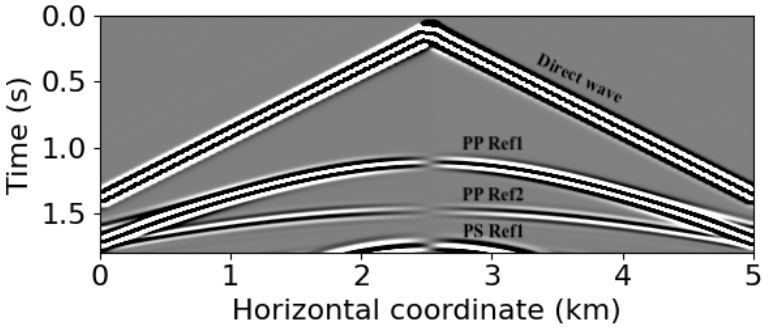

(a): v_x-component full

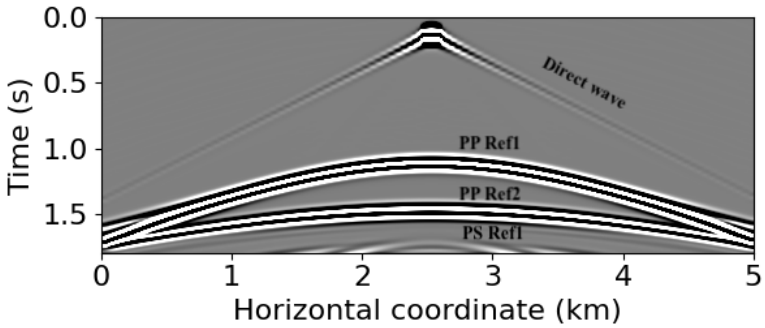

(b): v_z-component full

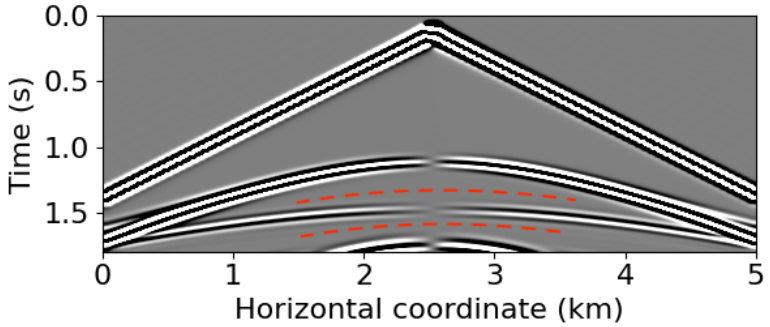

(c): v_x-component local

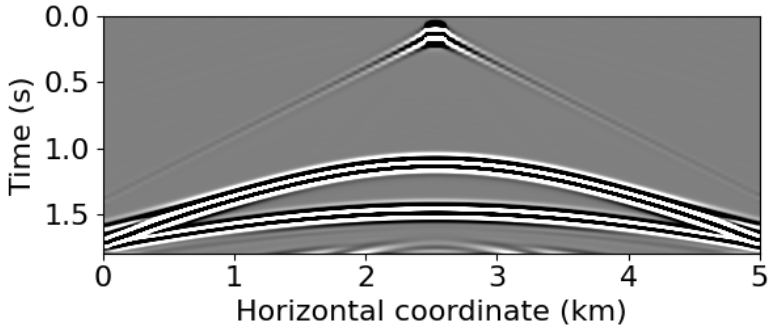

(d): v_z-component local

Figure 3.7: (a) and (c) shot gathers v_x-component and (b) and (d) shot gathers v_z-component for a source at $x = 2.5$ km. The same amplitude clipping is applied to both simulations so that the colour scales correspond. The red dashed lines indicate the window used to measure the amplitude of the PP- reflection of v_x-component shot gather.

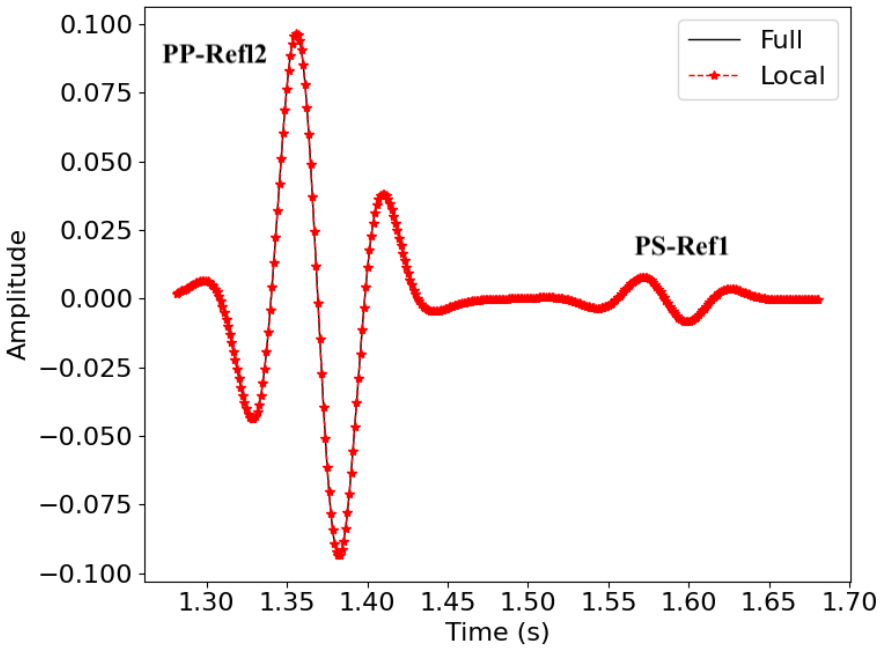

Figure 3.8: Traces at $x = 2.0$ km for a shot at $x = 2.5$ km from the v_x-component shot gather in Figure 3.7a. The black line shows the trace modeled with the full solver (Figure 3.7a) and the triangle dashed red line plots the trace modeled using the local solver (Figure 3.7c). Notice the excellent agreement between the full and local simulations.

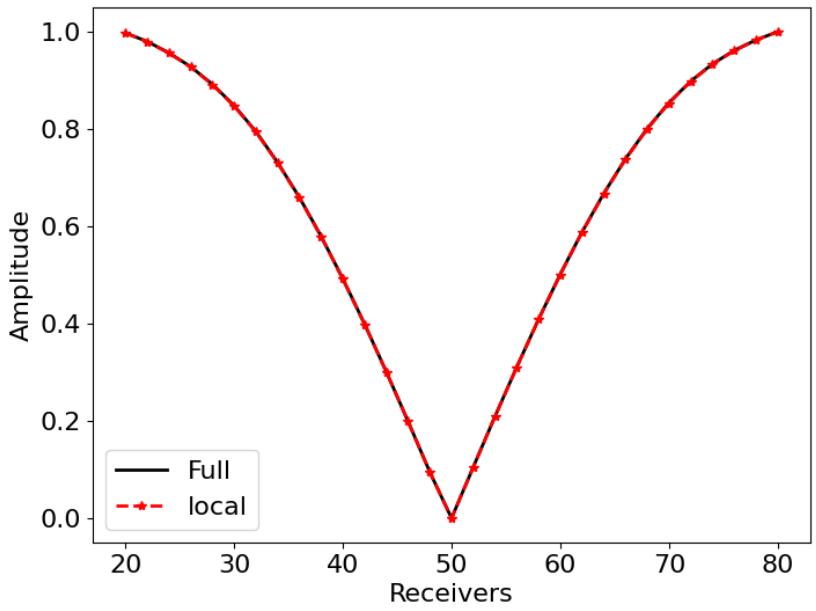

Figure 3.9: Comparing the amplitude extracted from the windowed reflections in Figures 3.7a and 3.7b. The black line shows the amplitude values from the data modeled in the full elastic model (Figure 3.7a). The red triangle dashed line shows the amplitude values extracted using the local solver and the extrapolation methodology (Figure 3.7c). Notice the excellent agreement.

and 3.7c). For comparison purposes, we normalize the curves using the maximum value of the full and local amplitudes, respectively. The amplitude shows a drop at receiver 50, i.e. at approximately $x = 2.5$ km which is consistent with the PP-reflection marked as PP Ref2 in Figure 3.7a. The curves perfectly overlap each other.

Phase measurement

Figure 3.10 shows the phase extracted of PP Ref2 v_x-component within the same time window used in the amplitude measurement (Figures 3.7a and 3.7c). To measure the phase, we adopt the method used by [38] who follow [87] and [99]. As is expected, the phase modeled by the local solver (red triangle dashed line) overlaps almost perfectly with the phase modeled by the full solver (black dashed line). In addition, we see the expected 180^o phase shift present in the reflection of interest at receiver 50 i.e., at approximately $x = 2.5$ km. This sign flip across the origin is expected for this setup.

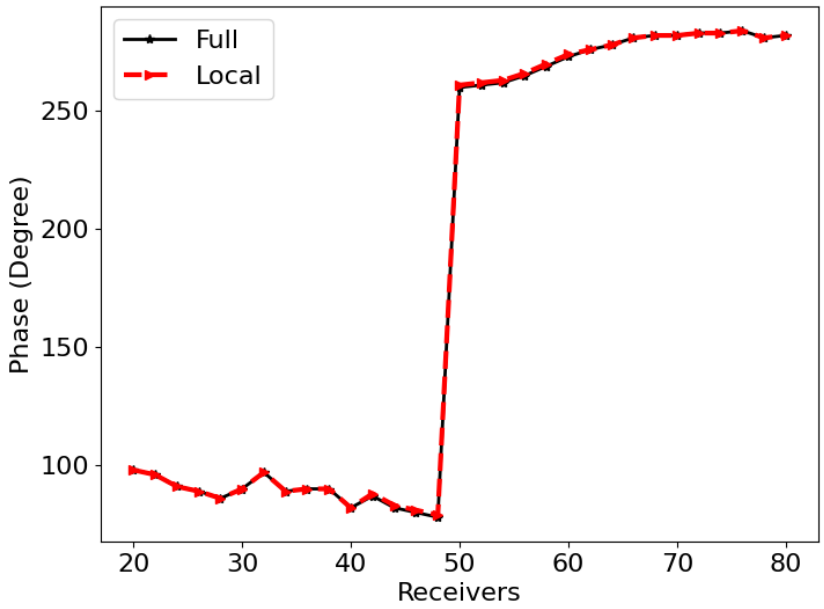

Figure 3.10: Comparing the phase extracted from the windowed reflection in Figures 3.7a and 3.7c. The black line represents phase values from the data modeled in the full elastic model (Figure 3.7a). The red triangle dashed line represents the phase values extracted from the data computed using the local solver and the extrapolation methodology (Figure 3.7c). Again we have excellent agreement between the two algorithms.

3.4.1 SEAM model

We now illustrate the proposed method on a more complicated elastic velocity model. The synthetic model we focus on this section, shown in Figure 3.11, is a subsection of the 2D elastic SEG Advanced Modeling Program (SEAM) model [23]. The dimensions are 5.0 km $\times$ 2.0 km and the grid spacing is 10 m $\times$ 10 m. The source is a 15 Hz Ricker wavelet located at $x = 2.5$ km and $z = 0.1$ km. The receivers are located along the entire horizontal extent of the model at a depth of $z = 0.1$ km. The wavefield is propagated for 1.7 s. The blue box in the P-wave velocity model corresponds to the injection surface S, and the black surface above marks the extrapolation surface S_e in Figure 3.11. Note that the model contains a high-velocity layer inside the local domain. The high-velocity layer was added after the background field was modeled. Otherwise, the scattered wavefield would be zero. As we described above, the MPS method can perform independently of the order of the spatial order of the FD stencil. For this example we use a fourth-order FD stencil.

Figures 3.12a and 3.12b show the v_x-component and v_z-component shot gathers for the full-domain elastic solver, while Figures 3.12c and 3.12d show the v_x-component and v_z-component shot gathers, respectively, for the local solver with the elastic velocity model shown in Figure 3.11. The black arrows mark the reflection of interest in the full v_x-component and v_z-component shot gather which comes from the layer with high velocity located at approximately 1.25 km in depth. Note the remarkable similarity between both shot gathers (top and bottom for each case). The plots are shown with the same colour bar.

Figure 3.13 shows a trace at $x = 2.0$ km between 0.75 s and 0.95 s from the v_x-component shot gathers in Figure 3.12. The black line is the trace from the full-domain simulation (Figure 3.12a), and the red triangle dashed line is the trace simulated with the local solver (Figure 3.12c). The traces overlap each other perfectly as expected. With this example, we show that the methodology is applicable independent of the velocity model used.

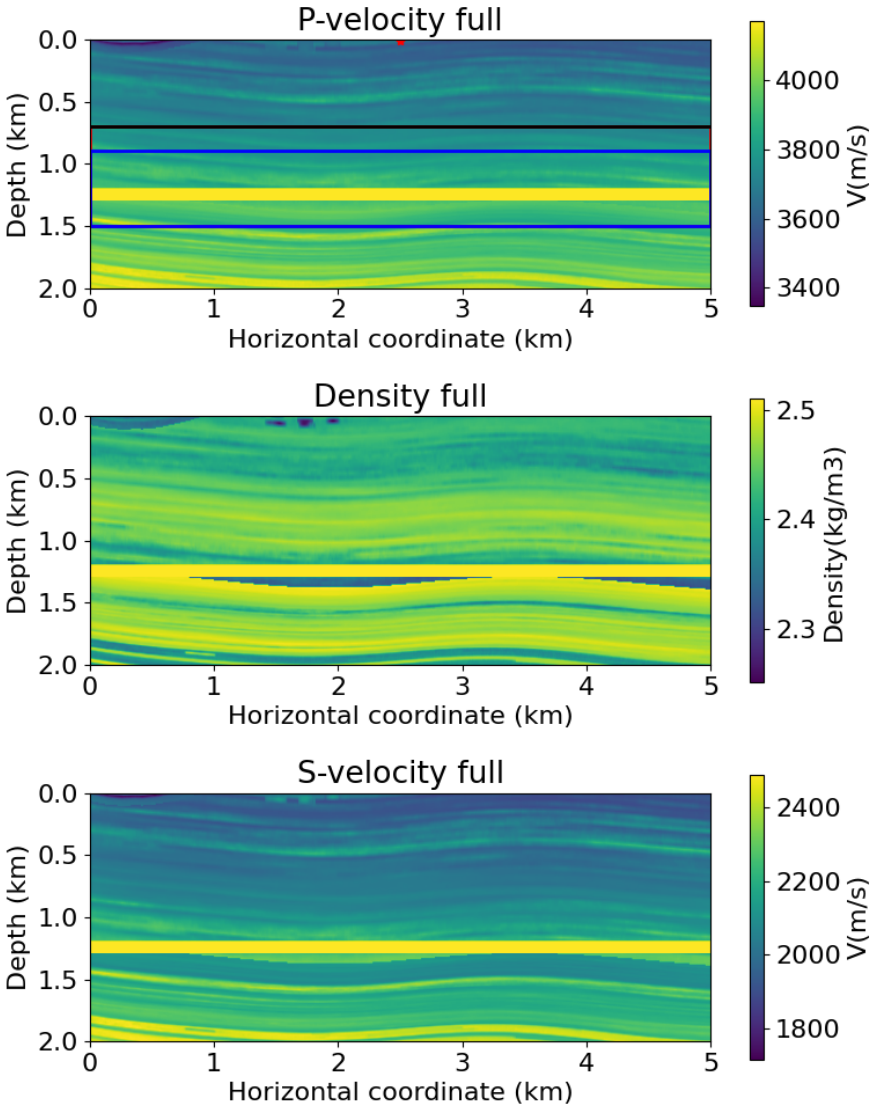

Figure 3.11: Subsection of SEAM elastic model, based on the geology of the Gulf of Mexico [23]. The selected domain is located in x between 11.5 and 16.5 km and z from 6 to 8 km from the original model. The source is located at $x = 5$ km and $z = 0.1$ km (red star at the top of v_p).

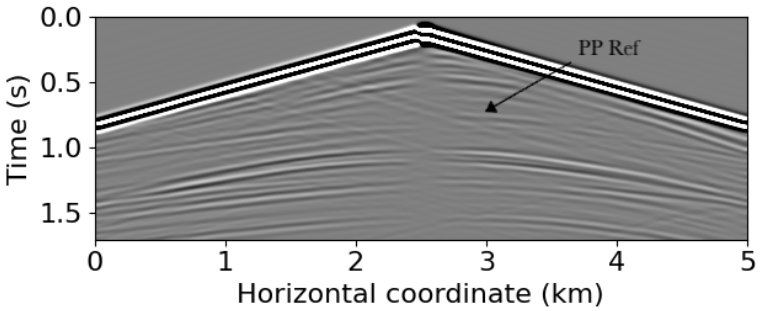

(a): v_x-component full

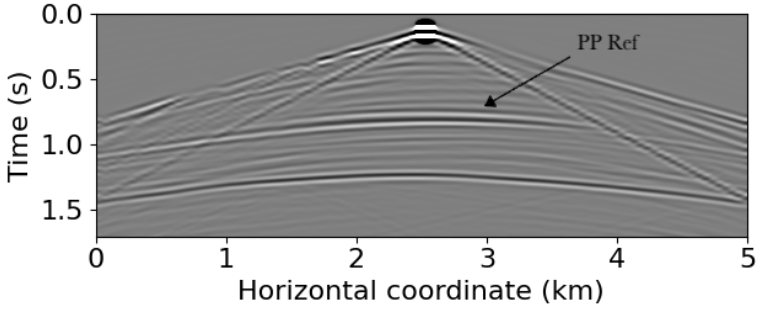

(b): v_z-component full

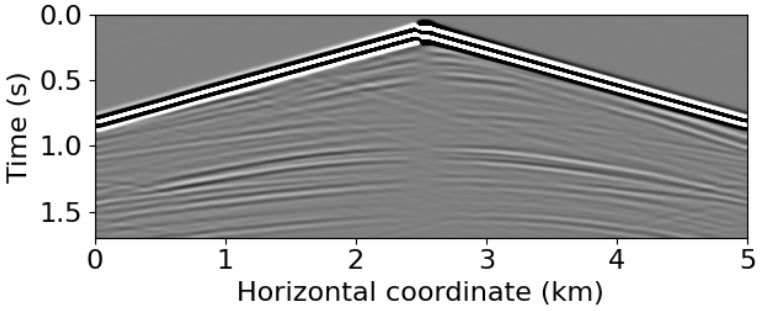

(c): v_x-component local

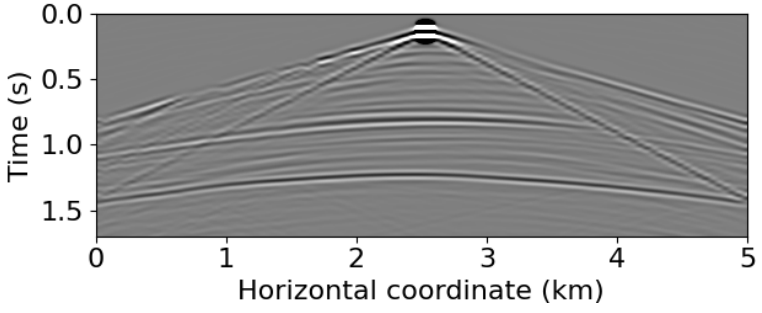

(d): v_z-component local

Figure 3.12: (a) and (c) shot gathers v_x-component and (b) and (d) shot gathers v_z-component for a source at $x = 2.5$ km. The black arrow marks the PP reflection from the layer of interest.

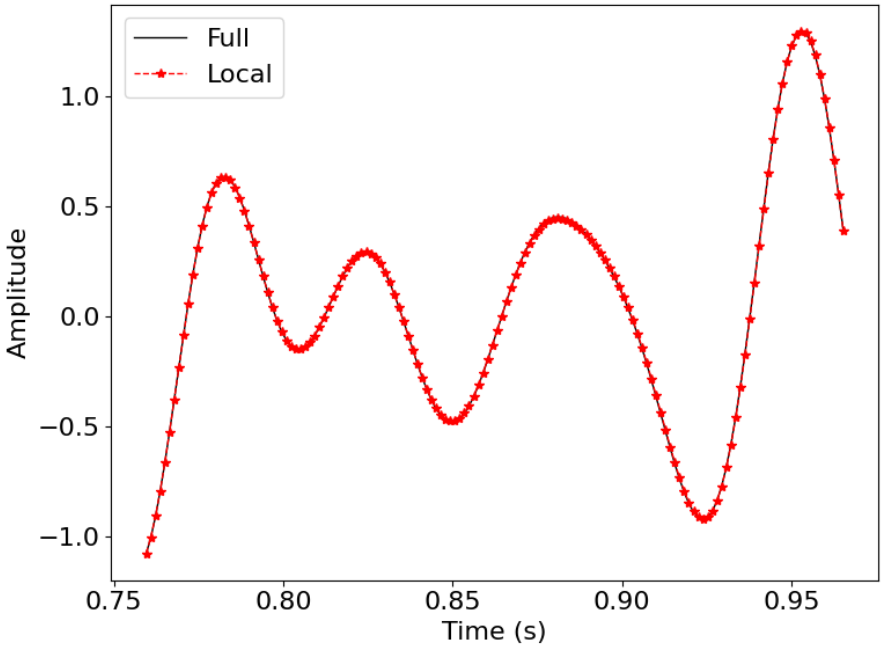

Figure 3.13: Trace comparison at 2.0 km for a shot at $x = 2.5$ km from the v_x-component shot gather in Figures 3.12a and 3.12c. The black line represents the trace modeled with the full solver and the triangle dashed red line plots the trace modeled using the local solver.

3.5 Discussion

The local solver implemented in this paper is based on the injection of wavefields using the MPS method on staggered FD grids. This method uses wavefields that are recorded on a surface with an arbitrary spatial order of accuracy and are later injected back into the FD grid as point sources to produce an exact reconstruction of the PP-reflected wavefields. The way that the wavefield is recorded and injected on S is general; thus, it can be used in FD schemes with different orders of spatial accuracy.

To reconstruct the source wavefield using the MPS method, we need to save five wavefields ($v_x, v_z, \tau_{xx}, \tau_{xz}, \tau_{zz}$) along the boundary S, which requires less memory than conventional methods that need to store at least half of the FD stencil size to ensure accuracy in the source wavefield reconstruction, such as checkpointing methods [73, 96]. The MPS method has been demonstrated by [79] in the acoustic case and used by [44] in elastic RTM. The local solver implementation with the MPS methodology for the reconstruction of the source wavefield makes the local solver even more appealing in memory-intensive applications such as elastic FWI, elastic waveform tomography, and elastic RTM. However, this approach is most useful in situations in which we need to recompute the wavefield locally and iteratively, i.e., updates only in a small region instead of a full model.

When the design of the injection surface includes corner points, minor artifacts appear from the intersection of these line segments. These artifacts have a relatively small amplitude compared to the amplitude of the reflection of interest. In the example we study here, the amplitude of this artifact ranges between $\pm 1 \times 10^{-6}$, whereas the amplitude of the reflections of interest varies from $\pm 1 \times 10^{-3}$. Thus, the error propagating from the corners represents around 0.1% of our reflection of interest. One strategy to overcome this issue is presented by [77] who obtains an exact wavefield in a model with sharp corners by averaging two FD injections to one grid point during the injection step.

There is a trade-off between the spatial grid size and the spatial order of the FD method to obtain the exact reconstruction. Larger spatial sampling values with a high space order can result in mismatches in the amplitude. We use bilinear interpolation to the surface of injection to locate the wavefield at the exact position in the stencils

from which they are injected. Thus, the longer the stencil, the more nodes are used to implement the point sources in the interpolation, causing errors when you have a large spacing. [79] show that there is a region in the vicinity of the injection surface where the wavefield is not exactly reconstructed. The width of this region is proportional to the length of the FD stencil: the higher the spatial order used, the larger the region.

An attractive feature of this methodology is the fact that the scattered wavefield can be extrapolated to the receiver locations at a relatively limited computational cost. The outgoing scattered wavefield from the local domain is recorded on an extrapolation surface, and then we extrapolate this scattered wavefield through an overburden using equation 3.5. We calculate the Green's functions with the FD method, and then we leverage the reciprocity theorem in equation 3.5. This method maintains high accuracy and is appealing if a large number of recalculations are needed or when the seismic response should be modeled for various possible scenarios such as FWI and time-lapse seismic simulations [5, 75, 7].

Although the overburden in the SEAM model includes several layers, it is noted that there is not a large contrast between them. Thus, there is not a large variation in the material parameters for these sediments. Our local solver approach is highly accurate when small-scale perturbations are present in the overburden. However, it can be less beneficial if we want to model wavefields that propagate outside the target region into the unaltered domain and then reenter the local domain. Future work could focus on implementing local elastic solvers that account for all interactions between local and unaltered exterior domains

In the simulation in which we use the two-layer model, the recalculation of the wavefield in the local domain after perturbation required 18% less time than the total time of the simulation in the full domain (i.e., approximateky 82% of the total time). The memory usage for the local domain simulation was 0.8 MBytes compared to the 117 MBytes required for the full forward simulation, which is a significant saving. We are also interested in the extrapolation of the wavefield to the receiver positions. The computational cost for the extrapolation depends on the number of times that you alter the model and the number of receivers. However, the evaluation of equation 3.5 is trivial because we compute the Green's functions only once. If we have multiple sources and receivers and the receivers coincide with the source locations, then we calculate the Green's functions without extra cost. Furthermore, the computational

cost of the Green's functions calculation can be distributed over the number of local simulations for which the local solver is used; i.e., the larger the number of required simulations, the less significant the Green's functions calculations will be per simulation. Finally, the surface S where the injection occurs can be designed to be small compared with the full model and even the local domain. Thus, only a tiny fraction of the source wavefield needs to be stored. In the SEAM example, the entire source injection field for 1300 time steps required 36 KBytes. In contrast, optimal storage of the whole wavefield at all points and times would require approximately 15 GBytes in the full simulation. For 3D models, the savings will be greater, assuming we are able to make similar savings. [61] present a detailed computational cost analysis for the FD-injection and extrapolation method. We expect that our savings will be on the same order, although we may see slightly better results with our implementation because we do not need to store and compute as many Green's functions because we inject along only a single layer, whereas they use at least twice the size of the FD stencil.

3.6 Conclusions

We have described the implementation of the elastic MPS method in a staggered FD scheme and its applicability to a local solver. We show that, using only one surface and five wavefield quantities, we are able to reconstruct the wavefield accurately within a subdomain. We observed that the implementation of the local solver and the extrapolation is efficient in modeling the recorded wavefield. Our implementation reduces the memory required to reconstruct the wavefield. The injection technique and the extrapolation method were validated against full elastic simulations. Finally, we implemented the methodology in a more complex elastic velocity model, showing that it is independent of the model used.

Chapter 4

Inversion comparison using an elastic local solver to recover elastic parameters

4.1 Summary

In many inverse problems such as full-waveform inversion or reverse-time migration the key computational cost is the repeated seismic modeling. Due to data and model spaces dimensions, the inversion algorithms become too costly, so that practical approaches are needed to reduce the dimensionality of the problem. Using local solvers, we can reduce the size of the computational domain to small areas while preserving the fidelity of the elastic wavefield reconstruction. Both the full waveform and extracted amplitudes and phases from seismic reflections are used in geophysical inversions to recover elastic parameters in regions of interest. In this study, we compare full-waveform inversion and amplitude-phase versus offset inversion to recover elastic parameters for a reflector of interest using a local elastic solver.

4.2 Introduction

The full-waveform inversion (FWI) method is the primary method used to retrieve the properties of the subsurface with high resolution. FWI is a technique based

on fitting simulated and observed data, where the solution of the wave equation is the most expensive computational component. Usually, the inverse problem solution involves the computation of forward and adjoint wavefields that are cross-correlated to calculate the gradient that is used to update the model. Thus, for each inverse iteration, the wave equation needs to be solved twice before the full model is updated [75]. Although there are many techniques that reduce computational time, most still work on the entire domain, even though the area of interest is small in most cases.

Local solvers strive to reproduce the wavefield inside local areas as if they were generated using the full domain, reducing the computational domain size and speeding up the inversion process. The development of local solvers can be divided into two categories. The first category was presented by [29] and extended by [78] and [80] in two and three dimensions. This technique is known as the immersive boundary condition (IBC) technique. The idea is based on using an analytic boundary condition to connect an inner and outer domain, and solve the wave equation, potentially with a different method, in each domain. In the second category, the wavefield is initially propagated in the background model and then injected inside the local domain as a set of monopole and dipole sources to obtain the wavefield inside the local area [4, 8]. This wavefield reconstruction method was proposed by [53] and is known as the multiple point source (MPS) method. These techniques have been successfully used in combination with extrapolation in FWI. For example, [61] applied the FD-method in a local domain after model alterations to solve time-lapse seismic problems. [87, 38] illustrate the effectivity of the local solver in FWI, recovering elastic parameters for an area of interest. The FWI with local solvers is based on the assumption that the model only changes in the local area, which implies that everything outside the local domain remains constant.

In this study, we use the second local solver category with the approach proposed by [40]. They use the representation theorem to reconstruct the wavefield inside the local domain, which requires the recorded wavefield on only one surface to reconstruct the source wavefield inside the local domain. Also, in their approach the implementation assumes that researchers build upon an existing code. Thus, their implementation reduces memory while still reconstructing the wavefield with high accuracy. Here, we use this time-domain elastic local solver approach to recover the elastic parameters for a layer of interest. Using the local solver, we compare the results of FWI and an inversion using the extracted amplitude and phase from a reflection of interest.

4.3 Methodology

The local solver aims to compute wavefields after perturbing the model inside local areas and then extrapolates the scattered wavefield from a local surface to the receiver positions. To use the local solver we must first compute a single full-domain simulation. However, after that, we can generate local wavefields much faster than using full-domain simulation. With this formulation, we can update the full shot gather after local model alterations, recomputing only the wavefield within the local areas. In this study, we use the amplitude and phase extracted from the PP-reflection to invert for elastic reflector properties of a layer of interest using the local solver. We then compare the results with full waveform inversion.

Our implementation of the local solver discards the wavefield scattering on the perturbation that leaves the local domain and then reenters it before propagating to the receiver locations. In other words, internal multiples with a single bounce within the local domain are not modeled. This limitation is not of concern here because we are interested in modeling amplitude and phase from the PP-reflection (i.e. primary reflections) that are primarily affected by scattering at the reflector and less by propagations through the heterogeneous elastic overburden [100].

The methodology implemented to model the forward wavefield by using an elastic local solver is explained by [40]. They show that using only one surface of five wavefields, it is possible to reconstruct the wavefield with high accuracy within a local domain. They validate the method by extracting the amplitude and phase and comparing them to those extracted from a full model simulation. This establishes the accuracy of our data.

Figure 4.1 shows a schematic of the local solver. The elastic local solver requires the Green's functions for the elastic background represented by the black wavy lines inside the big white box. The Green's functions in the background are then injected as point sources on an enclosing surface S (black dashed line around the light pink box) to reconstruct the wavefield. The model is only updated inside the local domain (light pink region) which contains the reflector of interest. The gray boxes that surround the full and local domain represent perfect matched layer (PML) boundary conditions. Figure 4.2 illustrates the workflow steps to inject and extrapolate the wavefields in the local solver.

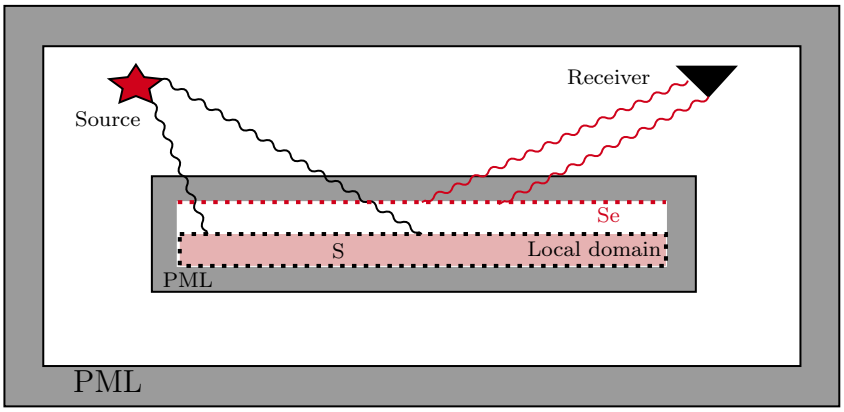

Figure 4.1: Schematic of the local solver. The dark gray layers represent the perfectly matched layers (PML) on the boundary. The model is perturbed and the scattered field is updated within the local domain (light pink region). The injection occurs on the injection surface S (black dotted line) and the extrapolation to the receiver locations takes place from the extrapolation surface S_e (red dashed line).

Amplitude and Phase Inversion

Once the amplitude and phase of the reflected wavefields are updated at the receiver positions, we proceed to obtain the reflection coefficient values as a function of angle. To measure amplitude and phase, we first isolate the event, picking a time-window that includes only the reflection of interest (red lines in Figure 4.4). To extract the amplitude we take the Hilbert transform and then take the maximum value of each trace to obtain each angle's reflection coefficient. To measure the phase we adopt the method used by [38] who follow [87] and [99]. They use the observation that a zero-phase wavelet has maximum correlation with its envelope. The details of the outlined algorithm are presented by [99].

To perform the amplitude and phase inversion, we minimize the least squares objective function:

$$\Gamma(\mathbf{m}) = \frac{1}{2}\|\Lambda(\mathbf{d}) - \Lambda(\mathcal{L}(\mathbf{m}))\|_2^2 \tag{4.1}$$

where $\mathcal{L}$ represents the elastic local solver, $\mathbf{d} = (\mathcal{A}_r, \mathcal{P}_r)$ is a vector that contains the recorded amplitude and phase and $\mathbf{m} = (\mathcal{A}_m, \mathcal{P}_m)$ is the vector that contains the modeled amplitude and phase. Both amplitude and phase are functions of the elastic parameters of the layer of interest (v_p, ρ, v_s). Writing out equation 4.1 in terms of

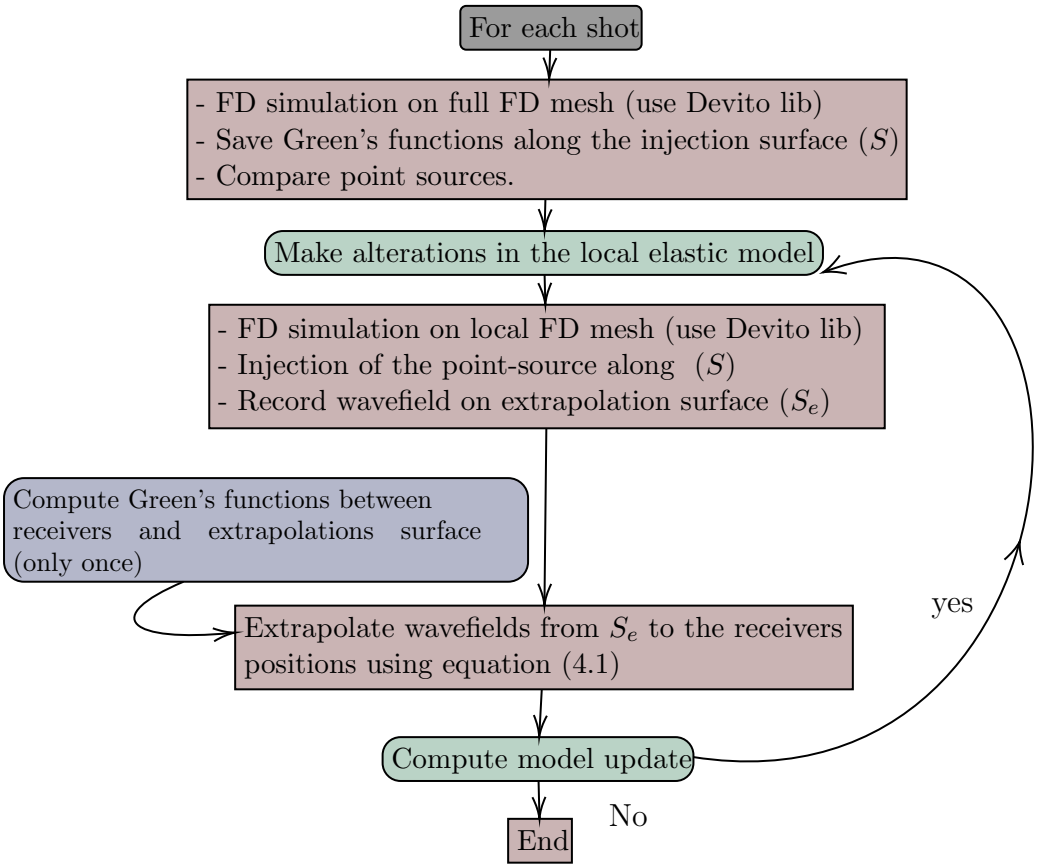

Figure 4.2: Workflow showing the injection and extrapolation of the local solver. Based on [40].

phase and amplitude gives,

$$\Gamma(\mathbf{m}) = \left\| \frac{\mathcal{P}_r - \mathcal{P}_m}{max(\mathcal{P}_r)} \right\|_2^2 + \left\| \frac{\mathcal{A}_r - \mathcal{A}_m}{max(\mathcal{A}_r)} \right\|_2^2, \tag{4.2}$$

where $max(\mathcal{P}_r)$ and $max(\mathcal{A}_r)$ represent the maximum values of the phase and amplitude of the recorded data, respectively.

Our focus is the multi-parameter inversion to estimate the elastic parameters v_p, ρ, v_s of the layer of interest. Involving several parameters increases the nonlinearity of the inversion process, introducing parameter crosstalk and trade-off [54]. We use the Gauss-Newton method that mitigates the coupling effect between parameters to minimize the misfit function $\Gamma(\mathbf{m})$ [54, 75].

Full waveform Inversion

Here we are comparing full waveform inversion and amplitude and phase inversion using a local solver. Thus, we also perform a full waveform inversion, minimizing the least squares objective function described in equation 4.1. However, in this case $\mathcal{L}$ represents the elastic full simulation, $\mathbf{d}$ is a vector that contains the full recorded shot gather and $\mathbf{m}$ is a vector that contains the modeled shot gather. The simulated shot gather is a function of the elastic parameters (v_p, ρ, v_s) at the layer of interest. We again use the Gauss-Newton method to minimize the least squares objective function in equation (4.1).

4.4 Results

In this section, we investigate if the amplitude and phase modeled by the local elastic solver can be used to invert for elastic parameters. Then, we compare these results with those of full waveform inversion. To perform the comparison, we use a subsection of the 2D elastic SEAM model shown in Figure 4.3 [23]. The dimensions are 10 km $\times$ 2.0 km and the grid spacing is 20 m $\times$ 10 m. The source is a Ricker wavelet that generated a P-wave only, injected in x and z directions. It is located at $x = 5.0$ km and $z = 0.1$ km with a central frequency of 15 Hz. 50 receivers are located along the entire horizontal extent of the model at a depth of $z = 0.1$ km. The wavefield is propagated for 2 s.

Figure 4.3a shows the initial P-velocity model where we compute the background wavefield and then save along the injection surface (red box). This is step 1 in the workflow (Figure 4.2). Figure 4.3b shows the perturbed P-velocity model where the injection of the Green's function occurs as point sources around the local domain. This is step 2 in the workflow in Figure 4.2. In this example, we work with the method that has fourth space-order accuracy in space. The yellow line represents the extrapolation surface where the scattered wavefield is saved and then extrapolated to the receiver surface.

Figure 4.4 shows the v_x shot gather component obtained by using a full elastic solver (top) and the local solver (bottom) with the elastic velocity model shown in Figure 4.3. The black arrow marks the reflection of interest that comes from the layer

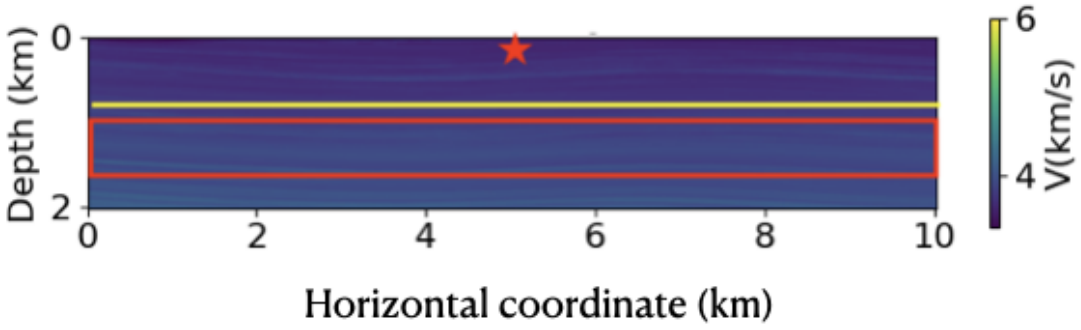

(a): Initial model

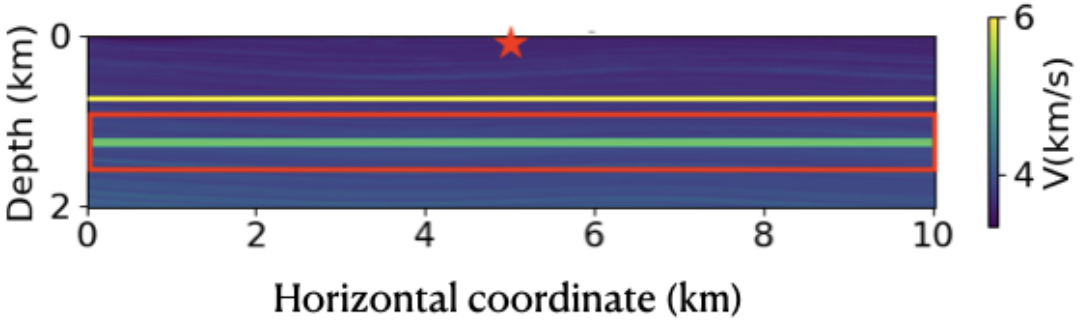

(b): Perturbed model

Figure 4.3: (a) initial P-velocity model and (b) perturbed P-velocity SEAM elastic model, based on the gulf of Mexico [23]. The selected domain is located in x between 23 and 33 km and z from 6 to 8 km in the original model. The source is located at $x = 5$ km and $z = 0.1$ km (red star at the top). The red box shows the injection surface S and the yellow line the extrapolation surface S_e. Notice the layer introduced in (b) around 1.25 km in depth to perturb the elastic velocity model.

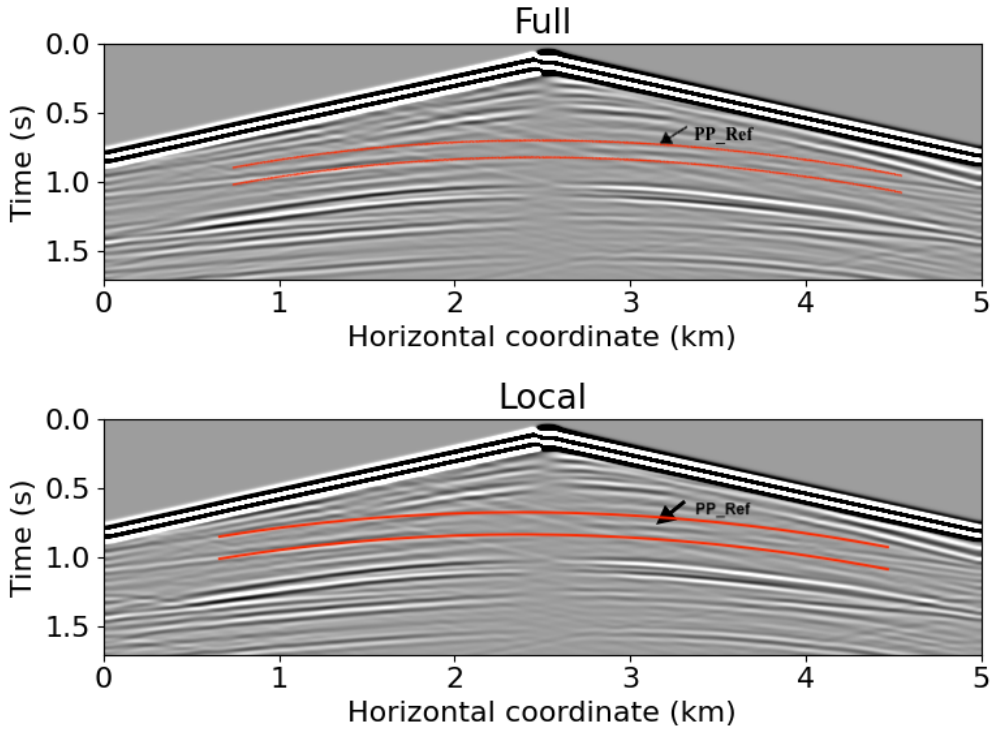

Figure 4.4: Shot gathers for a source at $x = 2.5$ km with the full (top) and local (bottom) solvers. The black arrow marks the reflection of interest from a layer located around 1.25km in depth in the model (Figure 4.3). The red lines mark the window used to extract the amplitude and phase from the PP-reflection. Both shot gathers are plotted on the same colour scale.

with high velocity located around 1.25 km in depth in the model (see Figure 4.3). The red lines represent the time window that is used to measure the amplitude and phase of the reflection. Both shot gathers show a measurable similarity with a percentage of error equal to 8.06x10^{-}05, demonstrating that the shot gather can be updated with high accuracy using the elastic local solver. The plots are shown with the same colour bar.

Inversion

After observing that the local solver accurately updates the shot gather, we now focus on inverting elastic material parameters at the reflector of interest. We first use amplitude and phase with the local-elastic solver. Then we perform a full waveform

inversion. Notice that in the first scenario, i.e when the amplitude and phase are used with the local solver in the inversion, we presume that we know the overburden. Thus, we invert only for elastic properties present in the layer of interest i.e. at 1.25 km depth in the SEAM model. In total, we invert for three parameters, two velocities and one density (v_p, v_s and ρ) in both inversion scenarios.

Figure 4.5 shows the amplitude (a) and phase (b) evolution for a few iteration numbers. We see that the amplitude and phase residuals get progressively smaller as the amplitude and phase inversion progresses. The black curves represent amplitude and phase obtained for the true model with full simulation, and the yellow represents the amplitude and phase obtained for the true model with local simulation. Because the amplitude and phase from the true and local simulation agree quite well, we expect to recover the model with high accuracy.

Figure 4.6 shows the evolution of the model m_i as a function of iteration number i for one-shot located at 2.5 km for (a) amplitude and phase inversion and (b) full-waveform inversion. All curves are normalized using the true value, hence all the curves will approach 1.0 for the perfect case. We see that all parameters in amplitude and phase inversion as well as in full-waveform inversion converge to the true model after five iterations. The first three iterations show large updates, and v_s appears to diverge during the initial iteration for the amplitude and phase inversion. However, after later iterations, the convergence behaviours are smooth and incremental. Table 4.1 shows the true, initial and inverted model parameters for the layer of interest at 1.25 km depth in Figure 4.3 for the amplitude and phase inversion (top) and the full waveform inversion (bottom). The initial model improves significantly for both amplitude and phase inversion and full waveform inversion. The error for all parameters for the amplitude and phase inversion is 0.1%. In contrast, the error in the recovered parameters using full waveform inversion is around 0.03%. With this example, we show that the local elastic solver with the amplitude and phase as constraints can retrieve elastic parameters with a similar accuracy to full waveform inversion.

Comparing the computational cost for the amplitude and phase inversion and full waveform inversion, we found that the full waveform inversion requires 15 GBytes for storage of the whole wavefield at all points and time steps, whereas the source injected in the local simulation requires only 36 KBytes. The total time for each iteration in

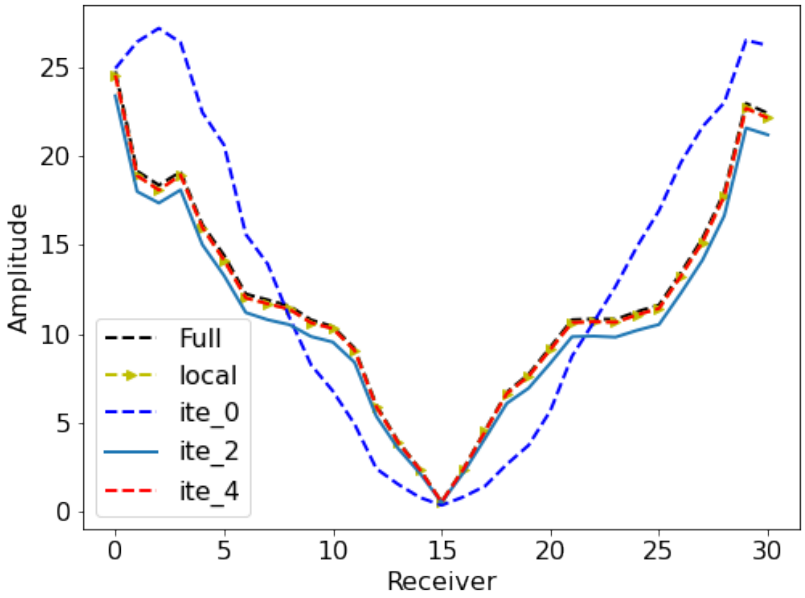

(a): Amplitude

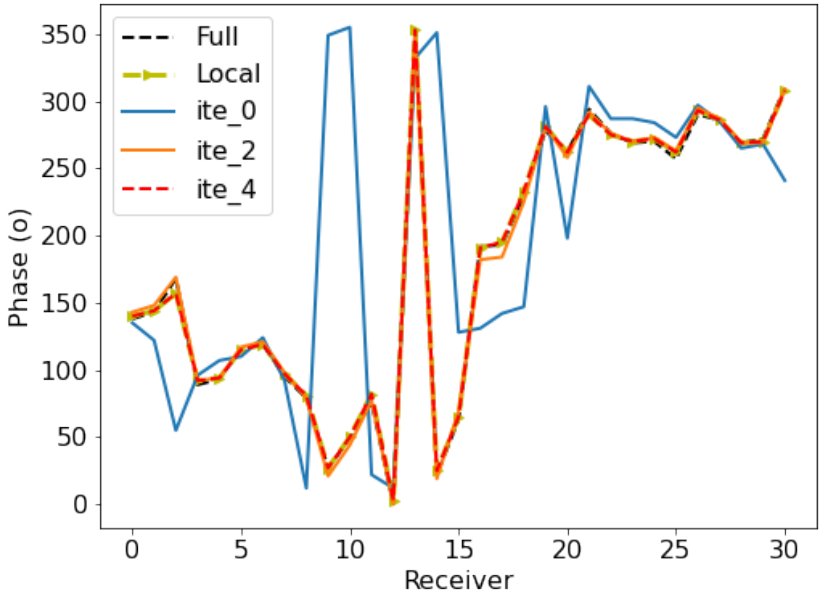

(b): Phase

Figure 4.5: (a) amplitude and (b) phase extracted from the windowed reflections in Figure 4.4. The black dashed lines represent the amplitude and phase values from the data modeled in the full model. The red triangle dashed lines represent the amplitude and phase values extracted using the local solver. ite_n represents the recovered values at iterations n.

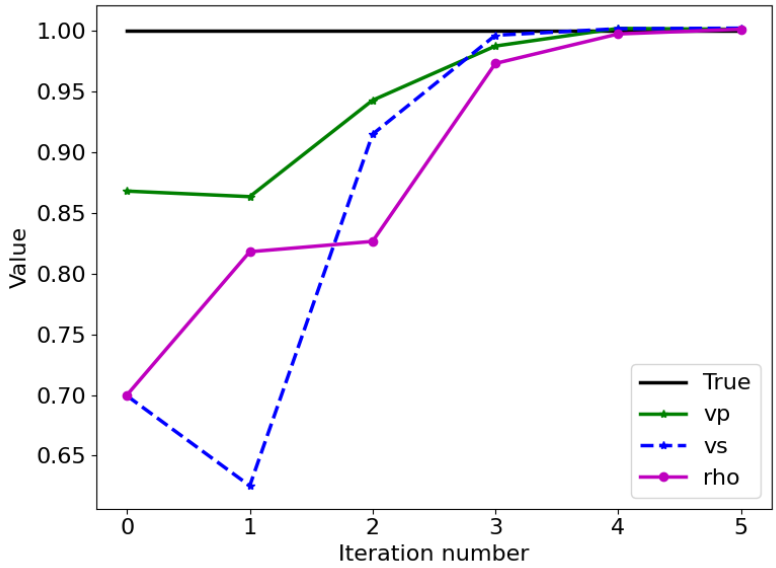

(a): Local

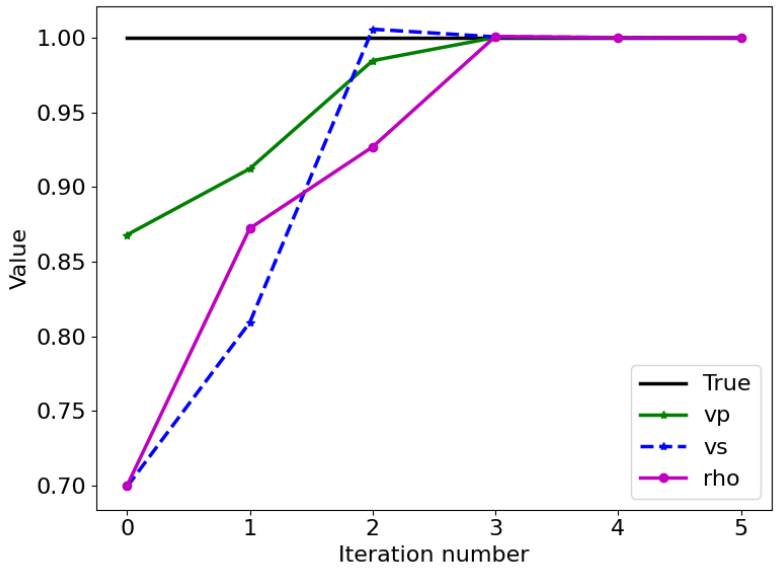

(b): Full

Figure 4.6: Normalized model evolution during (a) amplitude and phase inversion, (b) full waveform inversion. Black line refers to the true model.

Amplitude and phase inversion using a local solver					
	True	Initial	Error	Inverted	Error
v_p (m/s)	5300	4600	13.2%	5306	0.1%
ρ (kg/m^3)	3000	2100	30.0%	3003	0.1%
v_s (m/s)	2860	2000	30.1%	2865	0.1%
Full waveform inversion					
	True	Initial	Error	Inverted	Error
v_p (m/s)	5300	4600	13.2%	5300.1	0.01%
ρ (kg/m^3)	3000	2100	30.0%	3001.0	0.03%
v_s (m/s)	2860	2000	30.1%	2859.5	0.01%

Table 4.1: P-velocity, S-velocity and density inverted for the layer of interest. The top rows show the parameters inverted using the local solver. The bottom rows show the parameters inverted using the full solver

the amplitude and phase inversion is about 82% of the full simulation, saving 18% per iteration compared with the full waveform inversion. A more detailed computational cost analysis for a local simulation is presented by [61]. Although their analysis is not for the same implementation, our saving is slightly better since the local simulation that we are using does not need to store and compute as many Green's functions as in the FD-injection method.

4.5 Conclusions

Numerical tests show that the inversion using amplitude and phase with a local solver can retrieve elastic parameters with an error of less than 0.2%. However, the standard FWI approach gives an error that is, on average, smaller by a factor of 10, i.e., 0.02%. We found that the memory required for FWI is substantially larger than that for amplitude and phase inversion. We also compare time costs, indicating that amplitude and phase inversion saves around 18% per iteration compared with full waveform inversion. Given the small error in both cases, using the phase and amplitude rather than the full wavefield may be beneficial if a large number of re-calculations are needed.

Chapter 5

Recovery of the elastic parameters in a complex velocity model

5.1 Summary

Imaging complex structures involving strong contrast interfaces is challenging because of the difficulty in estimating and updating complex velocity models and geometries. This is a problem that is faced by both geophysics and medical imaging. Both industries also share time and computational limitations. In geophysics, due to the dimensionality of the problem and in medicine because real-time results are desirable. Our local solver with Amplitude Variation with Offset (AVO) and Phase Variation with Angle (PVA) inversions have shown promising results, reducing the dimensionality and time required while allowing complex wave propagation techniques to be applied around complex velocity models. However, these methods do not use converted wave modes as constraints in the inversion, and therefore, fail to recover elastic parameters in the presence of complex scattering. We evaluate how the focusing and defocusing of migrated images with elastic reverse time migration (RTM) as an objective function could be used to retrieve elastic parameters in complex velocity models with the goal of ultimately computing these velocity updates with the local solver. The evaluation is developed, first, in synthetic data that contain a large impedance contrast layer. Then, we analyze the migrated images using ultrasound lab data of the scattering from a polymethyl methacrylate (PMMA) tube.

5.2 Introduction

Imaging techniques strive to create a detailed image of the subsurface using reflected data. However, obtaining a clear image of a complex velocity model involving large impedance contrast interfaces is challenging. Techniques such as FWI and RTM have been developed to produce high-resolution delineations of the subsurface [75, 5]. However, these approaches struggle in the presence of interfaces with large impedance contrasts, resulting in models with a lack of sharp interfaces and back-scattered artifacts in the final image [45].

FWI is a technique that seeks to retrieve elastic parameters by measuring an objective function in the data domain while handling the complex wave propagation around complex velocity models. Therefore, it has recently been applied to large impedance contrast scenarios [55, 69, 34]. Approaches focused on reconstructing salt velocity models towards imaging improvement and interpretation of salt bodies with FWI, are also a topic of current interest. For instance, [98] use travel-time misfits measured in frequency dependent time windows as the FWI cost function to correct the interpretation of salt images. [34] propose a reflection full waveform inversion (RFWI) workflow to improve sub-salt images. [89] apply a local solver to generate the FWI gradient at the salt body boundary; then, the gradient is used in a level set method to update the salt boundary. [16] use shape optimization with level sets to refine 3D models of salt bodies at depth using field data. However, the success of these FWI methods relies on the initial guess of the velocity geometry and parameters. Inversions that start with a model that is far away from the truth often lead to incorrect models. Therefore, the most common practice to update salt geometries remains through RTM angle gather methods [43, 92].

RTM is a technique widely used in geophysics for seismic imaging [5]. Conventionally, RTM consists of two steps: (1) the construction of source and receiver wavefields using an estimated wavelet and the recorded data, respectively, and (2) the application of an imaging condition [14]. The source and receiver wavefields are reconstructed using the wave equation, which depends on the properties of the model (e.g. velocities and densities). These multicomponent wavefields allow a variety of imaging conditions [19, 93]. A simple imaging condition is formed by cross-correlating the cartesian components of the displacement for the source and receiver wavefields. For example, in a 2D elastic domain, where we record two-component data, this results in four

different combinations providing four different images. A drawback of these imaging conditions is that the mixed P-and S-wave modes in the source and receiver wavefields create artifacts in the final image, making its interpretation challenging. Using multicomponent imaging conditions, it is possible to first decompose the wavefields into different modes (e.g. P- and S-wave modes) and then cross-correlate them to create different imaging conditions, overcoming the crosstalk between P- and S-wave modes while preserving elastic attributes such as the amplitude and phase of migrated images [18, 93]. We again obtain four different imaging conditions in this scenario, but now they are based on the physical P- and S-wave modes.

Both FWI and RTM methods are based on the propagation of wavefields, which is the most computationally intensive component for inversion and seismic imaging schemes. Methodologies to reconstruct the wavefield locally have been implemented to reduce the cost of the wavefield extrapolation by reducing the size of the model while providing the same features as an extrapolation performed from the source [4, 61, 8, 87, 39]. Local solvers attempt to speed up the nonlinear problem in the inversion and migration processes, reducing the dimensionality of the domain and, as a result, the time and memory required. Local solvers combined with amplitude and phase inversion have been successfully used to retrieve elastic parameters for large impedance contrast interfaces [87, 39]. However, these methods rely on PP reflections, discarding converted wave modes, which provide crucial information to estimate S-wave velocities in complex velocity models. In this study, we take these works to the next level, incorporating S-waves into the objective function by analyzing the focusing and defocusing of migrated images with an elastic RTM. At the same time, we improve the resolution of the images by incorporation S-waves. We focus our analysis on the migrated images created with P- and S-wave modes.

Using target-oriented imaging also has applications outside seismic imaging, for instance, medical imaging of high-impedance contrast targets such as bones. The target and acquisition methods can vary, but the imaging methods are conceptually similar. In fact, measurement of the P-wave is a topic of interest since the 70s in particular after the development of ultrasound tomography [31, 30]. More recently, studies are focused on measuring sound speed fully, i.e. P- and S-wave measurement. This is because of the efficiency of tomography as a non-invasive method that helps detect diseases like cancer [26, 70, 37]. An example of this is the research done by [59], who investigate the estimation of parameters in a transversely isotropic cortical bone

model (model with P- and S-wave anisotropy) using the unfocused beams transmission and the autofocus methods. Thus, applying these targeted techniques from Earth science into the medical field can illuminate crucial aspects of both scientific domains. In this study, we present an evaluation of migrated images using as a target laboratory data of the scattering from a poly methacrylate (PMMA) tube, allowing us to evaluate a complex velocity model involving large impedance contrast interfaces as a case study.

5.3 Theory

In this section, we summarize the measurement of defocusing or focusing of a migrated image. Then we summarize the underlying elastic RTM theory and the imaging conditions using P- and S-wave modes. In this study, we use multicomponent data to incorporate converted PS waves in the interpretation. Our particular interest is in determining which imaging condition provides the best results for P-wave acquisition at source and receivers such as marine and bone data acquisition. We test different imaging conditions to define which wave modes are most useful in imaging this kind of data.

Elastic image domain inversion

Data-domain inversion such as local FWI are designed to estimate model parameters by fitting the observed data with simulated data. In this study, instead of minimizing the data misfit, we update the velocity model by optimizing the quality of the image. This technique is known as image domain wavefield tomography [62, 65, 97]. If we assume that an observed image $I_{obs}(\mathbf{x})$ is available, a simple least-squares objective function can be written as

$$\Gamma(m) = \|I(\mathbf{x}) - I_{obs}(\mathbf{x})\|^2, \tag{5.1}$$

where I is the image we want to construct, m is the velocity model to be recovered. However, this method is not commonly used for initial model building due to the lack of target images. Instead, we can measure the focussing or quality of the image, which is strongly dependent on the accuracy of the velocity model [63]. In this scenario, the objective function measures the image incoherency caused by model errors;

this method is known as Differential Semblance Optimization (DSO) and is commonly used in the velocity building process [72, 71]. The essence of DSO is to minimize the difference between the reflection events in common-image gathers (CIGs). The CIG is defined as a subset of the whole image with fixed surface location. The CIGs can be created, for example, as a function of the data offset or angle known as Offset Domain Common Image Gathers (ODCIGs) or Angle Domain Common Image Gathers (ADCIGs), respectively [66, 68].Thus, the new objective function that measures the focusing is defined as

$$\mathcal{J}(m) = \frac{1}{2}\|PI_{CIG}\|^2, \tag{5.2}$$

where I_{CIG} represents the CIGs and P is the DSO operator that removes the focussed energy, and highlights the energy that is not focussed [67]. Before performing the inversion by minimizing equation 5.2 using the local solver, we need to analyze different imaging conditions to determine which imaging condition provides the most suitable results. In the next section, we present different multiparameter imaging conditions using elastic RTM. Note that our focus is to analyze the migrated imaging conditions created with P- and S-wave modes.

Elastic reverse time migration (RTM)

Elastic RTM is a robust technique used for imaging in complex velocity models. In the elastic domain this technique involves vector wavefields which allow multiparameter imaging conditions. To form PP, PS and SS images separately, the wavefields should be separated during migration [18, 93]. [18] show an approach to separate the extrapolated wavefield into P and S potentials before the cross-correlations of the scalar P and vector $\mathbf{S}$ potentials. However, their approximation is not commonly used in the isotropic elastic wavefield equation, instead we use the Helmholtz decomposition

$$\begin{aligned} P &= \nabla \cdot \mathbf{V}(x,z) \\ \mathbf{S} &= \nabla \times \mathbf{V}(x,z), \end{aligned} \tag{5.3}$$

In equation 5.3, $\mathbf{V}(x,z)$ represents a vector wavefield obtained from the forward solver, for example. In an isotropic elastic medium, P represents the compressional component of the wavefield propagating at speed v_p and $\mathbf{S}$ represents the transverse components of the wavefield, traveling at speed v_s [2].

In elastic RTM, we forward propagate the source to simulate a source wavefield $\mathbf{V}_s(x,z)$ and backpropagate the recorded data to form a receiver wavefield $\mathbf{V}_r(x,z)$ [5]. Using the Helmholtz decomposition (equation 5.3), we separate $\mathbf{V}_s(x,z)$ into a compressional component P_s and a transverse component $\mathbf{S}_s$ for the source and $\mathbf{V}_r(x,z)$ into a compressional component P_r and a transverse component $\mathbf{S}_r$ for the receiver. By combining the separated wave modes, we can form different imaging conditions, P_sP_r, $P_s\mathbf{S}_r$ $\mathbf{S}_sP_r$, and $\mathbf{S}_s\mathbf{S}_r$ [93]. For simplicity, we use the notation I_{PP} for the image formed with P_sP_r, I_{PS} for the image formed with $P_s\mathbf{S}_r$, I_{SP} for the image formed with $\mathbf{S}_sP_r$, and I_{SS} for the image formed with $\mathbf{S}_s\mathbf{S}_r$. Thus, for example, the imaging condition for I_{PS} is

$$I_{PS}(x,z) = \sum^{S} \int_0^T (\nabla.\mathbf{V}_s(s;t,x,z))(\nabla \times \mathbf{V}_r(s;T-t,x,z))dt, \tag{5.4}$$

where S represents the number of sources, T is the record length, and s in $(s;t,x,z)$ and $(s;T-t,x,z)$ indicates data for each source (i.e. it is a parameter, not a variable in this equation). The rest of the images can be defined in a similar way. Without loss of generality, we focus our analysis on I_{PP}, I_{PS} and I_{SS}. Therefore, images created with the separated P- and S-wave modes for the incident and reflected waves have a clear physical meaning making them easier to interpret.

5.4 Numerical examples

We analyze these imaging conditions in two data sets. We use a synthetic model that contains a large impedance contrast layer to create the first set of data. The second one is an ultrasound transverse plane real experimental dataset of a polymethyl methacrylate (PMMA) tube, i.e. an isotropic, elastic material, acquired by [59].

5.4.1 Synthetic longitudinal plane data

We create this synthetic dataset using the elastic finite difference solver contained within the seismic package, Devito, [47] with the velocity model shown in Figure 5.1. We use perfectly matched layer boundary conditions to cover all four sides of the model, thus, no surface multiples are generated. For this simulation we use a Ricker

wavelet that generates primarily a P-wave with a peak of frequency of 25 MHz as a source. In total we use 96 sources that are located along the top of the model at a depth of $z = 0.1$ mm and with a separation of 1.25 mm between them; the sources are modelled one at a time. We place 96 receivers on the surface at the same depth as the sources, evenly spaced at an interval of 0.26 mm. We record the x and z components of the wave for 20 μs.

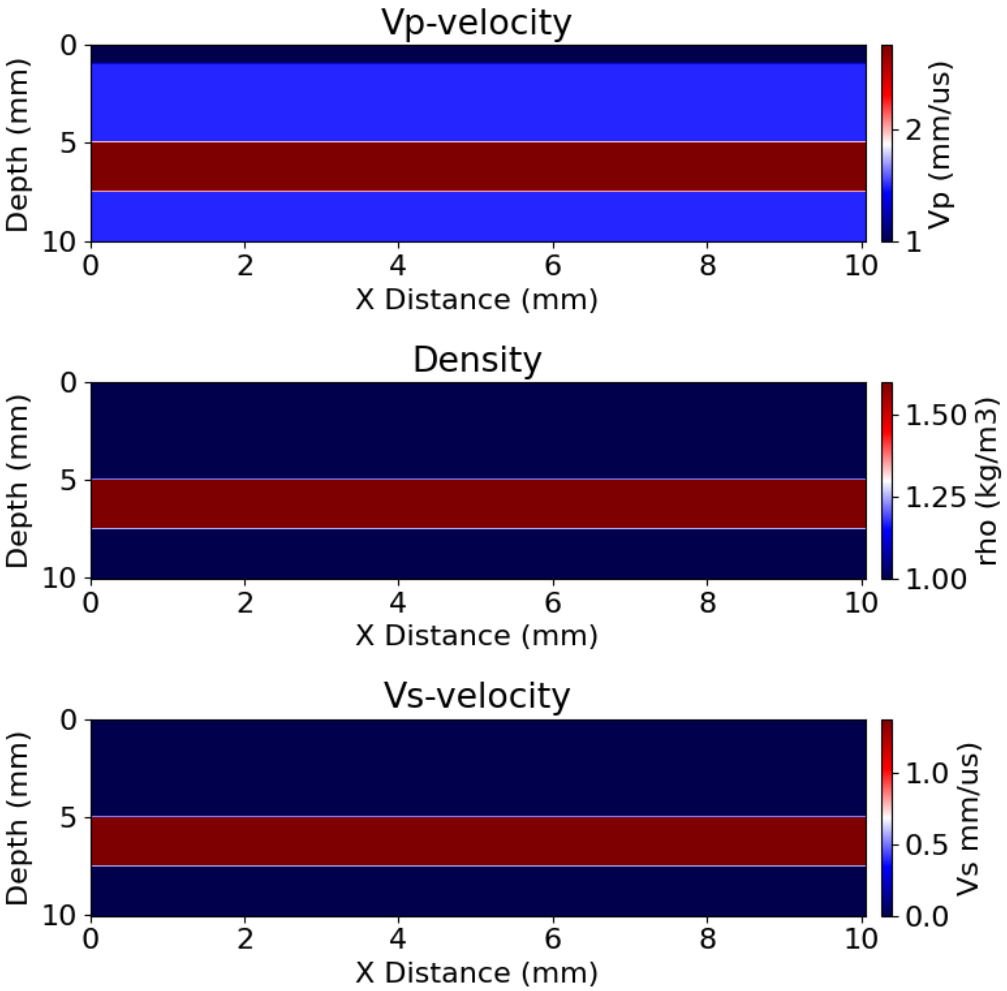

Figure 5.1: Elastic velocity model showing a high-contrast velocity layer at $z = 5$ mm.

We assume that throughout the velocity model building, smooth versions of the P- and S-wave velocity models are available. We perform elastic RTM using the smooth P- and S-wave velocity and density models. Figure 5.2 shows I_{PP}, I_{PS}, I_{SS} images.

The images are formed by stacking the RTM images generated separately for each shot. Because we are interested in the large contrast impedance layer, we cut 1 mm off of the top of the image to remove source artifacts. Notice that the illuminated regions are different between the different imaging conditions. This is due to different illumination angles of the two propagation modes (i.e. P- and S-wave modes). The reflectors present in the model are clearly defined in all images, but with different strengths. For example, in the I_{PP} and I_{PS} images the deeper reflector has lower amplitude compared with I_{SS}. In addition, I_{PS} shows a phase-shift along the first reflector due to the polarity reversal of the converted P- and S-waves. These changes in the polarity are observed around 1.5 mm, 5mm, and 8.5 mm in Figure 5.2b. We can correct the polarity reversal by incorporating other methods such as the angle decomposition technique [93, 33]. Notice that I_{PP} shows noise below and above the top and bottom of the large contrast layers which is due to multiply-reflected waves. These multiples can be well attenuated in the data with the combination of sparse hyperbolic radon transform, and predictive deconvolution [64, 20]. I_{SS} shows a clean and well defined image that includes both top and bottom reflectors. Thus using I_{SS} in the interpretation process is advantageous because it better illuminates deeper large contrast interfaces. These results suggest that the decomposed wavefield image produced could be applied to estimate shear and compressional speeds in models that contain large impedance contrasts.

5.4.2 Transversal PMMA tube — Real data

Our previous results are promising to image velocity models with large impedance contrasts; however, models with large impedance contrasts usually contain complex geometries such as salt bodies in geophysics or the head of the femur, knees or the skull bones in the medical field. To take a step closer to these more complicated models, we now evaluate the imaging conditions in a polymethyl methacrylate (PMMA) tube dataset acquired by [59]. These data introduce both a large impedance interface and complex geometry, giving us better insight into the imaging condition behaviour.

The ultrasound data are acquired with an ultrasound transducer array positioned in the transverse plane. They used a conventional clinical ultrasound probe which is made of a linear array of independent piezoelectric elements. Each transducer element is activated one at time and all transducers record the resulting reflections.

This acquisition method and conventional 2D seismic acquisition in exploration geophysics are similar, where a source generates a spherical wave and an array of geophones/hydrophones records the reflections. Figure 5.3 illustrates the acquisition configuration. The transducer contains 96 elements spaced 0.295 mm apart recording for 35 μs and a peak ultrasound frequency of 2.5 MHz.

Figure 5.4 depicts the best estimation of the P-wave velocity (smooth function between 1.0 and 3.0 mm/μs), S-wave velocity (smooth function between 0.0 and 2.0 mm/μs) and the density ρ (smooth function between 1.0 and 1.64 kg/mm^3) of the PMMA tube data. The outer and inner diameter of the tube are 20 and 8 mm, respectively. The PMMA tube is suspended in deionized water with a speed of approximately 1.5 mm/μs.

For this geometry, the velocity model is significantly more complicated than the longitudinal model described previously. The large impedance contrast and complex shape of the PMMA tube make imaging the interior and sides extremely challenging as the high velocity of the tube causes waves to scatter at sharp angles, leading to little recorded energy at the surface. In addition, imaging is challenging due to the significant amounts of energy that are multiply scattered.

We illustrate the challenge of this geometry by analyzing the wavefield propagation and v_z-component shotgather modeling with the velocity model in Figure 5.4. Figure 5.5 shows snapshots of the simulated wavefield and a v_z-component shotgather. We can see from the wavefield propagation that both head and guided waves are present within the tube, pointed out in Figure 5.5b and 5.5c with number 4 and 7, respectively. Figure 5.6 illustrates a cartoon of these ray paths. Notice that the propagation of the head wave occurs along the curved surface (Figure 5.5b and Figure 5.6 number 4); thus, it does not appear as a straight line in the shotgather. Instead, it seems to be a split in the top of the tube reflection at far offsets (Figure 5.5, bottom: shotgather number 4). The direct wave also has a complex path once it reaches the inner part of the tube, reflecting off both sides of the inner part of the tube before being reflected to the surface (Figure 5.5b, c and d green arrow). This is observed at approximately 27 μs in the shotgather (Figure 5.5, bottom: shotgather number 6). The energy in the interior of the tube is scattered multiple times, which complicates the velocity estimation and image significantly. For instance, the bottom reflector of the tube could appear distorted and deeper than its actual location in the migrated image,

even when imaging using the correct velocity model, due to the longer time taken by the multiply scattered wavefield to reach the receivers. Figure 5.6 shows the ray path for the waves mentioned above. Note that these are an approximation of the actual trajectories.

Building the velocity model and image

For real data, the velocity model is unknown, so we need to build a velocity model in combination with applying an imaging algorithm. We start with a top-down approach in which elastic RTM is applied. The complexity of the velocity model is increased by building each successive velocity model from the previous migration result. The initial velocity model consists of a thin layer of silicone rubber in the first millimetres and then a fluid layer where the P-wave velocity, the S-wave velocity and density are constant. Note that all the models used in the velocity model building are smoothed. We apply a Laplacian filter to the migrated images to reduce low frequency artifacts. The true model of the tube is overlain in yellow in all images. In addition, we remove the first 2 mm of the migrated images to focus on the large impedance surface and remove artifacts at the source positions. Using this model we are able to resolve the top of the tube. Figure 5.7a, 5.7b and 5.7c show the image I_{PP} , I_{PS} and I_{SS}, respectively. The sides of the tube are not imaged because the energy reflected off the sides of the tube is scattered downward and does not return to the transducer. Part of the backside of the tube is imaged; however its thickness is distorted due to the slow velocity used.

Based on the previous migrated image, we generate a half-space tube velocity model (Figure 5.8 top). We consider the velocity below the top of the tube interface to be made entirely of tube material. Elastic RTM is then applied again, but using the new smooth velocity model. Figure 5.8 bottom shows the new migrated images. The bottom of the uppermost section of the tube is now visible in both the I_{PP} and I_{PS} images (black arrow in Figures 5.8a and 5.8b, bottom); however, in I_{PS}, it is defined with high resolution. Notice that we only obtain S-waves when a conversion of P-wave occurs. We expect that the migrated image using the S-waves from source and receiver has the smaller amplitude, as shown in the image migrated I_{SS}. In addition, note that the wavelength of the S-waves is smaller than that of the P-waves which leads to high resolution in I_{SS}. The bottom of the tube and the lowermost section of

the tube appear in all images; however, their locations are distorted due to the high velocity used (blue arrows in Figures 5.8a, 5.8b, 5.8c). In seismic imaging, half-space velocity models are commonly used to locate the bottom interfaces of salt bodies [85].

Using the previous I_{PP} and I_{PS} images (Figures 5.8a and 5.8b bottom), where the upper sections of the tube are resolved, we create a smooth horseshoe velocity model where we downward continue the side of the tube as is shown in Figure 5.9 top. Elastic RTM is applied again using this model. From Figure 5.9 bottom, we see that we are able to image the bottom of the tube and part of the reflections that come from the interior of the tube (blue arrows in Figures 5.9a and 5.9b). However, both the bottom of the tube and the lowermost section are mis-positioned, and several artifacts are present. Due to the distortion, they appear to be deeper than their actual position. The tube sides are still not resolved in I_{PP}; however, I_{PS} and I_{SS} are able to image a few of the reflections off the sides. The acquisition geometry and large velocity contrast of the tube refract the waves steeply down from the sides of the tube. Therefore, little energy is directed upwards, making imaging the tube sides difficult. In addition I_{PS} shows some artifacts which are related to the polarity reversal of the converted P-and S-wave. This can be improved by applying angle decomposition methods [93, 33].

Knowing the location of the upper sections of the tube and using the known outer and inner diameter of the tube of 20 mm and 8 mm marked on Figure 5.9b, we construct a full velocity model (Figure 5.10 top). Following this, we apply elastic RTM using the velocity model shown in Figure 5.10 top and give the results in Figure 5.10 bottom. We can see an improvement in the definition of the surfaces with large impedance contrast. In the I_{PP} image, we only see a limited section of the interior of the tube; however, in I_{PS} and I_{SS} images, the tube's interior is better defined. When the P-wave mode is back-propagated to the tube, part of it is converted to the S-wave mode and then bounces around inside the tube. Thus, the bouncing waves inside the tube interfere with the incoming P- or S-wave mode, helping in the formation of the I_{PS} and I_{SS} images.

Increasing image resolution

To improve the final images present in Figure 5.10 bottom, we increase the resolution in the first half of the velocity model from 500 to 900 pixels in x direction and from

250 to 450 pixels in the z directions. Figure 5.11 shows the I_{PP}, I_{PS} and I_{SS} images obtained. As we expected, all of the images have higher definition on the interfaces and fewer artifacts due to the numerical dispersion that degrades the resulting image's accuracy.

In general, elastic RTM is capable of recovering large contrast interfaces. We are also able to determine the thickness between the top and uppermost section of the tube equal to 6.0 mm as marked in Figure 5.10a. Combining I_{PP}, I_{PS} and I_{SS} in the interpretation process is advantageous to obtain better locations of the reflectors.

5.5 Discussion

Our results show that elastic RTM is robust enough to image a velocity model with large impedance contrasts. Furthermore, the decomposed wavefield images produced i.e. I_{PS} and I_{SS}, could be applied to estimate shear and compressional speed; methods such as wavefield-migration velocity analysis could be applied [74]. Imaging the interior of the PMMA tube is challenging; however, the P-wave mode back-propagation that is converted into S-waves inside the tube helps in forming I_{PS} and I_{SS} images, defining the interior of the tube with more precision (Figures 10b and 10c). Multiples are also present in our results, causing artifacts. Due to the velocity variations, the artifacts generated by the P-wave and S-wave multiples are not necessarily consistent in-depth, even when the correct velocity is provided. Thus, when multiples are stronger than the PP-, PS- and SS-waves, the measure of focusing or defocusing might give inaccurate results in the inversion (equation 5.2). Therefore, multiple suppression should be performed before the inversion. These multiples can be well attenuated in the data with the combination of sparse hyperbolic radon transform, and predictive deconvolution [64, 20].

The wave mode separation is not completely accurate because of the variation of the velocity model, which violates the homogeneous assumption in the Helmholtz decomposition, causing some artifacts in the migration images associated with the crosstalk between P- and S-wave modes. Other modeling methods that simulate pure P- and S-waves may minimize the crosstalk in the final migration result [33].

To this point, we have tested conventional mode wave imaging conditions to ultimately use their measurement of focusing as an input in the objective function

(equation 5.2) using a local solver. However, to extract more information from the data and better focus the images, we need to investigate common image gather (CIG) and angle domain imaging conditions [93]. Those imaging conditions allow for elastic AVA analysis. The next step will test CIG imaging conditions and then apply them in the objective function (equation 5.2) using the local solver to recover the elastic parameters. We expect the inversion to improve the resolution of the model based on the focusing results. Thus, running a local solver at the top of a bone model with similar geometry would be quite effective and faster in determining the thickness of bones, the P- and S-wave velocities of the bone and its interface locations.

5.6 Conclusions

We investigated different imaging conditions based on P- and S-wave modes using elastic RTM with only P-waves both from the source and receiver sides. We analyze the imaging conditions using first synthetic data in a layered model and then in a PMMA tube laboratory dataset. We used the Helmholtz decomposition method to extract P- and S-wave modes from the elastic wavefields reconstructed in the subsurface. The image formed using SS modes in the longitudinal data showed a much higher definition of the deep layer present in the velocity model than PS and PP images, suggesting that exploiting the information in the shear wave helps in the imaging of deep structures. The reconstruction of the PMMA tube real-data is more challenging than the longitudinal data. However, we were able to reconstruct the upper sections of the PMMA tube successfully. Reconstructing the interior of the tube is more complicated, so that suppression of multiples needs to be included in the analysis. Overall, our results suggest that decomposed wavefield images are a good starting point for exploring multicomponent elastic imaging domain inversion.

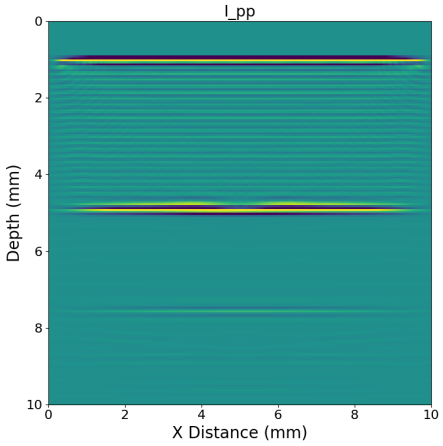

(a): I_{PP}

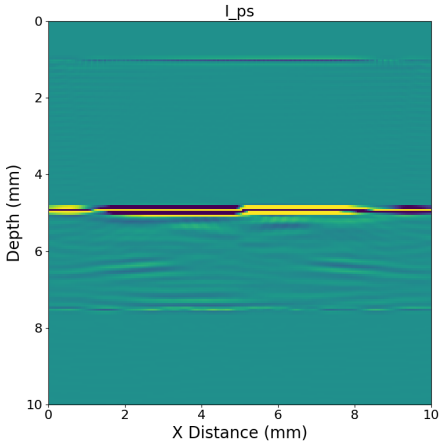

(b): I_{PS}

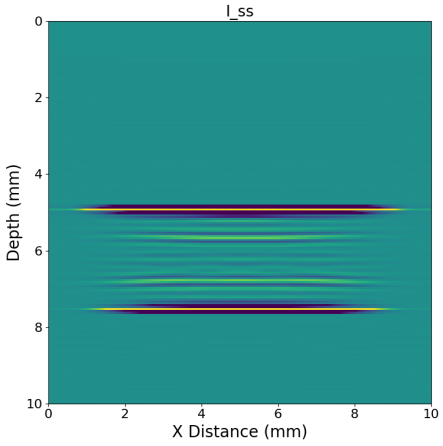

(c): I_{SS}

Figure 5.2: Image migrated using the elastic velocity model shown in Figure 5.1. We use elastic RTM with 96 sources. We see the top and bottom reflectors in all images (a) I_{PP}, (b) I_{PS} and (c) I_{SS} but with different strengths.

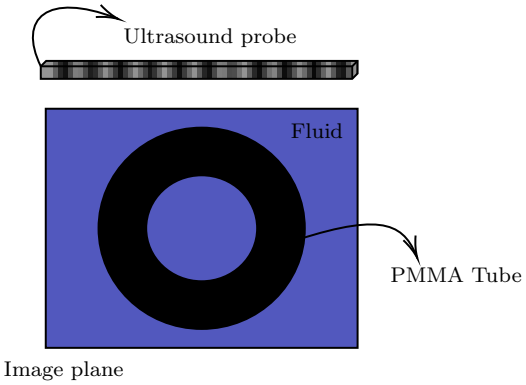

Figure 5.3: Illustration of the acquisition configuration for the PMMA data. The outer and inner diameter of the tube are 20 and 8 mm, respectively. The PMMA tube is immersed in water.

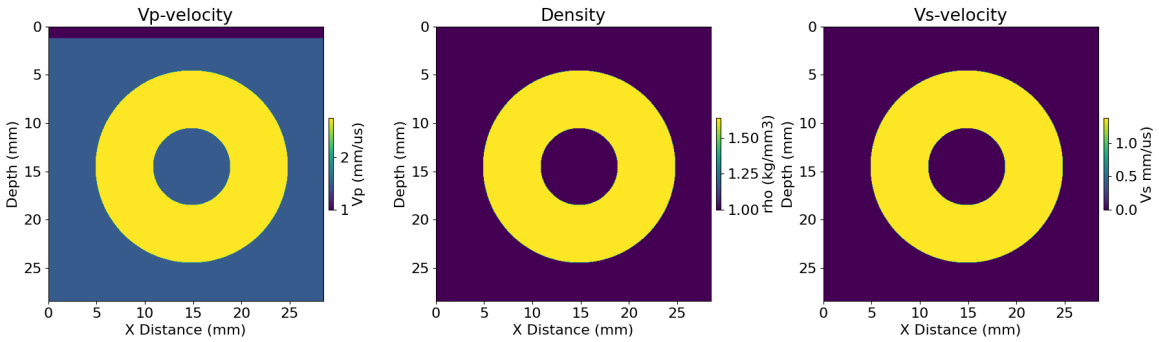

Figure 5.4: Elastic velocity model showing a large contrast interface between the fluid and the PMMA tube (donut) in the center.

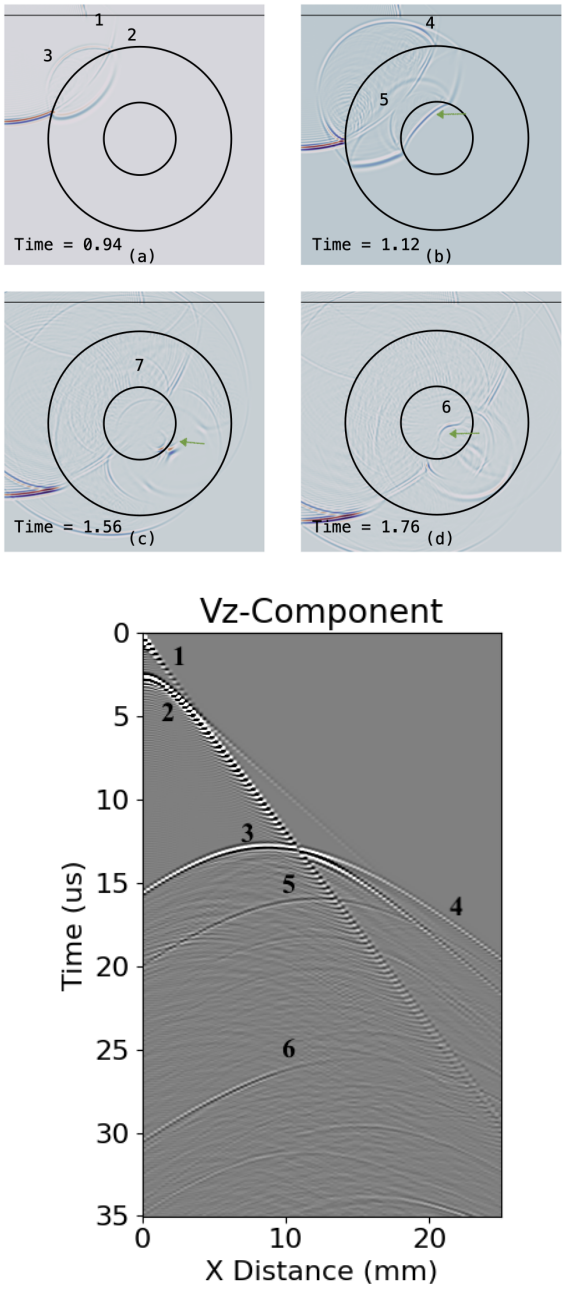

Figure 5.5: Top: different snapshots of v_z-component wavefield propagation in the velocity model shown in Figure 5.4. The numbers mark (1) the direct wave, (2) the silicone refracted wave, (3) the tube external reflection,(4) the tube head wave,(5) the tube upper internal reflection, (6) lower internal reflection and (7) the guided tube wave. The green arrow marks part of the wave propagation inside the tube. Bottom: v_z- component shotgather with the same labelling for reflected waves.

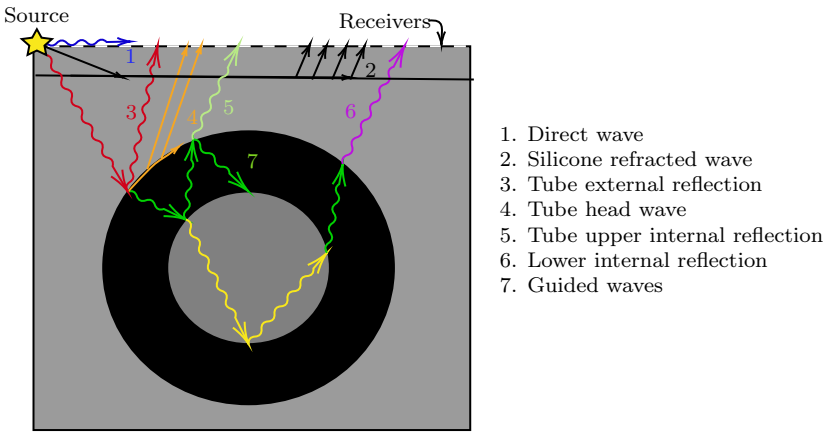

Figure 5.6: Cartoon illustrating the direct wave (1), silicone refracted wave (2), the tube external reflection (3), the tube head wave (4), the tube upper internal reflection (5), lower internal reflection (6) and the guide tube wave (7). The numbers mark off the path in the figure.

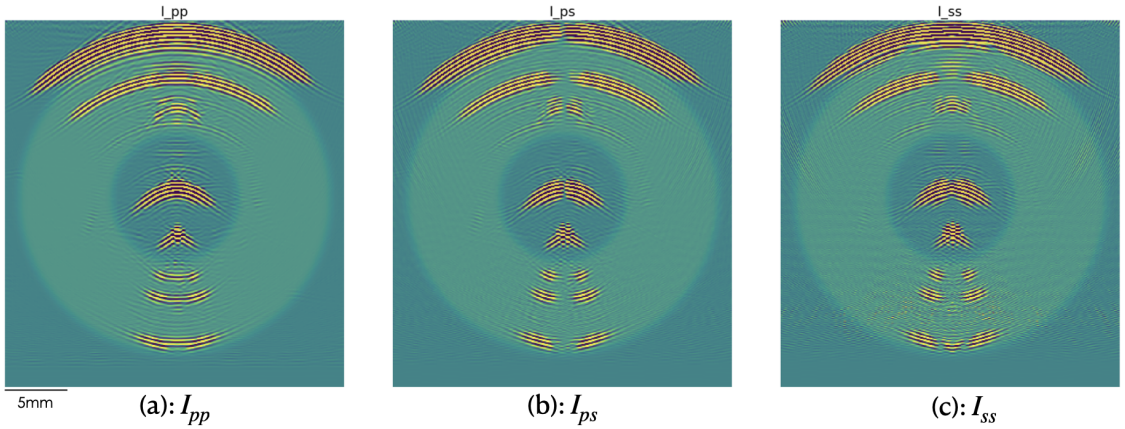

Figure 5.7: Image migrated using a constant velocity model. Elastic RTM was run for 96 shots. The top of the tube is clearly shown in all images (a) I_{PP}, (b) I_{PS} (c) I_{SS}.

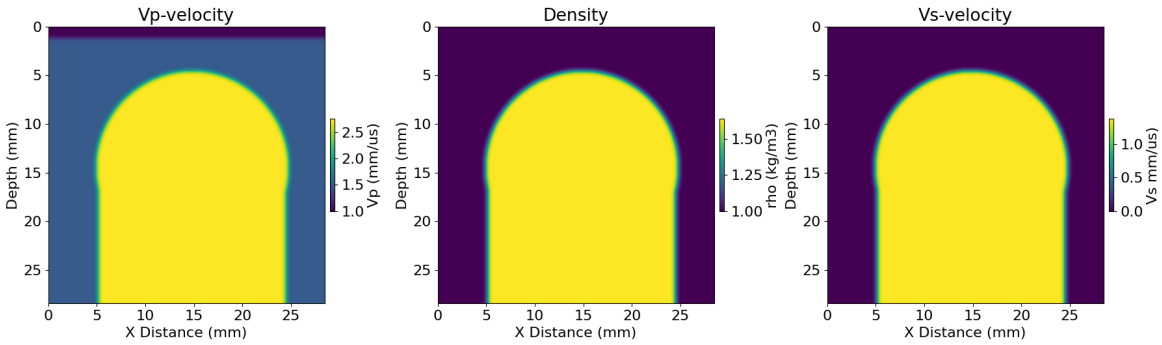

Smoothed half-space elastic velocity model.

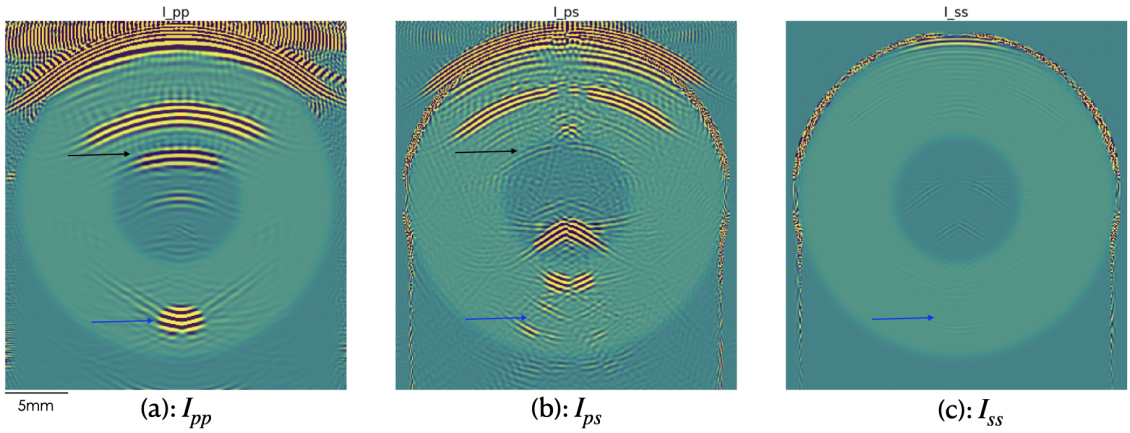

Figure 5.8: Top: smoothed half-space elastic velocity model. Bottom: images obtained using tube half space velocity model (top). The top and uppermost section of the tube is resolved in I_{PP} and I_{PS}. To highlight the potential reflections we saturate the scale in all images. The uppermost internal section of the tube is marked with black arrows in (a) and (b). The blue arrows show the bottom of the tube distorted by the high velocity.

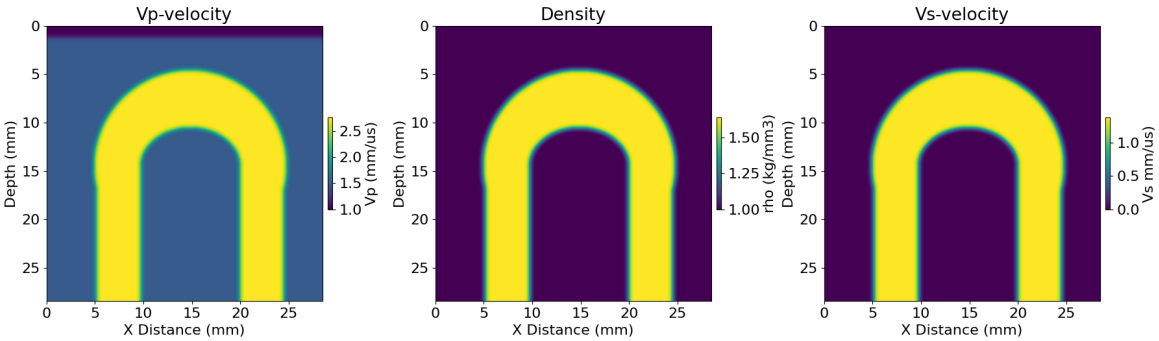

Smoothed horseshoe elastic velocity model.

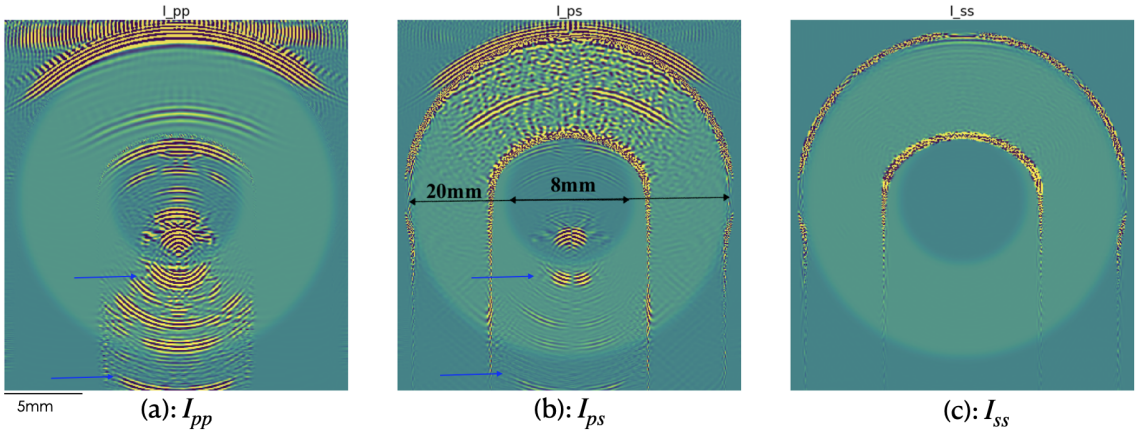

Figure 5.9: Top: smoothed horseshoe elastic velocity model. Bottom: images obtained using the horseshoe velocity model (top). The black arrows point out the bottom and internal lowermost section of the tube. To highlight the potential reflections we saturate the scale in all images.

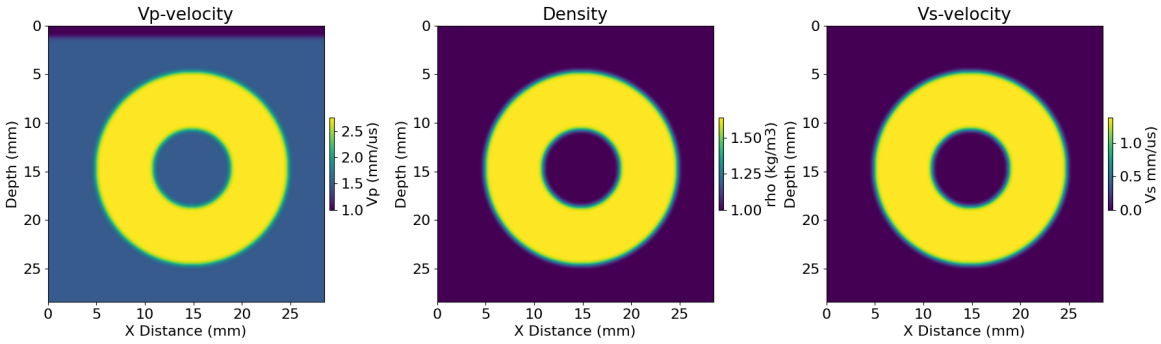

Smoothed full tube elastic velocity model.

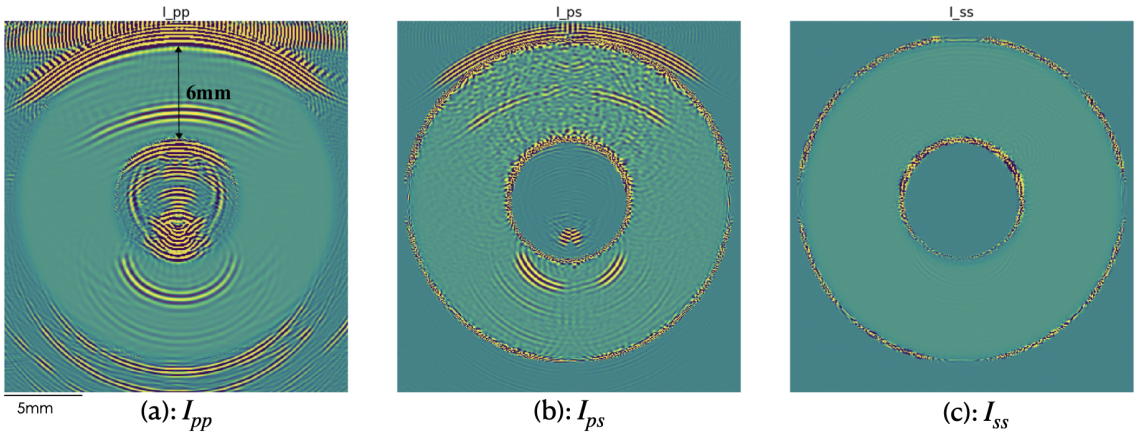

Figure 5.10: Top: smoothed full tube elastic velocity model. Bottom: images obtained using the full tube velocity model (Top). To highlight the potential reflections we saturate the scale in all images.

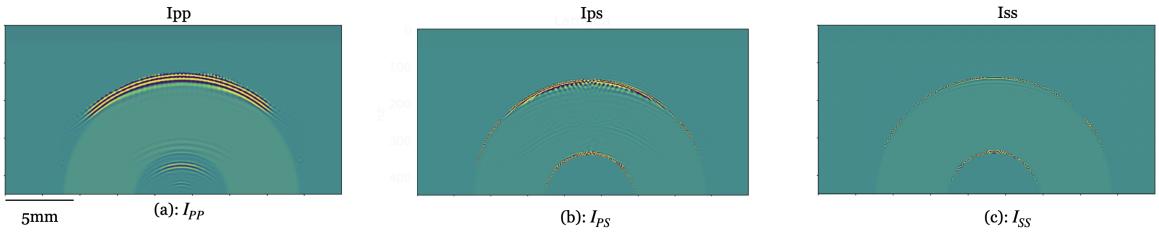

Figure 5.11: Images obtained using the top half tube velocity model with higher resolution.

Chapter 6

Conclusions and Future Work

In this thesis, we have investigated the performance of localized elastic AVO and PVO inversion in case of large contrast reflectors. This thesis represents mainly theoretical studies on synthetic data. The results can be used as a motivation for further development in theoretical and practical aspects.

In **Chapter 2**, we model the amplitude of the reflection using an acoustic-elastic local solver on a simple two-layer model and on a more complex heterogeneous velocity model. We notice that the combination of the size of the local solver and taper as well as the position of the source play an important role in the behaviour of the modeled amplitude curves and the resulting accuracy of the inversion. Then, we incorporate the amplitude as a constraint in the inversion and we show that, for an amplitude and phase inversion, we are able to recover more accurate model parameters of a reflector of interest compared to what we can obtain with the phase alone. We observe that to recover accurate P-wave velocities, V_p and V_s should be inverted simultaneously. In the inversion of density the number of sources included in the inversion is important. The acoustic-elastic local solver is able to recover parameters closer to the global minimum of the objective function improving the accuracy of the recovered model.

Using the MPS method and a staggered FD scheme, we implement a local elastic solver shown in **Chapter 3**. We show that we only need one surface and five wavefield quantities to reconstruct the wavefield accurately within a subdomain. This local solver is memory efficient compared with local solvers that use the FD-injection method. After, we show how to extrapolate scattered wavefield from the local solver to the receiver's location. We validate the local solver against full elastic simulations.

At this point, there are not many published examples of local solver applied to larger contrast reflectors. In addition, it is not well understood how AVO and PVO compared in accuracy and efficiency to FWI. In **Chapter 4** we investigate this question on a subsection of the SEAM model. We observed that AVO and PVO inversion with a local solver could retrieve elastic parameters with less than 0.2% error. We found that the memory required for FWI is substantially larger than for AVO and PVO inversion and the time cost for the local solver indicates a saving of 18% compared with the FWI.

In **Chapter 5** we carry out the local solver to the next level, evaluating how we can apply the focusing and defocusing of migrated images with elastic reverse time migration to retrieve elastic parameters in complex velocity models to ultimately compute velocity updates with the local elastic solver. We investigated different imaging conditions based on P- and S-wave modes using elastic RTM. We analyzed the imaging condition using two models. First, a layered synthetic model is used in the analysis and then we use PMMA tube laboratory data. We found that the image formed using SS modes for the first model shows a better definition of the deep layer present in the velocity model than PS and PP images. Reconstructing the tube laboratory data was more challenging. However, we were able to reconstruct the upper sections of the tube. Our results suggested that decomposed wavefield images are a good starting point for exploring multicomponent elastic imaging domain inversion and that exploiting the information in the shear wave could help in the diagnostics of deep structures.

Overall, this thesis investigates the potential of local solvers in seismic imaging and inversions. Local solvers combined with conventional inversion methods allowed us to have faster solutions, reducing time and computational cost and improves the interactivity of inverse problems. Our framework using AVO/PVO does not allow us to exploit the full information in the seismic wavefield. However, we study the amplitude and phase attributes that enable us to investigate questions that would not be feasible with FWI. Despite the limitation of the local solvers, which ignores the high-order interactions between the inside scattered wavefield and the structures outside injection boundaries, it is possible to recover elastic parameters from materials inside the local areas with high accuracy. We move forward on a better understanding of the local solver under different scenarios and their potential implementations.

6.1 Future directions

There are many ways to improve our understanding of local solver and the methods introduced in this thesis. For example, we can extend all the approaches to include more realistic physics, including anisotropy and viscoelasticity. Anisotropy and viscoelasticity are present during the wavefield propagation, affecting the inversion. Anisotropy is essential to retrieve S-wave velocity and density and provide information about fracture distributions. Other authors have studied anisotropy and viscoelasticity widely so that we expect the implementation of these algorithms to the actual local solver method to be relatively straightforward [3, 95].

In AVO and PVO inversion, the phase carries most of the information in the implementation because it has a more extensive range than the amplitude and thus intrinsically carries greater weight in the inversion setup. We attempt to normalize the amplitude and phase using different approaches. For example, we scale amplitude and phase data to have values between zero and one. However, for this case, the inversion does not converge. In fact sometimes, the inversion diverged quite far from the true value. We also apply the normalization proposed by [46]. However, the method produced a non-stable algorithm. The next step for the local solver is to use strategies that optimize and regularize the inversion algorithm. Improving the robustness of the inversion algorithm will help to improve the optimization approach to a unique solution.

Both local solvers used in this thesis ignore the high-order interactions between the inside scattered wavefield and the structures outside injection boundaries. We can solve this problem by implementing the exact boundary condition [8]. This method requires a real-time update of the injection boundary wavefield in case of model alterations. [81] implemented this approximation is the acoustic domain using MPS, showing improvement in comparison to other local modeling methods. The extension should be easy to implement in the elastic domain based on the approach we showed in this thesis. We can also consider extending all of the methods exposed in this thesis to 3D and even implementing other numerical modelling methods, such as finite-element or spectral-element methods. This idea has been recently started by [91] using spectral elements.

Even though the local elastic solvers were applied to retrieve elastic parameters

and improve the velocity model, additional applications can be found, such as reservoir monitoring or outside the geophysics field, as shown in Chapter 5 for medical imaging. Medical imaging shares the main goal with geophysics since both are looking for information about the shape, dimensions, elastic parameters and sound speed profiles of the local target.

6.2 Perspective

In this thesis, we demonstrate the potential of local solvers for reconstructing wavefields with high accuracy while reducing time and computational cost. The main advantage of this speed-up in modeling wavefields is reflected in more interactive inversions where the cost of the forward modeling is a limitation. This is also a key in continuous monitoring systems and time-lapse inversions. Understanding and improving local solvers open up new pathways to transform current forward modeling methods. Medical imaging, nondestructive testing, and environmental engineering are some fields where the local solvers can also be applied. An example of medical imaging could be monitoring symptomatic bone lesions and the effects of treatments, where only a tiny part of the bone is of interest. Small target domains also decrease the computational cost, giving room to improve the resolution of the image of the target model. Furthermore, the implementations of more complex inversion methods could be achieved, such as the computation of full Hessian, instead of only approximations that allow improvement on inversion results.

Bibliography

[1] O. E. Aaker, E. B. Raknes, Ø. Pedersen, and B. Arntsen. Wavefield reconstruction for velocity–stress elastodynamic full-waveform inversion. *Geophysical Journal International*, 222(1):595–609, 2020.

[2] K. Aki and P. G. Richards. *Quantitative Seismology*. University Science Books. Sausalito, CA, 2002.

[3] T. Alkhalifah and R.-É. Plessix. A recipe for practical full-waveform inversion in anisotropic media: An analytical parameter resolution study. *Geophysics*, 79(3):R91–R101, 2014.

[4] Z. Alterman and F. Karal Jr. Propagation of elastic waves in layered media by finite difference methods. *Bulletin of the Seismological Society of America*, 58(1):367–398, 1968.

[5] E. Baysal, D. D. Kosloff, and J. W. Sherwood. Reverse time migration. *Geophysics*, 48(11):1514–1524, 1983.

[6] D. Borisov and S. C. Singh. Three-dimensional elastic full waveform inversion in a marine environment using multicomponent ocean-bottom cables: A synthetic study. *Geophysical Journal International*, 201(3):1215–1234, 03 2015.

[7] D. Borisov, S. C. Singh, and N. Fuji. An efficient method of 3-D elastic full waveform inversion using a finite-difference injection method for time-lapse imaging. *Geophysical Journal International*, 202(3):1908–1922, 2015.

[8] F. Broggini, M. Vasmel, J. O. Robertsson, and D.-J. van Manen. Immersive boundary conditions: Theory, implementation, and examples. *Geophysics*, 82(3):T97–T110, 2017.

[9] J. P. Castagna, F. Al-Jarrah, and S. Chopra. Rock-physics foundation for avo analysis. In *AVO*, pages 15–33. Society of Exploration Geophysicists, 2014.

[10] C. H. Chapman, J. W. D. Hobro, and J. O. A. Robertsson. Correcting an acoustic wavefield for elastic effects. *Geophysical Journal International*, 197(2):1196–1214, 03 2014.

[11] I. L. Chen Ning, P. Sava, et al. Seismic imaging with optimal source wavefield reconstruction. In *SEG International Exposition and Annual Meeting*. Society of Exploration Geophysicists, 2019.

[12] Y. Choi, D.-J. Min, and C. Shin. Two-dimensional waveform inversion of multi-component data in acoustic-elastic coupled media. *Geophysical prospecting*, 56(6):863–881, 2008.

[13] S. Chopra and J. P. Castagna. *Avo*. Society of Exploration Geophysicists, 2014.

[14] J. F. Claerbout. Toward a unified theory of reflector mapping. *Geophysics*, 36(3):467–481, 1971.

[15] P. Connolly. Elastic impedance. *The Leading Edge*, 18(4):438–452, 1999.

[16] T. Dahlke, B. Biondi, and R. Clapp. Applied 3d salt body reconstruction using shape optimization with level sets. *Geophysics*, 85(5):R437–R446, 2020.

[17] A. T. De Hoop. Representation theorems for the displacement in an elastic solid and their application to elastodynamic diffraction theory. *Ph.D. thesis, Delft University of Technology*, 1958.

[18] J. Dellinger and J. Etgen. Wave-field separation in two-dimensional anisotropic media. *Geophysics*, 55(7):914–919, 1990.

[19] Y. Duan and P. Sava. Scalar imaging condition for elastic reverse time migration. *Geophysics*, 80(4):S127–S136, 2015.

[20] G. Ely, A. Malcolm, and G. Renaud. Suppression of internal multiples with a group sparse radon transform for imaging the interior of bone. In *SEG Technical Program Expanded Abstracts 2018*, pages 4807–4811. Society of Exploration Geophysicists, 2018.

[21] Exxomobil. Using Full Wavefield Inversion (FWI) seismic imaging to map formations below the seafloor.

[22] N. Favretto-Cristini, P. Cristini, and E. De Bazelaire. Influence of the Interface Fresnel zone on the reflected P-wave amplitude modelling. *Geophysical Journal International*, 171(2):841–846, 11 2007.

[23] M. Fehler and P. J. Keliher. *SEAM Phase 1: Challenges of subsalt imaging in tertiary basins, with emphasis on deepwater Gulf of Mexico*. Society of Exploration Geophysicists, 2011.

[24] S. Fomel and M. van der Baan. Local similarity with the envelope as a seismic phase detector. In *SEG Technical Program Expanded Abstracts 2010*, pages 1555–1559. Society of Exploration Geophysicists, 2010.

[25] E. Forgues and G. Lambaré. Parameterization study for acoustic and elastic ray plus born inversion. *Journal of Seismic Exploration*, 6(2-3):253–277, 1997.

[26] J.-L. Gennisson, T. Deffieux, M. Fink, and M. Tanter. Ultrasound elastography: principles and techniques. *Diagnostic and interventional imaging*, 94(5):487–495, 2013.

[27] A. Gholami, H. S. Aghamiry, and M. Abbasi. Constrained nonlinear amplitude variation with offset inversion using Zoeppritz equations. *Geophysics*, 83(3):no. 3, R245–R255, 2018.

[28] A. Gillman, A. H. Barnett, and P.-G. Martinsson. A spectrally accurate direct solution technique for frequency-domain scattering problems with variable media. *BIT Numerical Mathematics*, 55(1):141–170, 2015.

[29] D. Givoli and J. B. Keller. Non-reflecting boundary conditions for elastic waves. *Wave motion*, 12(3):261–279, 1990.

[30] J. F. Greenleaf and R. C. Bahn. Clinical imaging with transmissive ultrasonic computerized tomography. *IEEE Transactions on Biomedical Engineering*, 94(2):177–185, 1981.

[31] J. F. Greenleaf, S. A. Johnson, and A. H. Lent. Measurement of spatial distribution of refractive index in tissues by ultrasonic computer assisted tomography. *Ultrasound in medicine & biology*, 3(4):327–339, 1978.

[32] M. J. Grote and I. Sim. Local nonreflecting boundary condition for time-dependent multiple scattering. *Journal of Computational Physics*, 230(8):3135–3154, 2011.

[33] B. Gu, Z. Li, X. Ma, and G. Liang. Multi-component elastic reverse time migration based on the p-and s-wave separated velocity–stress equations. *Journal of Applied Geophysics*, 112:62–78, 2015.

[34] Q. Guo and C. Rivera. Elastic reflection FWI for subsalt velocity reconstruction: Benchmark test with massive salt body. In *SEG Technical Program Expanded Abstracts 2019*, pages 1600–1604. Society of Exploration Geophysicists, 2019.

[35] R. Hewett and L. Demanet. The pysit team, 2013. *PySIT: Python seismic imaging toolbox v0.5: Release 0.6. URL http://pysit.org/*, 2013.

[36] H. Igel. *Computational seismology: a practical introduction*. Oxford University Press, 2017.

[37] M. Imbault, A. Faccinetto, B.-F. Osmanski, A. Tissier, T. Deffieux, J.-L. Gennisson, V. Vilgrain, and M. Tanter. Robust sound speed estimation for ultrasound-based hepatic steatosis assessment. *Physics in Medicine & Biology*, 62(9):3582, 2017.

[38] L. E. Jaimes-Osorio, A. Malcolm, and A. Gholami. Amplitude variation with offset (AVO) inversion using acoustic-elastic local solver. *Geophysics*, 85(3):1–57, 2020.

[39] L. E. Jaimes-Osorio, A. Malcolm, P. Zheglova, E. F. Koene, and H. R. Rasmus. Reduced memory implementation of a local elastic finite-difference solver. *Geophysics*, 86(3):1–44, 2021.

[40] L. E. Jaimes-Osorio, A. Malcolm, P. Zheglova, E. F. Koene, and H. R. Thomsen. Reduced memory implementation of a local elastic finite-difference solver. *Geophysics*, 86(3):1–44, 2021.

[41] E. Koene and J. Robertsson. A finite-difference algorithm to retrieve finite-difference modeled elastic waves at the free surface. In *SEG Technical Program Expanded Abstracts 2018*, pages 3923–3927. Society of Exploration Geophysicists, 2018.

[42] P. Lailly and J. Bednar. The seismic inverse problem as a sequence of before stack migrations. In *Conference on inverse scattering: theory and application*, pages 206–220. SIAM, Philadelphia, PA, 1983.

[43] Z. Li, S. Ji, B. Bai, Q. Wu, and W. Han. Dirty salt tomography using rtm 3d angle gathers. In *SEG Technical Program Expanded Abstracts 2011*, pages 4020–4024. Society of Exploration Geophysicists, 2011.

[44] C. Lim, N. Ivan, and P. Sava. Seismic imaging with optimal source wavefield reconstruction. In *SEG Technical Program Expanded Abstracts 2019*, pages 4156–4160. Society of Exploration Geophysicists, 2019.

[45] F. Liu, G. Zhang, S. A. Morton, and J. P. Leveille. An effective imaging condition for reverse-time migration using wavefield decomposition. *Geophysics*, 76(1):S29–S39, 2011.

[46] M. Louboutin, L. Guasch, and F. J. Herrmann. Data normalization strategies for full-waveform inversion. In *79th EAGE Conference and Exhibition 2017*, 2017.

[47] M. Louboutin, M. Lange, F. Luporini, N. Kukreja, P. A. Witte, F. J. Herrmann, P. Velesko, and G. J. Gorman. Devito: an embedded domain-specific language for finite differences and geophysical exploration. *https://gmd.copernicus.org/articles/12/1165/2019/*, 2018.

[48] M. Louboutin, P. Witte, M. Lange, N. Kukreja, F. Luporini, G. Gorman, and F. J. Herrmann. Full-waveform inversion, part 1: Forward modeling. *The Leading Edge*, 36(12):1033–1036, 2017.

[49] Y. Masson, P. Cupillard, Y. Capdeville, and B. Romanowicz. On the numerical implementation of time-reversal mirrors for tomographic imaging. *Geophysical Journal International*, 196(3):1580–1599, 2013.

[50] Y. Masson, P. Cupillard, Y. Capdeville, and B. Romanowicz. On the numerical implementation of time-reversal mirrors for tomographic imaging. *Geophysical Journal International*, 196(3):1580–1599, 2014.

[51] R. Mittet. Implementation of the Kirchhoff integral for elastic waves in staggered-grid modeling schemes. *Geophysics*, 59(12):1894–1901, 1994.

[52] P. Mora. Nonlinear two-dimensional elastic inversion of multioffset seismic data. *Geophysics*, 52(9):1211–1228, 1987.

[53] P. M. Morse and H. Feshbach. *Methods of Theoretical Physics*. McGrow-Hill, 1953.

[54] S. Operto, Y. Gholami, V. Prieux, A. Ribodetti, R. Brossier, L. Metivier, and J. Virieux. A guided tour of multiparameter full-waveform inversion with multicomponent data: From theory to practice. *The Leading Edge*, 32(9):1040–1054, 2013.

[55] C. Peng, M. Wang, N. Chazalnoel, and A. Gomes. Subsalt imaging improvement possibilities through a combination of FWI and reflection FWI. *The Leading Edge*, 37(1):52–57, 2018.

[56] R.-É. Plessix. Three-dimensional frequency-domain full-waveform inversion with an iterative solver. *Geophysics*, 74(6):WCC149–WCC157, 2009.

[57] R.-E. Plessix and Q. Cao. A parametrization study for surface seismic full waveform inversion in an acoustic vertical transversely isotropic medium. *Geophysical Journal International*, 185(1):539–556, 2011.

[58] R. G. Pratt. Seismic waveform inversion in the frequency domain, part 1: Theory and verification in a physical scale model. *Geophysics*, 64(3):888–901, 1999.

[59] G. Renaud, P. Clouzet, D. Cassereau, and M. Talmant. Measuring anisotropy of elastic wave velocity with ultrasound imaging and an autofocus method: application to cortical bone. *Physics in Medicine & Biology*, 65(23):235016, 2020.

[60] T. C. Richards. Motion of the ground on arrival of reflected longltudlnal and transverse waves at wlde-angle reflectlon dlstances. *Geophysics*, 26(3):277–297, 1961.

[61] J. O. Robertsson and C. H. Chapman. An efficient method for calculating finite-difference seismograms after model alterations. *Geophysics*, 65(3):907–918, 2000.

[62] P. Sava and B. Biondi. Wave-equation migration velocity analysis. i. theory. *Geophysical Prospecting*, 52(6):593–606, 2004.

[63] P. Sava and S. Fomel. Time-shift imaging condition in seismic migration. *Geophysics*, 71(6):S209–S217, 2006.

[64] P. Sava and A. Guitton. Multiple attenuation in the image space. *Geophysics*, 70(1):V10–V20, 2005.

[65] P. C. Sava, B. Biondi, and J. Etgen. Wave-equation migration velocity analysis by focusing diffractions and reflections. *Geophysics*, 70(3):U19–U27, 2005.

[66] P. C. Sava and S. Fomel. Angle-domain common-image gathers by wavefield continuation methods. *Geophysics*, 68(3):1065–1074, 2003.

[67] P. Shen and W. W. Symes. Automatic velocity analysis via shot profile migration. *Geophysics*, 73(5):VE49–VE59, 2008.

[68] P. Shen, W. W. Symes, and C. C. Stolk. Differential semblance velocity analysis by wave-equation migration. In *SEG Technical Program Expanded Abstracts 2003*, pages 2132–2135. Society of Exploration Geophysicists, 2003.

[69] X. Shen, I. Ahmed, A. Brenders, J. Dellinger, J. Etgen, and S. Michell. Full-waveform inversion: The next leap forward in subsalt imaging. *The Leading Edge*, 37(1):67b1–67b6, 2018.

[70] R. M. Sigrist, J. Liau, A. El Kaffas, M. C. Chammas, and J. K. Willmann. Ultrasound elastography: review of techniques and clinical applications. *Theranostics*, 7(5):1303, 2017.

[71] C. Stork. Reflection tomography in the postmigrated domain. *Geophysics*, 57(5):680–692, 1992.

[72] W. Symes and J. J. Carazzone. Velocity inversion by differential semblance optimization. *Geophysics*, 56(5):654–663, 1991.

[73] S. Tan and L. Huang. Reducing the computer memory requirement for 3-D reverse-time migration with a boundary-wavefield extrapolation method. *Geophysics*, 79(5):S185–S194, 2014.

[74] Y. Tang and B. Biondi. Subsalt velocity estimation by target-oriented wave-equation migration velocity analysis: A 3d field-data example. *Geophysics*, 78(1):U19–U29, 2013.

[75] A. Tarantola. *Inverse problem theory: Methods for data fitting and parameter estimation*. Elsevier, Amsterdam, 1987.

[76] R. Tatham and P. Stoffa. Vp/Vs -a potential hydrocarbon indicator. *Geophysics*, 41:837–49, 1976.

[77] H. R. Thomsen. Exact wavefield separation on an elastic-free surface with sharp corners. In *SEG Technical Program Expanded Abstracts 2018*, pages 5017–5021. Society of Exploration Geophysicists, 2018.

[78] D.-J. Van Manen, J. O. Robertsson, and A. Curtis. Exact wave field simulation for finite-volume scattering problems. *The Journal of the Acoustical Society of America*, 122(4):no. 4, EL115–EL121, 2007.

[79] M. Vasmel and J. O. Robertsson. Exact wavefield reconstruction on finite-difference grids with minimal memory requirements. *Geophysics*, 81(6):T303–T309, 2016.

[80] M. Vasmel, J. O. Robertsson, D.-J. van Manen, and A. Curtis. Immersive experimentation in a wave propagation laboratory. *The Journal of the Acoustical Society of America*, 134(6):EL492–EL498, 2013.

[81] M. L. Vasmel. *Immersive boundary conditions for seismic wave propagation*. PhD thesis, ETH Zurich, 2016.

[82] D. Vigh, B. Starr, J. Kapoor, and H. Li. 3d full waveform inversion on a gulf of mexico waz data set. In *SEG Technical Program Expanded Abstracts 2010*, pages 957–961. Society of Exploration Geophysicists, 2010.

[83] J. Virieux. P-SV wave propagation in heterogeneous media: Velocity-stress finite-difference method. *Geophysics*, 51(4):889–901, 1986.

[84] J. Virieux and S. Operto. An overview of full-waveform inversion in exploration geophysics. *Geophysics*, 74(6):no. 6, WCC1–WCC26, 2009.

[85] B. Wang, Y. Kim, C. Mason, and X. Zeng. Advances in velocity model-building technology for subsalt imaging. *Geophysics*, 73(5):VE173–VE181, 2008.

[86] K. Wapenaar. General representations for wavefield modeling and inversion in geophysics. *Geophysics*, 72(5):SM5–SM17, 2007.

[87] B. Willemsen and A. Malcolm. An efficient coupled acoustic-elastic local solver applied to phase inversion. *Geophysics*, 82(4):no. 4, R219–R234, 2017.

[88] B. Willemsen, A. Malcolm, and W. Lewis. A numerically exact local solver applied to salt boundary inversion in seismic full-waveform inversion. *Geophysical Journal International*, 204(3):1703–1720, 2016.

[89] B. Willemsen, A. Malcolm, and W. Lewis. A numerically exact local solver applied to salt boundary inversion in seismic full-waveform inversion. *Geophysical Journal International*, 204(3):1703–1720, 2016.

[90] L. A. Willemsen. *Problems with a localized nature in exploration seismology.* PhD thesis, Massachusetts Institute of Technology, 2017.

[91] Y. Xie, C. A. Rychert, N. Harmon, Q. Liu, and D. Gajewski. Multi-solver spectral-element and adjoint methods. *Earth and Space Science Open Archive ESSOAr*, 2020.

[92] S. Xu, Y. Zhang, and B. Tang. 3d angle gathers from reverse time migration. *Geophysics*, 76(2):S77–S92, 2011.

[93] J. Yan and P. Sava. Isotropic angle-domain elastic reverse-time migration. *Geophysics*, 73(6):S229–S239, 2008.

[94] J. Yang, Y. Liu, and L. Dong. Simultaneous estimation of velocity and density in acoustic multiparameter full-waveform inversion using an improved scattering-integral approach. *Geophysics*, 81(6):no. 6, R399–R415, 2016.

[95] P. Yang, R. Brossier, L. Métivier, and J. Virieux. A review on the systematic formulation of 3-d multiparameter full waveform inversion in viscoelastic medium. *Geophysical Journal International*, 207(1):129–149, 2016.

[96] P. Yang, R. Brossier, and J. Virieux. Wavefield reconstruction by interpolating significantly decimated boundarieswavefield boundary interpolation. *Geophysics*, 81(5):T197–T209, 2016.

[97] T. Yang, J. Shragge, and P. Sava. Illumination compensation for image-domain wavefield tomography. *Geophysics*, 78(5):U65–U76, 2013.

[98] Z. Zhang, J. Mei, F. Lin, R. Huang, and P. Wang. Correcting for salt misinterpretation with full-waveform inversion. In *SEG Technical Program Expanded Abstracts 2018*, pages 1143–1147. Society of Exploration Geophysicists, 2018.

[99] X. Zhu, G. McMechan, et al. Phase variation with angle inversion using plane and spherical waves. In *2011 SEG Annual Meeting*, pages 2565–2570. Society of Exploration Geophysicists, 2011.

[100] X. Zhu and G. A. McMechan. Elastic inversion of near-and postcritical reflections using phase variation with angle. *Geophysics*, 77(4):R149–R159, 2012.

[101] X. Zhu and G. A. McMechan. Amplitude and phase versus angle for elastic wide-angle reflections in the τ-p domain. *Geophysics*, 80(1):no. 1, N1–N9, 2014.

[102] K. Zoeppritz. On the reflection and propagation of seismic waves at discontinuities. *Erdbebenwellen VII B*, pages 66–84, 1919.

Appendix A

Local solver in Devito Library

This repository contains the manuscript and a collection of Python codes, synthetic data example and data file for a paper about the open-source software package Local-solver. The example data reproduces the results and figures shown in the SEG publication. The Local-solver software is written in Python 3.6.10 and programming languages. To run the program, the Devito, numpy, scipy and matplotlib libraries are required. (Devito: https://www.devitoproject.org/devito/). We recommend using Docker installation as is provided in (https://www.devitoproject.org/devito/download.html) After Docker and Devito are installed this repository should be copied into the docker container, then a bash shell with Devito should be started using: "docker-compose run devito /bin/bash" before the code can be executed.

1-Abstract
2-Content
3-Prerequisites
4.Running the files
5-License
6-Disclamer

==========

1- Abstract

The recovery of elastic properties from seismic data often requires iterative the use of seismic modeling. The finite-difference method is an essential component in seismic modeling and usually the most computationally expensive step in methodologies such as inversion or reverse time migration. We introduce an implementation of an elastic local solver that allows us to propagate the elastic wavefield within a subvolume after local alteration of the model. We implement the elastic local solver as an add-on to an existing solver, so that minimal changes are required to turn any finite-difference solver into a local solver. We demonstrate the capability of the elastic local solver to reconstruct the wavefield and then we extrapolate the wavefield to the receiver positions to compare with observed data.

2-Content

Python codes

General python modules containing the functions to calculate the shotgather, injection, wavefields, Green functions, and convolution:
- full simulation.py
- local simulation.py
- convolution.py
- compute green function.py
- amplitude phase.py
- calc phase.py

Python scripts to run the different models:
- main model constant.py
- main model seam.py
- main model two layers.py

Python scripts to generate the synthetic local and full models from SEAM I 2D Model:
-create model seam full.py
-create model seam local.py

Python script to generate the synthetic local and full constant models:
-create model constant.py

Python script to generate the synthetic local and full two layer models:
-create model two layer.py

Python script to generate the synthetic local and full two layer coordinates:
-define coordinates.py

Python general modules that contains functions to plot: model, injection, shotgather, and traces:
-plot.py
-plot model.py

Data files:

Synthetic SEAM data.
This data can be download: https://seg.org/News-Resources/Research-Data/Open-Data

-SEAM I 2D Model

3- Prerequisites

The Python software Local solver - requires the library “Devito”, and some Python packages.

The easier way to get Devito is following the instruction

https://www.devitoproject.org/devito/download.html

After installed Devito, the software “Local solver” can run in terminal.

The “Local solver” programs were tested Mac platforms using Python 3.6.10.

Ram memory require for all the sequence $\sim$ 30Gbytes. Time $\sim$ 30 minutes.

4- Running the files

After the libraries are installed, download the folder "Local solver", on your machine.
You can download a zip archive of this repository at: software.seg.org(http://software.seg.org).
Following, be sure that all files are in the same directory.

Open the command prompt window (terminal) and run the command:

1. Constant model:
- python create model constant.py
- python define coordinates.py
- python main model constan.py

2. Two layer model:
- python create model two layer.py
- python define coordinates.py
- Two layer model: python main model two layers.py
- Two layer model: python amplitude phase.py

3. SEAM model:
- python create model seam full.py
- python create model seam local.py
- python define coordinates.py
- python main model seam.py
- python model full.png

WARNING: The output files overwrite when you change the model. Make sure you move the outputs before start to run a new model.

5- Output files

---

1. File create model constant.py:
-full.mat
-local.mat

2. File create model two layers.py:
-full.mat
-local.mat
-full pert.mat
-local pert.mat

3. File python create model seam full.py:
-full.mat
-full pert.mat

4.File python create model seam local.py:
-local.mat
-local pert.mat

5.File define coordinates.py:
-coord rec.mat
-coord se.mat
-coord inj.mat
-coord inj local.mat
-coord se local.mat

6.File full simulation.py:
mi= pert or nonp, isrc=source x coord.
-shotgather src %s %.2f.mat'%(mi, isrc)
-waveform se full src %s %.2f.mat'%(mi, isrc)
-point sources src %s %.2f.mat'%(mi, isrc) #Point sources equation (2)
-geometry %s %.2f.mat'%(mi, isrc)

7.File local simulation.py
mi= pert or nonp, isrc=source x coord.

-waveform se local src %s %.2f.mat'%(mi,i[0])
-v1 local %s.mat'%mi

8.File convolution.py
-shotgather extrapolated.mat

9. compute green functions.py
isorc=source x coord.
-Component source greens se%.2f'%isorc

10. main model constant.py:
-figure:model-vp.png
-figure:injection non src 2500.00.png (figure 3 in the paper)
-figure:trace=%.2f.png'%(xp) (figure 4 in the paper) xp =receiver index position

11. main model two layers.py:
-figure: injection nonp src 2500.00.png
-figure: injection pert src 2500.00.png
-figure: model-vp.png (figure 6 in the paper)
-figure: shotgather vx.png (figure 7 in paper)
-figure: shotgather vz.png
-figure: vx short trace=20.00.png (figure 8 in paper)
-figure: vz short trace=20.00.png
-figure: vx trace=20.00.png
-figure: vz trace=20.00.png
-figure: vx out integral.png
-figure: vz out integral.png

12. amplitude and phase.py
-phases.mat
-figure: windowed shotgather true vx.png
-figure: windowed shotgather extr vx.png
-figure: amplitude.png (figure 9 in the paper)
-figure: Phase.png (figure 10 in the paper)

-figure: QC shot timeindex.png

13. main model seam.py
-figure: injection nonp src 2500.00.png
-figure: injection pert src 2500.00.png
-figure: model-vp.png
-figure: shotgather vx.png (figure 12 in the paper)
-figure: shotgather vz.png
-figure: vx short trace=20.00.png (figure 13 in the paper)
-figure: vz short trace=20.00.png
-figure: vx trace=20.00.png
-figure: vz trace=20.00.png

14. plot model.py -figure: model full.png (figure 11 in the paper)

6- License

---

written permission.

THIS SOFTWARE IS PROVIDED BY THE COPYRIGHT HOLDERS AND CONTRIBUTORS "AS IS" AND ANY EXPRESS OR IMPLIED WARRANTIES, INCLUDING, BUT NOT LIMITED TO, THE IMPLIED WARRANTIES OF MERCHANTABILITY AND FITNESS FOR A PARTICULAR PURPOSE ARE DISCLAIMED. IN NO EVENT SHALL THE COPYRIGHT HOLDER OR CONTRIBUTORS BE LIABLE FOR ANY DIRECT, INDIRECT, INCIDENTAL, SPECIAL, EXEMPLARY, OR CONSEQUENTIAL DAMAGES (INCLUDING, BUT NOT LIMITED TO, PROCUREMENT OF SUBSTITUTE GOODS OR SERVICES; LOSS OF USE, DATA, OR PROFITS; OR BUSINESS INTERRUPTION) HOWEVER CAUSED AND ON ANY THEORY OF LIABILITY, WHETHER IN CONTRACT, STRICT LIABILITY, OR TORT (INCLUDING NEGLIGENCE OR OTHERWISE) ARISING IN ANY WAY OUT OF THE USE OF THIS SOFTWARE, EVEN IF ADVISED OF THE POSSIBILITY OF SUCH DAMAGE.

7- Disclaimer

If you obtained this set of codes from the SEG (downloaded from software.seg.org or otherwise), you must also agree to the following disclaimer:

http://software.seg.org/disclaimer2.txt